Diese Arbeit wurde vorgelegt am
Institut für Elektrische Maschinen der
Rheinisch-Westfälischen Technischen Hochschule Aachen

Modeling of the skin effect in a scalable numerical machine model of an induction machine using analytical calculation methods

Master Thesis

David Maldonado Lopez
Matrikelnummer 398980

Betreuer: Martin Nell, M.Sc. RWTH
Prüfer: Univ.-Prof. Dr.-Ing. habil. Dr. h. c. Kay Hameyer

Aachen, im September 2019

Contents

List of abbreviations vii

1 Introduction 1

2 Fundamentals 3
2.1 Modeling approaches of the induction machine . . . 3
2.1.1 Hybrid simulation approach . . . 5
2.1.2 Iron loss calculation . . . 6
2.1.3 Transient torque-speed map . . . 6
2.2 Scaling of the machine . . . 7
2.3 Skin effect . . . 12
2.3.1 Skin depth . . . 12
2.3.2 Influence of the frequency . . . 13
2.3.3 Influence of the conductor material . . . 13
2.3.4 Influence of shape and size . . . 14
2.3.5 Resistance and inductance variation . . . 14
2.3.6 Skin effect in the IM windings . . . 17
2.4 Rotor bar topologies . . . 18
2.4.1 Rotor bar selection . . . 19
2.4.2 High speed application . . . 22
2.4.3 High starting current . . . 23
2.4.4 Material selection . . . 24

3 Methodical procedure 27
3.1 Modeling process . . . 27
3.2 Simulation and post-processing . . . 29

4 Skin Effect 33
4.1 Simulation of the skin effect . . . 33
4.2 Losses calculation . . . 37
4.2.1 Calculation of DC losses . . . 38
4.2.2 Calculation of AC losses . . . 38
4.2.3 Comparison of the losses calculation methodologies . . . 40
4.2.4 Shape influence in the skin effect . . . 43
4.2.5 Geometry characterization . . . 44

4.3 Skin effect and machine scaling 47
4.3.1 Analysis of the skin depth 52

5 Scaling of the geometry **59**
5.1 Principles of the geometry scaling 59
5.2 Modification of the geometry 62
5.3 Change of the design 71

6 Summary and future work **81**

List of symbols **83**
Latin characters 83
Greek characters 84
Subscripts index 84
Nomenclature 85

Bibliography **87**

Sperrvermerk und Selbstständigkeitserklärung **91**

List of abbreviations

FE	Finite Element
FEA	Finite Element Analysis
FEM	Finite Element Method
HEV	hybrid electric vehicle
IEM	Institut für Elektrische Maschinen
IM	induction machine
MA	maximum ampere
MTPCL	maximum torque per current line
NEMA	National Electrical Manufacturers Association
PMSM	permanent magnet synchronous machine
RWTH	Rheinisch-Westfälische Technische Hochschule

1 Introduction

The improvement of the efficiency to increase power savings is one of the main trends nowadays in the field of electric machines. Among the different drives, the most widely used is the induction machine (IM), which accounts for a big part of the total energy consumption. Therefore, new legislation has been developed that rises the efficiency standards for these machines. As a result, the optimization of the IM must be done from the beginning of the design stage. However, achieving an efficient machine model by means of Finite Element Analysis (FEA) is very time consuming and its implementation is not feasible. The solution to optimize the induction motor is the use of mathematical optimization tools. More specifically, the use of analytical equations that allow computing the new machine magnitudes when the design is altered, which is known as the scaling procedure. The scaling of a machine enables the optimization of the motor design in specific operating points by introducing small changes in the geometric dimensions or material composition. The procedure is based on the Finite Element Method (FEM) results of a reference machine, which are then modified with the scaling equations to yield the results of the new machine.

In the rotor bars of the IM takes place the skin effect, a phenomenon that induces an uneven current distribution. The consequence is a change in the resistance and the inductance of the rotor, which could affect the accuracy of the scaling procedure. Thus, the influence of the skin effect in the results of the analytical equations must be analyzed. This analysis is carried out in a machine whose geometry is scaled radially and in a model in which the rotor bar design is slightly modified.

To analyze this problem, first a literature review of the IM workin principles, scaling process, skin effect and rotor bar topologies is done in chapter 2. In chapter 3, the procedure of the modeling of the machine, the simulation with Finite Element (FE) and the use of the analytical equations is described. The skin effect and its causes are studied in chapter 4. Furthermore, the influence of the phenomenon in the losses calculation and in the machine scaling are also analyzed in this section. In chapter 5, the changes in the geometry of the rotor bar and its consequences in the scaling procedure are studied, first for the introduction of a cooling channel in the rod and subsequently for the change of the topology. Finally, the conclusions of the work and further improvements of the method are presented in 6.

2 Fundamentals

Due to the great importance of the IM and its wide application range, the modeling and design of this electric device is not a minor problem. The main characteristics that make this machine more popular than other are for example its robustness, price, reliability and the automation of its manufacturing process. All these factors make this motor take place in applications that go from small electric fans to big motors that are used in heavy industries, going through the vast range of automotive applications. Therefore, the design of this machine requires a certain amount of effort to achieve a proper optimization that allows the efficiency to be as close to the optimum as possible. In this chapter, the methods that have been used to design the induction motor are going to be analyzed to determine advantages, limitations and feasibility to be applied in the modeling of machines for the automotive industry.

2.1 Modeling approaches of the induction machine

As the IM is a complex device in which several physical phenomena take place, it is convenient to use a model that reduces the complexity but allows performing calculations keeping the errors below a certain threshold. One of the first approaches that was used to model the IM is the T-equivalent-circuit, which is characterized in figure 2.1. With this representation, the electrical machine is reduced to a mathematical model, which represents the electrical components of the motor. The different physical effects that take place in the machine are characterized as inductances and resistances, which allow obtaining the different magnitudes such as power, losses, efficiency, currents, etc. with ease. However, this representation does not have a lot of accuracy as this model is meant for the steady state. Even in steady state, there are considerable inaccuracies as this model does not consider harmonic effects, parameter variations, transient processes, etc. There are cases where the precision is not that critical and the T-equivalent-circuit is accurate enough. These parameters can be measured or calculated with analytical equations. Nevertheless, the latter imply simplifications that reduce accuracy. The calculation of the parameters from measurements is neither a trivial task and requires a certain intrusion in the machine to take measurements, as shown in [23]. Furthermore, if the machine is not built, the measurements are not available and the only design that can be made is a rough one. For all these reasons, other techniques have been developed to design and analyze the IM.

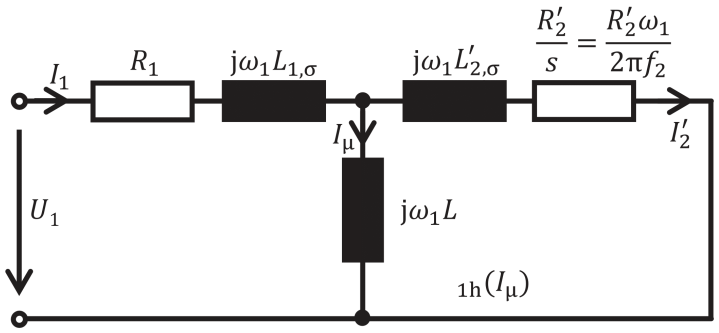

Figure 2.1: T-equivalent-circuit of the squirrel cage IM [36].

Another approach that was developed to design and represent the IM and determine its performance characteristics is the use of analytical calculations, as shown in [4]. These equations model the different phenomena that take place in the device, whether if they are electrical, magnetic or mechanical ones. However, to simulate the entire machine, the amount of equations that are required is much bigger than in the case of the equivalent circuit, as the complexity and the quantity of information needed increases along with the accuracy. Moreover, many simplifications and assumptions are used to obtain the equations, decreasing the reliability of the model. As a result, when the accuracy required for the model is high, this model is not an option. Nevertheless, the use of analytical equations is really useful for some purposes, as it is mentioned in [14]. In this paper, the analytical equations of the IM are used to control the device on-line once the equivalent model of the drive is known. Thus, if the model of the machine is accurate enough, use can be made of analytical equations to perform rapid control or even more complex jobs. However, this does not avoid the problem of requiring a method that allows to represent the machine behavior in an accurate model with more ease.

As the computational power of computers was increasing, a method that uses a huge amount of calculations was developed: the FEM. This method is based in the solving of a big number of partial differential equations to determine the numerical solution of quasi-static electromagnetic boundary value problems, as it is explained in [32]. This method is based on analytical equations that model all the physics of the machine, i.e. the thermal, the electromagnetic and the mechanical models. With the use of FEM, the level of knowledge of the machine and the accuracy of the model are highly increased. As it is stated in [24], the advantages that present the FEM are allowing to represent all the physical effects in a numerical simulation, unlike analytical models that only consider a few. As a result, it takes into account non-linear behavior, local saturation and complex geometries, features that analytical equations lack.

The use of FEM is not a trivial task and requires different simulations to achieve a good model of the machine, as explained in [24]. Having the results from all these simulations is very useful, but the amount of information is excessive to be handled.

Thus, it is desired to reduce all the results from the FEA to a machine model with a lower level of complexity. This process is done with the lumped parameters technique, explained in [16]. These parameters are resistances and inductances obtained from the FEA. The advantage of this approach is that reduces the complex FE simulation into a simplified equivalent model for a certain time step. Furthermore, it also decreases the computational effort when not only the IM is simulated, but also attached devices such as the power electronics. The main inconvenient in the use of the FEM is that the simulation takes a long time because of the transient build-up of the rotor flux, which is the magnitude that requires more time to calculate. If one simulation is done, the computational time is not a big drawback. Nevertheless, when a motor is designed or tested, it is required to obtain the whole torque-speed map that represents the motor operation. For each torque produced by the machine at a certain speed, a point of the map is represented. Obviously not all the points are simulated, only a discretization of them. Still, this can easily involve more than a hundred simulations. Hence, it is convenient to use some techniques that help to speed up the simulations.

2.1.1 Hybrid simulation approach

One approach to reduce the computational times of the FEA is doing a 2-D simulation instead of simulating the entire machine. This method consists in calculating the different magnitudes in one cross-section of the machine, assuming that the rest of the motor behaves in the same way or, at least, in a similar one. As IMs can be considered axially extruded, this approach yields quite accurate results. Moreover, if the precision of this method is not good enough, the accuracy can be improved by using the multi-slice method that is presented in [31]. This technique performs several 2-D simulations of different cross sections of the machine (slices) which are then coupled, achieving results similar to the 3-D simulation.

Another approach to reduce the computational effort, and therefore the time of the simulation, is the hybrid simulation method described in [34] and [33]. As the build-up of the rotor flux is the most time consuming calculation in the FEA, this is accelerated by calculating the steady state flux linkage from the lumped parameters of the machine. These parameters are obtained from a no-load simulation. With the inductances from the lumped parameters, the steady state rotor currents are calculated and used in the transient FE simulation of the machine. The problem of this approach named Linear Hybrid FEA is that the inductances should not have a fix value because it depends on the level of saturation of the magnetic circuit. To consider different levels of saturation and therefore the changes in the inductances, there is another possibility, which is known as Non-Linear Hybrid FEA. Instead of doing one no-load simulation of the machine, several are done with different levels of stator current. By doing so, the saturation level of the machine can be interpolated and the transient FEA calculated with the correct inductances value. The improvements achieved by using the Non-Linear Hybrid FEA can be up to 98% according to [34].

2.1.2 Iron loss calculation

Another problem that leads to high computational effort and simulation time is the calculation of the losses, more precisely the iron losses. These losses are dependent on the harmonics of the magnetic flux density. These harmonics can reach frequencies of several kHz due to e.g. slotting. To consider these, the sampling frequency has to be multiple kHz. To simulate also the fundamental frequency of the rotor current, which is around 1-10 Hz, the simulation time has to be high. Therefore, a high simulation time combined with high sampling frequencies results in high computational effort. To avoid this problem, a change to the time domain is proposed in [36]. The proposed solution is to divide the iron losses into three terms, where each of them is calculated analytically using the derivatives of the flux density and some factors obtained from the material and the machine design. These three terms are: the instantaneous hysteresis losses $p_{\mathrm{hy}}(t)$, the Foucault (macroscopic) eddy-current losses $p_{\mathrm{cl}}(t)$ and the excess (microscopic) eddy current losses $p_{\mathrm{ex}}(t)$. Therefore, the total iron losses can be calculated as

$$p_{\mathrm{Fe}}(t) = p_{\mathrm{hy}}(t) + p_{\mathrm{cl}}(t) + p_{\mathrm{ex}}(t). \tag{2.1}$$

2.1.3 Transient torque-speed map

As mentioned before, when an IM is designed or analyzed, it is usually required to obtain the torque-speed transient map ($T - n$ map). This map represents all the combinations of torque and speed in the machine operation. However, when analyzing the $T - n$, it is convenient to know that on the one hand, in the IM the torque generation depends directly on the current allocation. This magnitude is related to the value of the stator, magnetizing and rotor current. On the other hand, the machine's speed is dependent on the stator and rotor frequencies. Considering that all the terms in the T-equivalent-circuit depend on the stator frequency f_1 except from the stator resistance, if the voltage loss in this element is subtracted, the current allocation can be considered independent from f_1. Hence, the torque-speed map can be transformed into the $\hat{J}_1 - f_2$ map as it is determined in many references such as in [36], in [33] and in [35]. By using this approach, the FEA of the entire map can be done only by changing the input parameters of the machine, avoiding an iterative process in which some input parameters are given and changed until the desired torque and speed are achieved. Once the simulation is done in the $\hat{J}_1 - f_2$ map, the change to the $T - n$ can be easily as explained in [36]. This transformation is achieved by finding the combination of $\hat{J}_1$ and f_2 that provides the desired torque and speed with highest efficiency. Once the point is found, it must be studied if the combination exceeds the voltage limit of the inverter. If it is the case, a point with less stator flux linkage is chosen.

The fact of transforming the $T - n$ map to the $\hat{J}_1 - f_2$ map reduces the complexity of the program but does not reduce significantly the simulation time, being necessary to perform the FEA for a numerous amount of operating points. However, considering all the improvements to the FEM that have been mentioned before, the simulation of the whole operating range of the motor could be affordable. Once the simulation of the machine is done, the next step in many cases is the optimization of it. For example, in the automotive industry, the trend nowadays is to reduce the energy consumption of the motor by increasing the efficiency of it. Thus, for a given operating point, the torque production must be achieved with the minimum input of energy. The optimization can be done by modifying several parameters of the machine. As a result, every time that a parameter is modified, a new simulation of the machine is required. Although the optimization of the FEM reduces computation times, optimizing a machine by performing numerous simulations of the complete operating map is not feasible. Therefore, a different approach is required to optimize an IM.

2.2 Scaling of the machine

As mentioned in the previous section, in the optimization of the IM, the amount of parameters of the motor that can be varied in order to improve the efficiency are numerous. Thus, the simulation of the entire operating map for all the combinations is not feasible. A clear example of this situation is given in [28]. In this paper, the optimal design of a hybrid electric vehicle (HEV) is formulated as a multi-objective optimization problem. The different objectives of the problem could be: reduction of emissions such as CO_2, NO_x or HC, the reduction of costs, the optimization of the electric engine, etc. In the case of the HEV, the process of design is complex and involves selecting the topology of the transmission (series HEV, parallel HEV or series-parallel HEV), optimizing this topology and the size and materials of all the components. For the case of the IM, it should be optimized for each topology several times. If in each case the whole $T - n$ map is to be optimized, the amount of simulations is not affordable. The whole optimization scheme can be observed in figure 2.2.

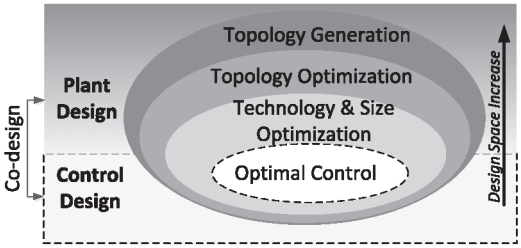

Figure 2.2: Optimization of the HEV [28].

The approach proposed by several authors is the scaling of the machine. This consists in performing a FEA of the motor and obtaining its equivalent model based on the lumped parameters, as was described in section 2.1. Based on this model and making use of analytical equations, it is possible to model the changes in the machine. For instance, once the motor is modeled and a change in the operation varies the temperature of the windings, it would be very useful being able to change the values of the resistances just based on equations. Thus, this procedure would avoid performing a new FEA and would reduce the computational effort. Another example of this approach, although it does not affect the T-equivalent-circuit, is the scaling of the iron losses shown in [35] and [36]. These papers have determined that the different loss components are scaled with the mechanical speed. As a results, the iron losses are evaluated in stator and rotor at one simulation frequency and can be scaled to a different one, e.g. from $f_1 = 80Hz$ to $f_1 = 240Hz$. This scaling of the losses does not solve the problem of optimizing the machine, but provides a good example of how the scaling based on analytical equations works.

A more general approach is provided in [5], where some basic scaling laws were determined for the output of the IM. The parameters of the engine modified in this case were the diameter and length, which are the same as radial and axial scaling. This approach was proposed in 1978, when the FEM could not be used for this purpose. At that time, it was useful for induction motors manufacturers being able to predict the output of the machine based on some geometrical parameters and physical magnitudes, as shown in

$$\text{Output} \propto D^2 L B_\delta \, q \, n \, . \tag{2.2}$$

In this equation, D is the diameter of the machine, L the length of it, B_δ the flux density in the air gap, q the specific electric loading and n the speed of the machine. The problem of using this formula to scale the machine is that the flux density in the air gap and the electric loading are assumed constant, which is not true when the machine is modified. Hence, this analytical approach presents some inaccuracies that should be improved in order to scale properly the device.

A more precise approach is given in [29], where the scaling laws are obtained for a permanent magnet synchronous machine (PMSM). Although the scaling laws of the IM and the PMSM are not the same, they share the same principle. In [29], a machine that is considered the reference is analyzed. Three parameters of this device are modified: the axial and radial dimensions and the rewinding factor. When these parameters are changed in the reference machine by using analytical equations, the scaled machines, are obtained. The use of equations to calculate the machine conditions without a new simulation must fulfill that

$$\vec{H}'(\rho', \phi) = \vec{H}(\rho, \phi) \, . \tag{2.3}$$

In this equation, $\vec{H}$ is the magnetic field strength distribution, which is represented by the module ρ and the angle ϕ. The condition in (2.3) is that the magnetic field distribution is the same in the reference and the scaled machine (represented with the apostrophe). To achieve this condition the input parameters of the scaled machine have to be modified in order to have the same field distribution of the reference. The scaling of the input is done according to

$$I = \frac{k_\tau}{k_\mathrm{W}} \, I_0 \, , \tag{2.4}$$

where I and I_0 are the input currents of the scaled and reference model respectively, k_τ the radial scaling factor and k_W the rewinding factor.

Based on the condition of (2.3) determined in [29], the scaling laws were developed in [22] for the IM. This scaling procedure not only considers changes in the geometry but also in the rotor bar resistance. The geometrical changes are the radial and axial dimension and the resistance ones (apart from those derived from the geometry change) are the material and temperature of the rotor. In order to obtain the same field distribution in the scaled machine as in the reference one, the input parameters should be modified. While in the PMSM the input parameter is the stator current, the IM is characterized by this magnitude and also the rotor frequency. Hence, it is necessary to scale both parameters to obtain the same field distribution.

To use analytical equations to scale the machine, the parameters of the model need to be modified. As mentioned, a change in the rotor resistance due to temperature, geometry or material variations affects the current allocation. To compensate this, the inductances have to be scaled with a time scaling factor $\mathrm{k_t}$. The change of the parameters of the model can be observed in figure 2.3.

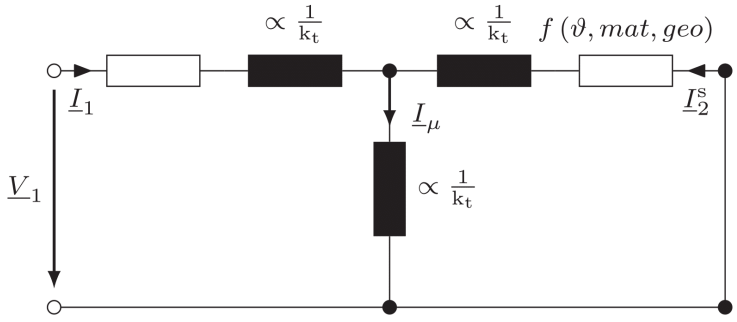

Figure 2.3: Scaled T-equivalent-circuit of the machine [22].

The factors presented in this figure are used to scale the different magnitudes of the machine. The first parameter is k_R, which is calculated with

$$k_R = k_{R1}\, k_{R2}\, \frac{k_a}{k_r^2}\,, \tag{2.5}$$

and considers the variations of the rotor resistance. In (2.5), k_r and k_a are the radial and axial scaling factors of the machine respectively and k_{R1} and k_{R2} are factors that account for the changes in the resistance of the rotor. On the one hand, the variation of k_{R1} is proportional to the ratio of radial to axial change. On the other hand, the value of k_{R2} depends on the conductivity change due to a variation of the temperature or the use of a different material. The second parameter used in the analytical equations is the total time scaling factor

$$k_t = \frac{k_a}{k_R}\,. \tag{2.6}$$

By using the scaling factors described and the magnitudes of the reference model, the parameters of the scaled machine can be calculated according to table 2.1. As it is shown in [22], the errors of using this scaling approach are negligible. Therefore, the optimization of the machine can be performed just by means of analytical calculations. However, there are some physical effects in the machine that depend on some of the parameters that are modified. Thus, the scaling laws have to be modified to account for effects such as the skin effect.

parameter	**variable**	$\propto$
length	l	$\mathrm{k_a}$
lateral surface	A_{surface}	$\mathrm{k_a k_r}$
cross sectional area	A_{cross}	$\mathrm{k_r}^2$
volume	V	$\mathrm{k_a k_r}^2$
magnetic field strength	H	1
magnetic flux density	B	1
magnetic flux linkage	Ψ	$\mathrm{k_a k_r}$
current density	J	$\frac{1}{\mathrm{k_r}}$
current	I	$\mathrm{k_r}$
time	t	$\mathrm{k_t}$
frequency	f	$\frac{1}{\mathrm{k_t}}$
speed	n	$\frac{1}{\mathrm{k_t}}$
torque	T	$\mathrm{k_a k_r}^2$
voltage	U	$\frac{\mathrm{k_a k_r}}{\mathrm{k_t}}$
inductance	L	$\mathrm{k_a}$
reactance	X	$\frac{\mathrm{k_a}}{\mathrm{k_t}}$
rotor resistance	R_2	$\mathrm{k_R}$
mechanical power	P_{mech}	$\frac{\mathrm{k_a k_r}^2}{\mathrm{k_t}}$
mechanical power density	p_{mech}	$\frac{1}{\mathrm{k_t}} = \frac{\mathrm{k_R}}{\mathrm{k_a}}$

Table 2.1: Scaling factors of the different parameters according to [22].

2.3 Skin effect

The skin effect occurs in a conductor that is fed with an alternate current. The consequence of this effect is that the current is distributed in the periphery on the conductor, creating an uneven current distribution that could lead to hot spots, as the losses in the conductor are not homogeneous. The cause of this phenomenon is a bigger variation of the magnetic field in the center of the conductor. This increases the reactance of this area, thus reducing the current circulating in the center of the conductor. In figure 2.4, the heterogeneous current density distribution can be observed.

The main consequence of the uneven current density distribution is that causes a distinct value of the ohmic losses in different areas of the conductor. Since more current flows in a smaller area (i.e. higher resistance), the losses are bigger in these spots. As a result, the ohmic losses are expected to be higher in a conductor affected by the skin effect than in one supplied with $f = 0$, even if the average current is the same. Since the influence of the skin effect is that considerable, the study of the parameters that cause it is conducted.

2.3.1 Skin depth

The term skin depth δ is the basic parameter to characterize how big the influence of this phenomenon is. This factor is defined as the distance over which the current is reduced to $1/e$ of the original value, being e = 2.71. As this original value of the

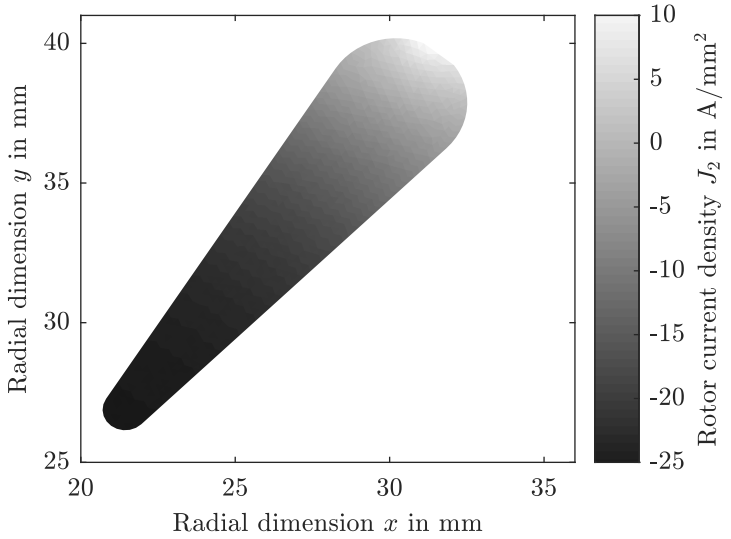

Figure 2.4: Current density distribution in a rotor bar at $J_1 = 14.5\text{A/mm}^2$ and $f_2 = 27$ Hz.

current is difficult to measure when the distribution in the conductor supplied with zero frequency is not available; the skin depth can also be calculated as the distance where the current density in the surface is reduced by $1/e$. Therefore a big value of the skin depth will indicate that the current distribution in the bar is quite even and as a result, the skin effect does not have a big influence. Instead, the lower the skin depth in a conductor, the bigger influence of this phenomenon.

In [27] the parameters that determine the influence of the skin effect are studied. The most important are:

1. the frequency,
2. the material,
3. the shape and
4. the size of the conductor.

To determine the effect of each parameter, it can be done by using the analytical formula proposed in [27] to determine the skin depth in a rectangular conductor, which is calculated with

$$\delta = \sqrt{\frac{1}{\pi f \sigma \mu}}\,. \tag{2.7}$$

2.3.2 Influence of the frequency

The effect of the supply frequency is clear because it is the reason why this phenomenon occurs. Therefore, it is easy to determine that the higher the frequency, the higher the skin effect, and in the case of $f = 0$, the effect barely appears. As shown in (2.7), a higher frequency means a lower skin depth and hence a bigger difference between the current density in the surface and the core of the conductor.

2.3.3 Influence of the conductor material

The other two parameters that have an effect in the skin depth are the material conductivity and the permeability. As the materials used for the conductors are usually aluminum and copper, which are not ferromagnetic materials, these can be considered dielectric and therefore $\mu \approx \mu_0$. Regarding the conductivity, better conducting materials have a bigger influence of the skin effect. The reason is that

the higher the conductivity, the lower the resistance of the conductor (if all other parameters are kept constant). Therefore, the influence of the change of the resistance due to the skin effect is more sensitive. For example, in the case of having two conductors with different conductivities supplied by the same frequency, the value of the resistances tend to the same value as the better conductor has a higher skin effect influence while the other has a greater DC resistance.

2.3.4 Influence of shape and size

As stated in [27], the size of the conductor and its shape also have an influence in the skin effect. In the case of the size, it is clear that if the frequency and conductivity are fixed, the skin depth will not vary in the conductor. For the same skin depth, if the conductor is bigger, the current distribution will be more homogeneous. Finally, the effect of the shape has to do with the distances between the surface and the core, but to determine its effects it should be done with simulations or measurements.

2.3.5 Resistance and inductance variation

The resistance of the conductor is not the only magnitude altered due to the skin effect. As mentioned, the change in the resistance is consequence of the change of the magnetic field in the conductor. For example, in the case of a rectangular conductor, the lower part will have more flux linkages, showing a higher inductance and displacing the current to the top part. This effect is shown in figure 2.5. For the case of the round conductor, the inner zone is the one with higher flux linkages. The result of this phenomenon is that the inductance in the conductor is lower as the frequency increases. For instance, at very high frequencies, the flux linkage is reduced to a small zone, forcing the rest to have a lower inductance. In [13], the variation of the resistance and inductance are studied for a rectangular bar. The result of this variation is the one shown in figure 2.6.

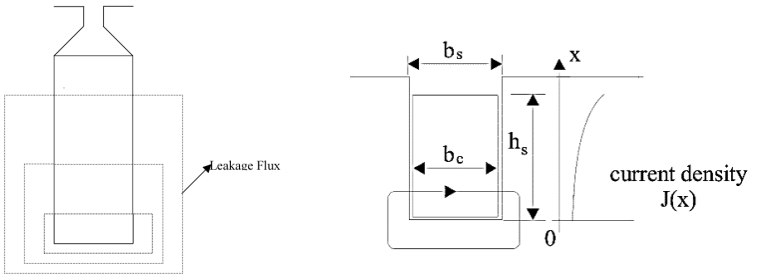

(a) Flux linkages distribution from [25].

(b) Current density distribution from [4].

Figure 2.5: Basic designs of the rotor bars.

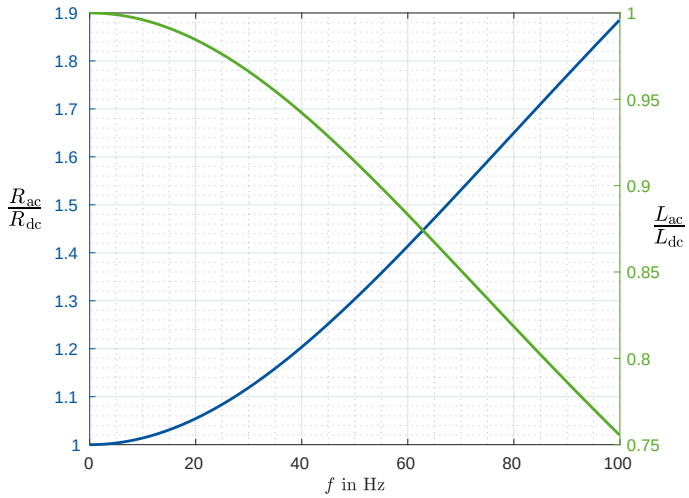

Figure 2.6: Variation of resistance and inductance with frequency.

Although the big influence of the skin effect is proved, it is not a phenomenon easy to predict as it depends on many variables, some of them as difficult to quantify as the shape. Therefore, a lot of literature has been developed in order to predict the effect of this phenomenon in the conductors. This would allow determining the resistance or inductance variations knowing, for example, the current in the bar supplied with DC frequency. For instance, one of the most common approaches is the use of analytical equations to establish relationships between R_{ac} and R_{dc}. The easiest case to develop these analytical equations is for a rectangular conductor. Equation (2.7) is the analytical formula to calculate the skin depth for this case. Based on this parameter, some literature propose formulations that enable to calculate the effect of this penetration in the resistance. A formula is proposed in [4], [13] and [19] to model the ratio of AC to DC resistance as well as the reactance. These equations are

$$K_{\mathrm{R}} = \frac{R_{ac}}{R_{dc}} = \frac{h}{\delta} \frac{\sinh\left(2\frac{h}{\delta}\right) + \sin\left(\frac{h}{2\delta}\right)}{\cosh\left(2\frac{h}{\delta}\right) - \cos\left(\frac{h}{2\delta}\right)} \text{ and} \tag{2.8}$$

$$K_{\mathrm{X}} = \frac{X_{ac}}{X_{dc}} = \frac{3h}{2\delta} \frac{\sinh\left(2\frac{h}{\delta}\right) - \sin\left(\frac{h}{2\delta}\right)}{\cosh\left(2\frac{h}{\delta}\right) - \cos\left(\frac{h}{2\delta}\right)}. \tag{2.9}$$

Where h is the height of the conductor and δ the skin depth.

In spite of (2.8) and (2.9) showing good accuracy, they are limited to the case of the rectangular conductor, which is not that common. Hence, new approaches are required to determine analytically the influence of the skin effect. The most typical method is known as the multilayer approach and is described in [4], [8] and [3] among others. This method consists in dividing the conductor into many rectangular shapes, each

of them thin enough to ensure that the current density in the layer is homogeneous. The resistance is calculated with

$$R_{\mathrm{i}} = \frac{1}{\sigma} \frac{l_{\mathrm{stack}}}{b_{\mathrm{p}} h_{\mathrm{t}}} \,, \tag{2.10}$$

where b_{p} is the width of the layer, h_{t} the height of the layer, σ the conductivity of the conductor material and l_{stack} the depth of the conductor. The inductance of each layer is calculated with

$$L_{\mathrm{i}} = \frac{\mu_0 l_{\mathrm{stack}} h_{\mathrm{t}}}{b_{\mathrm{p}}} \,. \tag{2.11}$$

Based on the value of the current in one layer, it is possible to obtain recursively the rest of the values of the current in the bar by using the data of the resistances and inductances from the different layers. When all the values of the current are known, the total losses in the conductor are easily calculated. With this magnitude and the losses in the case of $f = 0$, K_{R} and K_{X} can be calculated just dividing the AC losses by the DC ones. In figure 2.7, the multilayer approach is shown graphically. The current magnitudes are represented in this figure in a phasor diagram where the abscissa corresponds to the real part of the current and the ordinate to the imaginary. The first value of the first layer current is chosen arbitrarily to be real.

One improvement to the multilayer approach is presented in [18] and in [26], where the divisions of the conductor are not done with the same height but considering

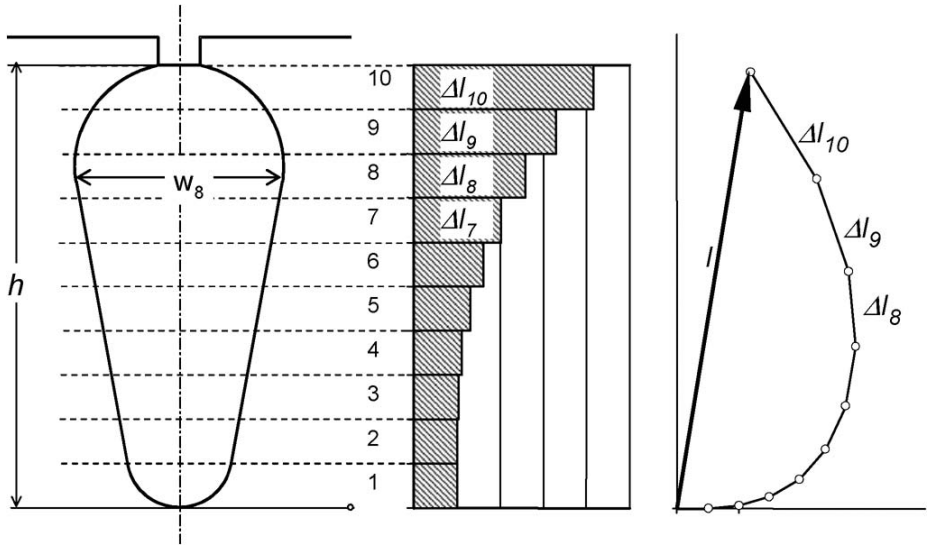

Figure 2.7: Calculation of the skin effect variation by the multilayer approach [3].

that the current density suffers bigger variations in the proximities of the surface. Therefore, the layers are thinner closer to the surface and wider in the lower part of the conductor. This reduces the calculation effort of the skin effect influence. Although the principle of the multilayer method is the same in this papers, the approach to calculate K_{R} and K_{X} is different. The conductor is divided into smaller layers but these are used to calculate an equivalent circuit that represents each layer as a branch, taking into account the coupling inductance that may appear between layers. With this equivalent model, the factors are calculated from the impedance of the circuit and the values of the resistance and inductance at 0 Hz.

The problem of these analytical methods to determine the influence of the skin effect is that they require a simulation or at least some measurements of the machine whose conductors are affected. This arises problems when the scaling of the machine wants to be done, as was mentioned in section 2.2. In order to scale a machine, the condition to fulfill is that both IMs have the same magnetic field distribution. This implies changing the input parameters of the motor such as the stator current density and the rotor frequency. Due to this frequency change, the influence of the skin effect cannot be determined by using these analytical methods as require information of the new machine. More specifically, the current density in the surface is required, but it is not available. Hence, the influence of the skin effect needs to be determined in the scaling process.

One approach that would not require information about the new machine operating conditions is the one presented in [7], where the skin effect influence is transformed from the admittance model to a transfer function. To use this method, it is required to divide the rotor bar into small simple elements like circles or rectangles and calculating the skin effect in each of them. This is done to avoid having to determine the skin effect of a shape which does not have an easy analytical formula and, instead, calculating it as a sum of smaller skin effects. With the information collected, a transfer function is particularized for the specific case, obtaining an equation in the Laplace domain that provides the complex impedance for each frequency value. However, if the machine is scaled, the transfer function may lose its accuracy.

2.3.6 Skin effect in the IM windings

In this work, the study of the skin effect is carried in the rotor bars only. The reason why the study is not done in the stator is that the main objective is to determine the influence of the skin effect or the change of the rotor topology when the scaling of the machine is performed. However, considering that the frequency of the stator current is always equal or greater than the one in the rotor currents, it could be the case of having a bigger skin effect in the stator windings. Nevertheless, as the rotor and stator have different designs for the windings, the effect of the eddy currents is not the same. The stator windings are manufactured from many turns of small conductors

connected in series and parallel that generate the whole shape. Despite the skin effect influencing the current distribution in each turn, the bulk conductor can be seen as a whole with homogeneous current density, as stated in [6] and [12]. The design of the rotor is completely different as in this case, the windings are bars of conducting material, which have a dimension big enough to allow for an uneven current density distribution. As a consequence, the study of the skin effect must be performed in the rotor bars even though the rotor frequency has values which are not that high.

Finally, the calculation of the losses in conductors affected by the skin effect must be considered. In the IM, to calculate the copper losses in the rotor bars, the current distribution in the conductor is assumed constant. However, when the skin effect influences the rotor conductors, the current distribution in them can no longer be assumed homogeneous. To take into account the skin effect properly in the calculation of the losses, the rotor bar needs to be divided into smaller regions in which the current density is constant. If a FEA is performed, these regions would be the elements of the mesh. In [33], both ways of calculating the losses in a conductor affected by the skin effect are presented. The analysis of the ohmic losses variation due to the skin effect is done in section 4.2.

2.4 Rotor bar topologies

The scaling procedure analyzed so far in this work was considering changes in the geometry of IM, temperature variations or the use of different materials in the rotor bars. However, there are some other changes in the motor that can be done like the change of the rotor bar topology. There are many different shapes for the rotor bars and each of them has different applications, therefore it can be interesting being able to scale the machine from one shape to the other just by using analytical equations.

There a few sets of rotor bar topologies that are used by the manufacturers, and the utilization of one or another depends on tests or the expertise of the company. This lack of guidelines to design the rotor bars turns into very specific rotor shapes that are seldom optimized for an application. As a result, the interest in a scaling procedure that could allow changing the design while giving a result accurate enough arises. It would allow to predict the performance of the motor with the new topologies of rotor bars without doing any additional FEA. To determine the use of this scaling, the most typical topologies and its applications are studied in order to determine how a change of the rotor design could help to increase the efficiency.

To design the machine and, more specifically, to select the rotor bar, the starting performance and the running efficiency have great importance. The parameters that are typically used to describe these conditions are the starting torque and starting current for the case of the start-up transient and the breakdown torque for the running

characteristic. All three parameters are related to the rotor resistance. However, the breakdown torque and the starting one are opposed. When the starting torque wants to be optimized, the efficiency of the machine is reduced due to the maximum torque decrease. As it is stated in [15], the rotor resistance value affects the torque speed curve of the machine. More precisely, a higher resistance of the bars will lead to a higher starting torque, but the point of maximum torque will be attached now to a point of lower speed. The effect of having the breakdown torque in an operation point with higher slip results in having a less efficient machine, as the output power is reduced for the same torque. Hence, the optimization of the torque curve requires a trade-off between starting characteristic and running efficiency, which is usually achieved by optimizing the design of the rotor bars.

As mentioned, the starting performance is not only characterized by the starting torque but also by the starting current. This magnitude is critical as it is related with the rise of the temperature in the machine windings. If the motor is a large one, the starting current can have values big enough to put in danger the integrity of the machine. In addition, a very high magnitude of the current can lead to a decrease of the buss voltage, which could compromise the stability of the grid and the operation of the machines that operate in it. Therefore, the limitation of the starting current through an optimal design of the rotor is not a trivial task, which has to be taken into account in the designing process. Achieving a design of the machine that yields a higher resistance could ensure to limit the starting current on the one hand, and on the other hand, increase the starting torque. Nevertheless, as said before, by increasing the resistance the efficiency of the machine is decreased.

2.4.1 Rotor bar selection

Regarding the rotor bar selection, there are some guidelines provided by National Electrical Manufacturers Association (NEMA) in [1]. In this standard, a classification of the motor is done in five different categories according to the specifications of the machine, which can be seen in table 2.2. The rotor bar shapes proposed for each motor design are the ones shown in figure 2.8. The rotor bars of the A type motors are normal length bars close to the surface, while bars for design B are deep ones. For class C, the bars are double cage ones and the proposed design for class D are small bars close to the surface. The rotor bar shape for class E is similar to class B bars but particularizing its design for the application to achieve higher efficiency. Based upon this classification, the manufacturers can determine which bar shapes are suitable for each application. However, in most of the cases the design process is based on experience, which is the reason why there are some predefined rotor bar designs that are the widely used by manufacturers.

Design	Slip	Locked-rotor torque (% rated-load torque)	Breakdown torque (% rated-load torque)	Starting current (% rated-load current)	Relative Efficiency	Application
Design A	0.5 - 5 %	70 - 275	175 - 300	Not defined but high	Medium or high	Fans, blowers, centrifugal pumps and compressors, motor-generator sets, etc. where starting torque requirements are relatively low
Design B	0.5 - 5 %	70 - 275	175 - 300	600 - 700	Medium or high	Fans, blowers, centrifugal pumps and compressors, motor-generator sets, etc. where starting torque requirements are relatively low
Design C	1 - 5 %	200 - 250	190 - 225	600 - 700	Medium	Conveyors, crushers, stirring motors, agitators, reciprocating pumps and compressors, etc., where starting underload is required
Design D	5 - 8 %	275	275	600 - 700	Low	High peak loads with or without flywheels such as punch presses, shears, elevators, winches, hoists, oil-well pumping and wire drawing motors
Design E	0.5 - 3 %	75 - 190	160 - 200	800 - 1000	High	Fans, blowers, centrifugal pumps and compressors, motor-generator sets, etc. where starting torque requirements are relatively low

Table 2.2: NEMA motor classification [1].

Among the different basic shapes that are used in the design of the rotor bars, there are three highlighted. These are most utilized and can be seen in figure 2.9. There is a relation between the designs proposed by NEMA and the ones shown in the figure. The rectangular (a) and the oval (b) shapes correspond to the design A or B depending on the length. The round shape (c) of figure 2.9 corresponds to NEMA design D. The double bar cages used by manufacturers and that correspond to NEMA design C are studied in section 2.4.3.

Analyzing figure 2.9, the simplest one is the rectangular shape, which is useful to understand the trade-off described before in terms of starting and breakdown torque. In [9] and [30], the effect of the height (h) to thickness (a) ratio of the rectangular bar on its performance is described. Bars with a big h/a ratio have a better starting

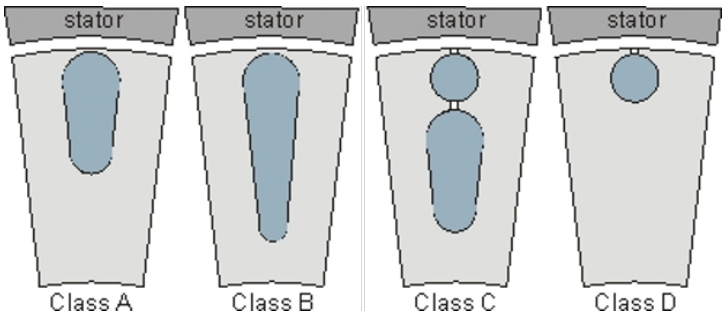

Figure 2.8: Rotor bar designs according to NEMA classification.

performance in terms of a greater torque and lower start-up current, due to the skin effect. As a result of this effect, the current does not penetrate in the whole length of the bar, instead it remains close to the surface yielding a higher current density in a smaller area. The result is having a higher equivalent resistance in the rotor bar than in the case of the same area but with a smaller h/a ratio. The modification of the ratio has a negative effect on the machine efficiency, as these modifications involve a trade-off between starting performance and running efficiency. Hence, a high h/a ratio will mean having a smaller per unit breakdown torque but, instead, a better start-up performance. However, there are other possibilities such as using more complex shapes like ones with holes, which can yield a better solution.

The problem of having a rotor bar design that enhances the influence of the skin effect to increase the resistance is that the overall efficiency of the machine would be reduced. However, sometimes this efficiency is preferred over a better starting characteristic. To increase efficiency, shapes like the one known as oval, which is shown in figure 2.9 (b), are used. According to [4], this shape is used for high efficiency drives, which do not have high rated power (usually less than 100 kW). If the rated power is not too big, the starting performance is not as critical as in other cases since the current peak during start-up is smaller. Although the oval design is suitable for machines with low rated power, if the application involves high speed, some problems arise. As stated in [21], the oval shaped rotor cage suffers in high-speed applications large rotational stresses caused by the high circumferential velocity of the rotor. This stress leads to a temperature increase and expansion of the materials in the rotor. As these have different expansion rates, mechanical stress also occurs in the materials, reducing the robustness of the machine.

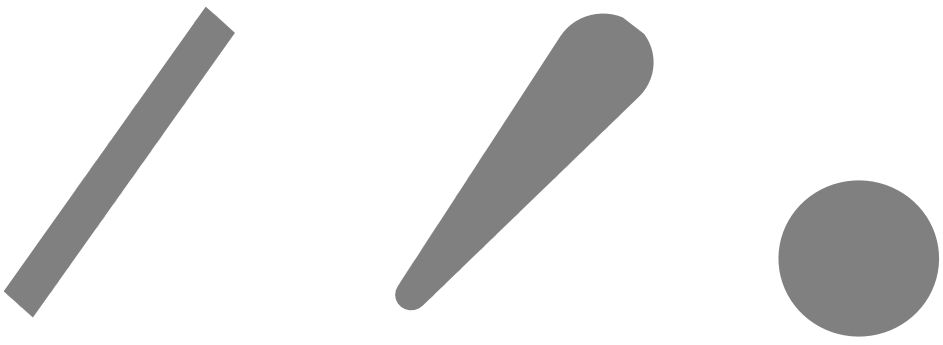

(a) Rectangular bar shape. **(b)** Oval bar shape. **(c)** Round bar shape.

Figure 2.9: Basic designs of the rotor bars.

2.4.2 High speed application

In [21], [20], [2] and [10] the problem of high-speed drives is analyzed. High-speed operation is considered the one in which the machine operates with a speed around 10000 rpm or more. The benefits of such operation is that the relation of weight for a certain magnitude of power conversion is reduced, so it is very important to achieve lower fuel consumption in transportation, as mentioned in [10]. The problem of such a high-speed application is the magnitude of the peripheral speed, which induces high stress in the materials. Therefore, one of the simplest solutions is a solid-rotor topology, which consists of a steel laminated rotor without bars. It is a very cheap and robust design, but the lack of high-conductivity path for the induced currents makes the overall electromagnetic properties not as good as other designs. For example, the slip for a certain amount of torque is much higher than other topologies, hence the skin effect is more noticeable and the current is concentrated near the surface of the rotor, increasing the losses. Another effect that increases the losses is the big amount of air-gap harmonics that concentrate on the surface. The solution presented in [21], [20] and [10] to reduce the amount of losses due to the magnetic flux harmonics is the change of the topology to what is called: slit rotor. In this design, some slots are done axially in the rotor surface. The effect that this has into the machine is the filtering of the flux harmonics, reducing the iron losses. However, it presents counter-effects such as the increase of the air-gap friction losses, the increase of the manufacturing costs, the increase of the noise and the reduced mechanical strength of the rotor.

As slitting the rotor does not solve the problem, another approach is used: the coated rotor. As it is presented in [21] and [10], by coating the rotor with a layer of conducting material such as copper, the effect created by the air-gap harmonics is reduced. This approach does not only reduce the iron losses due to the filtering of the flux harmonics, but also increases the torque production as a result of the increased rotor conductivity. Moreover, the robustness of the rotor is kept constant as no slots are created in the machine surface. Nevertheless, the coating makes the air-gap between the rotor and the stator much higher, reducing the power factor of the machine and the overall performance. To overcome these problems, the design including a squirrel cage is introduced in [20] and [2]. In this case, round holes are drilled into the rotor and casted with conductive material such as copper or aluminum. By doing so, the conductivity is increased, the air-gap is reduced and the losses decreased. However, in order to be able to drill this holes, it is required making the rotor out of layered plates or the manufacturing process would be too expensive. Compared to the oval shape, the round one offers a smaller surface and hence decreased stresses. In addition, the stresses can be reduced, as mentioned in [2], by a proper design of the end rings of the machine. For all these reasons, the round shape that is shown in figure 2.9 (c) is the one preferred for high-speed applications.

2.4.3 High starting current

To avoid thermal stresses because of the high losses in the start-up of machines with high rated power, it is convenient having a greater resistance in the rotor. However, in order to have better efficiency during normal operation it is more convenient to reduce it. Although this trade-off seems inevitable, the use of the skin effect can overcome this problem. Considering that during the start-up of the IM the currents induced in the rotor have the same frequency as the ones in the stator because there is no mechanical rotation, the influence of the skin effect is quite big, yielding a higher resistance. Nevertheless, when the machine reaches its normal operation, this frequency is highly reduced, having the resistance a much smaller value.

To enhance the skin effect in the rotor bars and increase the resistance during machine starting, some shapes such as the ones in figure 2.10 were developed. These bar shapes correspond to the design C proposed by NEMA in table 2.2. By choosing the designs from figure 2.10, the rotor has now two cages, one that will participate more in the starting and the other that will predominate during the steady state. In both cases of figure 2.10, the outer cage determines the behavior of the machine during the starting transient, because the skin effect forces the current to remain in the surface. Since the area of the exterior bar is smaller, the resistance will be bigger and the starting current will be smaller than in the case of a simple bar. Once the steady state is reached, the frequency of the rotor currents would be much smaller, leading to a reduce skin effect and a more homogeneous distribution of the current along the entire bar. During this stage, the inner bar is the one that determines the behavior of the rotor, providing a better steady state performance and a higher value of efficiency.

There are other possibilities to reduce the start-up negative effect in the machine that are not related with the change of the shape of the rotor bar. For example, one of the approaches that has been used for quite a long time is the wye-delta or star-delta connection. The working principle is changing the connection of the phases of the

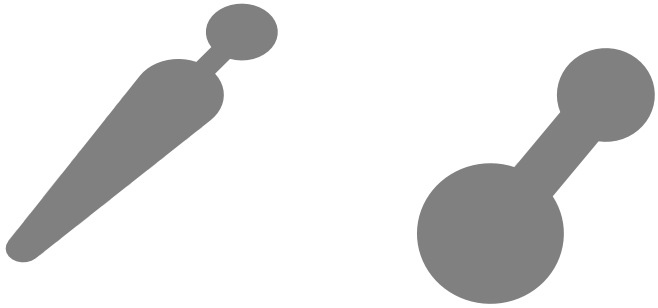

(a) Boucherot bar shape. **(b)** Double round bar shape.

Figure 2.10: Double cage designs for start-up.

motor. To achieve a start-up with reduce voltage and smaller peak current, the wye linkage is used. While the steady state is done with delta connection, thus normal voltage. The problem of this method is that the starting torque is reduced by 3, which could even lead to the machine not being able to overcome the initial load torque. Therefore, this method has been slowly replaced by the inverter start-up, which varies the frequency of the supply to achieve a slow start-up without a peak of current. As a result, if one of these approaches is done, the use of a double cage is not needed anymore.

To sum up the selection of the rotor bar shape, in table 2.3 the main application for the most common rotor designs can be observed. Nevertheless, it must be noted that these are some of the options chosen usually by the manufacturers, but there are many more possibilities. For instance, each shape can be optimized for a certain application using methods like the ones explained in [37] and [17]. On the one hand, in [17] a deterministic optimization method was used to maximize the ratio of $T_{\text{rated/starting}}$ but also considering constraints such as the maximum starting current, efficiency, etc. On the other hand, in [37] the same algorithm is used but to optimize a cost function. In both cases having an initial design that is quite suitable for the application can lead the optimization algorithm to an improved solution that reaches a better performance. However, this approach requires particularizing each rotor topology for a specific application, increasing the design costs. Moreover, the manufacturing process would also be altered as each shape of the rotor bar is different, making this approach unsuitable for mass production. The optimization of the rotor shape to achieve maximum performance is an interesting concept, which could be applied to machines that do a critical task in a company, but not to mass production.

2.4.4 Material selection

So far, the influence and the importance of the rotor shape has been analyzed for the different operations of the machine and applications. However, other variables can be modified such as the material of the mentioned slot. The two most common materials for the rotor bars are copper and aluminum, but alloys with different proportions of these two can be made. The direct effect of changing the material of the rotor bar

Bar Geometry	Rated power	Maximum speed	Starting current
Rectangular	Low-medium	Medium	Medium
Oval	Low-medium	Medium	Low
Round	Low-medium	High	Low
Double round	Medium-High	Low	High
Boucherot	Medium-High	Low	High

Table 2.3: Rotor bar shape characteristics.

is the variation of the conductivity and, hence, the resistance. For example, copper is usually used to achieve higher efficiencies, but its better conductivity leads to a smaller resistance, which can cause high currents peaks during start-up, as said in [15]. To reduce the negative effect of the better conductivity, aluminum can be used to achieve higher resistance. There are also more complex approaches depending on the requirements of the application and the type of motor. For instance, the material can have a big influence in the case of double cage rotors. The connection between the two cages and the materials used can change completely the performance of the motor. As it is stated in [11], there are several options when manufacturing the double cage of the rotor. One of the possibilities is using just one material for both cages, but another different approach is using distinct materials. In the case of a critical starting, the use of copper in the inner bar and aluminum in the outer bar is a very interesting approach as the resistance during start-up would be even higher and the rotor losses would diminish during steady state due to the better conductivity of copper. Although this idea could highly improve the operation of the IM, the results obtained in [11] do not show a clear advantage. The viability of this approach depends on the application, manufacturing costs and many other factors that change for each individual case.

After the revision of all the different designs of the rotor bars and the use of each of them, it can be concluded that the selection of a rotor shape is not a trivial task, which cannot be generalized. Therefore, it is necessary to know the requirements of the motor, the application, etc. As mentioned in previous chapters, when designing a motor, this is typically done by a FEA. If for each rotor design the whole $T - n$ map must be simulated, the computational cost would be extremely high. Thus, it would be very interesting developing a scaling procedure, like the one for the radial and axial dimension, to enable the variation of the geometry without the need of doing the whole simulation.

3 Methodical procedure

As the main goal of this work is to develop an improved set of analytical equations that allow for a better scaling of the machine, it is obvious that it is required a set of simulations to compare the results. To do so, it is necessary to understand the modeling and the simulation process, which is the objective of this chapter. More precisely, the design of the IM is going to be reviewed first, then the simulation procedure will be described, and finally the post-processing of the results will be explained.

3.1 Modeling process

Since the analysis of the skin effect is a big topic in this work, the simulation of different machine models is required as the shape is a critical parameter of it. Hence, it is convenient to have a modeling tool that allows generating the different geometries of the machine to perform the FEA afterwards. The program chosen to do the different modeling of the topologies is the software ANSYS©. With the aid of this tool, a script, which contained the different geometry models for rotor and stator designs is developed. This code allows the user to change from one shape of the rotor and stator windings to another. Moreover, the user can modify the geometry specifications to adapt each design to the required size.

The different topologies of the rotor windings were the ones described in section 2.4, which could be seen in figures 2.9 and 2.10. Regarding the different stator winding designs, they can be observed in figure 3.1. The geometry in (a) is the classical trapezoidal winding, the one in (b) is the inverted trapezoidal winding and finally in (c) the parallel flanks design can be observed. Each of them has different characteristics in terms of manufacturing process, performance of the machine, etc. but the description of each one is beyond the scope of this work. Despite having different designs for the stator windings, all the simulations have been carried with shape (a) of figure 3.1. The reason is that the influence of the skin effect in the stator windings is not the objective of this work, only its effect in the rotor bars.

(a) Stator winding shape with trapezoidal teeth.

(b) Stator winding shape with inverted trapezoidal teeth.

(c) Stator winding shape with parallel flanks.

Figure 3.1: Stator windings design.

Due to magnetic and structural symmetry of the machine, only a part of it is simulated, as shown in figure 3.2. This results in less computational effort. Another approach to reduce the simulation time is the calculation of the 2-D representation of the machine instead of the 3-D. The resulting model is divided into different parts, which are named labels, having each of them specific properties, material, mesh, etc. Each label of the machine is represented in figure 3.2 (a) with a different color. The different labels (not all are represented in the figure) used for the machine design are: shaft, rotor core, rotor bars, rotor slot (not all geometries have it), air gap (divided into 3 areas), stator slot, stator core, stator windings and stator exterior space (to set boundary conditions). Different labels for each material or area of the machine provide a big advantage as it allows having different mesh sizes for each label. The benefit of the variable mesh size comes from the point of view of the computational effort, as it enhances having less node density in the elements that are not interesting and more detail in the important ones. In this work, the rotor bars require a big quantity of data. Hence, a denser mesh is used to increase the number of elements, and as a result, the accuracy in the simulations. An example of the meshing of the machine can be seen in figure 3.2 (b). In the case of the rotor bars, it can be seen that the mesh has much more density, creating more elements (triangles connecting the nodes).

To scale the machine design, the ANSYS© script that creates it, allows introducing this modification. The only scaling procedure that affects the machine design is the geometrical one, specifically the radial. Although the axial is a geometrical scaling as well, because the representation is in 2-D, the geometry is not affected. This axial scaling and changes in the materials, conductivities, temperatures, etc. are introduced in a later stage, not in the geometry design.

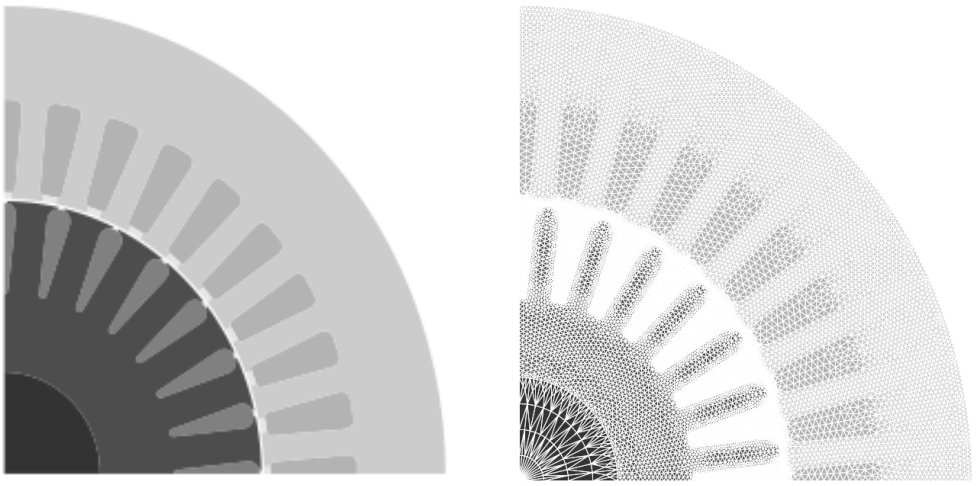

(a) Design example of the simulated machine.

(b) Grid example of the simulated machine.

Figure 3.2: Machine design for the simulation.

3.2 Simulation and post-processing

The FEM is executed after the machine is designed, meshed and the materials' properties are assigned. The FEA is carried out making used of the non-linear hybrid method that was described in chapter 2. The no-load simulation is performed first to obtain the initial rotor flux solution, which is used as the starting point of the transient FEA of the entire operation map. Instead of calculating the $T - n$ map, the input parameters are the different $\hat{J}_1 - f_2$ combinations. Following this approach, 12 no-load simulations are executed, each for each stator current density value. Based upon these results, the operation map is calculated. The values of this map are 15 different rotor frequencies combined with the 12 stator current densities that were mentioned, making a total of 180 simulations. These simulations are done running a Python program that uses iMoose, the IEM's (Institut für Elektrische Maschinen) own solver. Among the magnitudes obtained for each operation point, there are the magnetic vector potential solution, the current density distribution in the rotor bars, the lumped parameters of the model, etc.

If a scaled machine is simulated, the methodology is very similar but with some modifications that depend on the magnitude to scale. When the factor scaled is the radial dimension, this variation must be included in the design stage. After this point, the input parameters should be modified considering the scaling factors before the simulation of the machine. Therefore, the parameters such as the frequency, current and conductivity are modified according to table 2.1. The simulation of the scaled machine is used to validate the scaling procedure, as it allows comparing it with the reference motor. This is not necessary as the method is already validated, like

many papers cited in chapter 2 proved. However, for the purpose of this work, some improvements are introduced in the scaling methodology. Hence, the new scaling needs to be validated. For this reason, two simulations are carried in each case, one of the reference machine and one of the scaled device.

After the FEA, the post-processing of the solution is done with the software Matlab©. At this stage, the different magnitudes of the machine operation such as the ohmic losses in stator and rotor, iron losses, torque, effective values of the current, etc. are calculated. The calculation of the iron losses is done according the methodology introduced in chapter 2: the transient formulation of the iron loss calculation. As shown in (2.1), the iron losses are divided in three terms that enable reducing the computational effort. Regarding the calculation of the copper losses, a more detailed review will be done in the following chapters.

All the parameters obtained in the post-processing are first calculated in the $\hat{J}_1 - f_2$ map and then converted into the $T - n$ one. Considering the operation limits of the converter and other components, the complete operating map of the motor is calculated. If the scaling of the drive was performed, is in this post-processing step where the comparison of the solutions could be done. To compare the reference and the scaled machine is necessary to modify one of them. For example, the scaled machine can be transformed back into the reference by using the inverse scaling factors in the analytical equations. The other approach is scaling the reference machine with in the post-processing with the same parameters used to scale before the FEA.

A summary of the whole procedure can be seen in figure 3.3, which is particularized for the case of doing a simulation with scaling. This would be used to introduce a methodology to analyze the skin effect influence and the consequences of the geometry changes of the rotor bars. In the case of study of the reference motor or just one that does not want to be compared, the stages of the scaling should be avoided in the workflow.

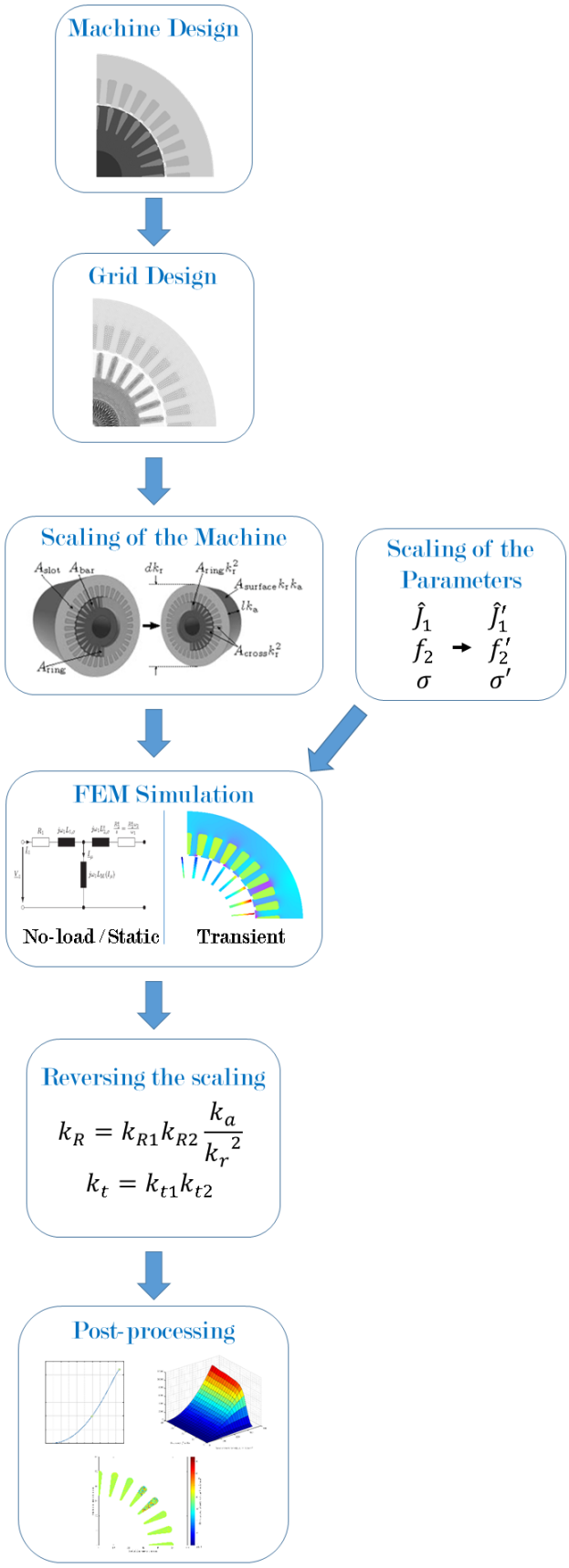

Figure 3.3: Procedure of the simulations.

4 Skin Effect

The skin effect is a phenomenon that particularly affects the rotor bars of an IM. As a result, the entire machine condition depends on it. Therefore, it is very important to characterize the effect, specially how affects the scaling procedure of the machine since this is a very interesting approach when dealing with simulations and design of machines. To determine the skin effect influence, several rotor designs are simulated in this chapter to study the different influence of the shape and other parameters. After that, the influence of the uneven current distribution in the losses is analyzed, and different approaches to calculate them are tested. Finally, the influence of the skin effect in the scaling procedure is determined.

4.1 Simulation of the skin effect

In chapter 2, the causes and the consequences of the skin effect on the machine operation were analyzed. According to literature, this phenomenon depends on several parameters: the frequency, the material of the conductor, the shape of it and its size. The effect of each parameter in the rotor bars of an IM must be analyzed to determine its influence in the machine operation. Moreover, the current distribution of the bars is also studied to see its repercussion in the losses.

The frequency, which is the parameter that characterizes the skin effect, is analyzed for the case of the IM. Two frequencies affect the conductors of the machine: the stator and the rotor frequency. In the case of the stator windings, these are only affected by the supply frequency. However, as said in section 2.3, the study of the stator windings is not the objective if this work. Therefore, the only conductors in which the skin effect is studied are the rotor bars. The frequency that influences in this case is the rotor one, which can be calculated as

$$f_2 = f_1 - n \cdot \frac{2\pi}{60} \,. \tag{4.1}$$

If the machine is studied in the $T - n$ map, f_2 depends on both the mechanical speed and the stator frequency according to (4.1). Thus, variations of n and f_1 affect its value. However, as the machine is simulated in the $J_1 - f_2$ map, one of the input parameter is directly the rotor frequency, hence independent from other magnitudes.

The relation between the frequency and the skin depth was reviewed in (2.7). This formula shows the relation of the frequency with the skin effect, seeing a stronger influence as the frequency is increased. Although this equation is particularized for the case of the rectangular conductor, it is an analytical calculation that can be used to predict the tendencies in some other cases. Thus, it can be concluded that for every bar topology, the bigger the rotor frequency, the more noticeable the skin effect is. For this reason, the phenomenon is studied in simulations with a high value f_2. Particularly, the skin effect is studied at $f_2 = 30\text{Hz}$, if the entire operating map is not calculated. The effect of the frequency in the current distribution of an oval bar can be observed in figure 4.1, where in picture (a) an even current density is observed for the similar scale as in figure (b).

It can be observed in figure 4.1, that both simulations have different frequencies but the same value of J_1. This factor does not affect the skin depth, as it is only determined by the variations in the value of the rotor current density. As the skin depth is the distance for which the current density is reduced by $1/e$, it does not depend on the magnitude of the current, but in the changes of it. However, the bigger J_1, the easier to study the skin effect as the changes will be more noticeable. Thus, all the simulations in which the phenomenon is studied, are performed with a high value of the stator current density to help visually to detect the changes in the magnitudes.

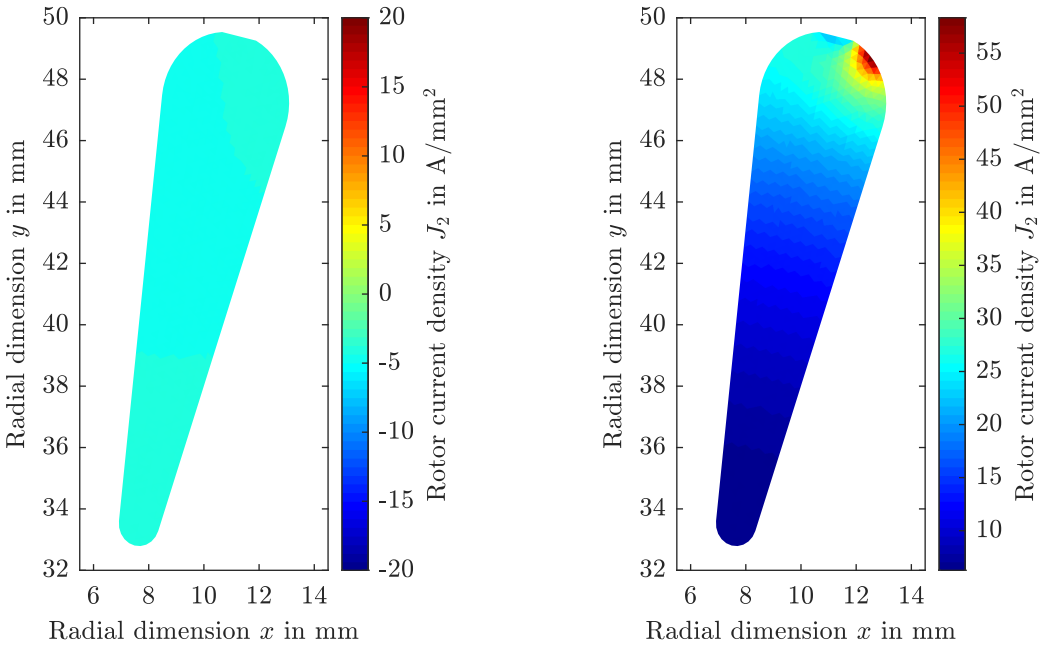

(a) $J_1 = 14.5\text{A/mm}^2$ and $f_2 = 1\text{Hz}$. **(b)** $J_1 = 14.5\text{A/mm}^2$ and $f_2 = 30\text{Hz}$.

Figure 4.1: Rotor current distribution of the oval shape.

Regarding the other factors that affect the skin effect, the simulation of different topologies is required to perform the analysis. To determine the influence of the shape, the five rotor topologies showed in figures 2.9 and 2.10 are simulated. Some examples of the results of these simulations can be seen in figures 4.2, 4.3 and 4.4. As shown in the different figures, the current distribution along the various designs changes even though the bar position, time instant and input parameters are the same. More specifically, the current distribution inside the bars of the round shape in figure 4.3 is more homogeneous than in the case of figures 4.4 or 4.2. Furthermore, the Boucherot bars present a bigger variation than the double round rotor. Therefore, it can be stated that the shape affect the distribution of the current. To obtain a more detailed analysis of the current distribution, the losses of the different topologies are studied in section 4.2. Furthermore, the influence of the size will be studied by analyzing the scaling of the machine.

One interesting effect that can be detected in the simulation results are small spots in which the current density has a value that differs considerably compared to the rest of the magnitude. This is the case of the white spot observed in the top right corner in figure 4.1 (b). This area contains a high current density in small surface of the bar, but in the literature it is said that rectangular regions of the bar that go from the surface to the core have a similar current density distribution if they are small enough. The reason for this effect is that the conditions of the simulation are

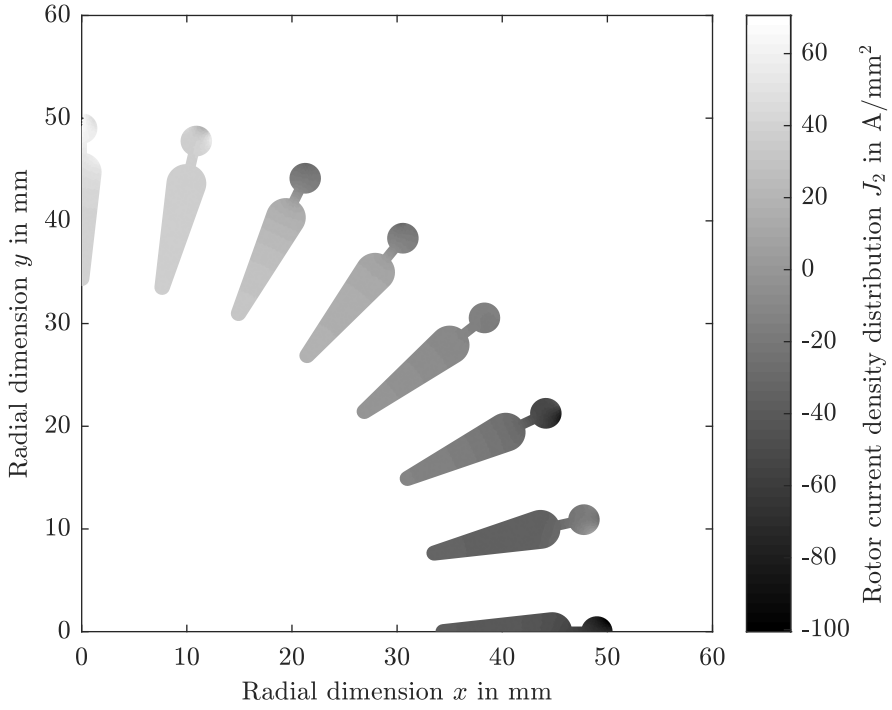

Figure 4.2: Rotor current density distribution in the Boucherot bars at $J_1 = 14.5\text{A/mm}^2$ and $f_2 = 30\text{Hz}$.

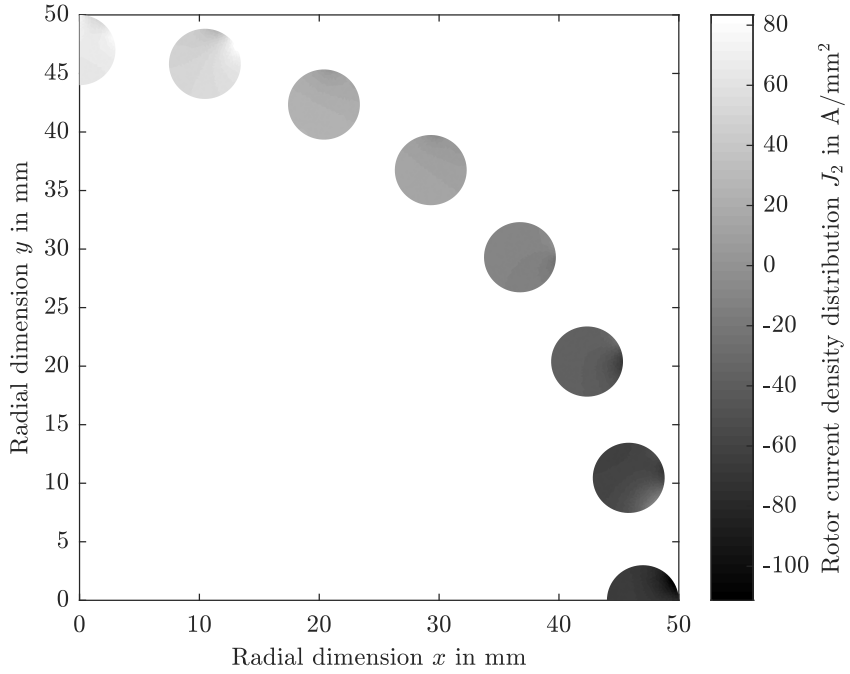

Figure 4.3: Rotor current density distribution in the round bars at $J_1 = 14.5\text{A/mm}^2$ and $f_2 = 30\text{Hz}$.

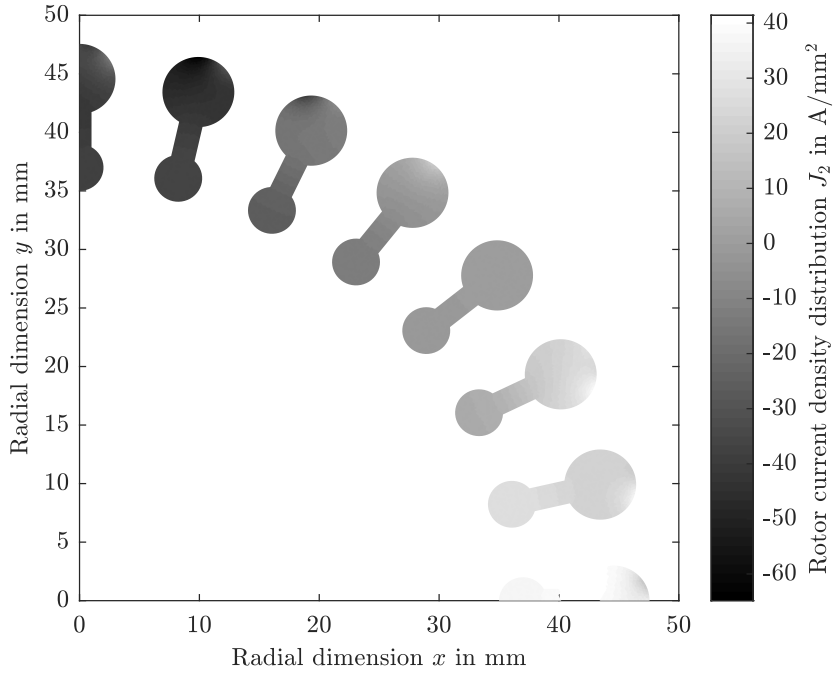

Figure 4.4: Rotor current density distribution in the double round bars at $J_1 = 14.5\text{A/mm}^2$ and $f_2 = 30\text{Hz}$.

not the same in the literature. In the case of the figures shown in this work, they are extracted from simulations of the whole machine. Hence, the interactions between the different elements are considered, giving other results as if the conductors were simulated isolated. From this interaction between the stator teeth and the rotor, some flux pulsations occur as result of the change of the magnetic path due to the rotation of the machine. As the reluctance changes constantly, the flux pulsations take place modifying the current values. The result of this phenomenon is the change of the current density distribution due to the flux pulsations caused by the inductance variation of specific areas.

The current density distribution inside the bars of the figures show a gradient that must be studied. For example, in the case of figure 4.1 (b), the values of the current are higher in the surface than in the lower part of it. This is the expected result according to the literature review, as the current is pushed out of the inner part of the bar due to the uneven flux distribution. However, in simulations like the one in figure 4.2, in some bars the current has higher values closer to the shaft or it suffers a change in the polarity. During the literature review of the skin effect, some papers showed simulations with this phenomenon, but without any physical explanation. Nevertheless, in [12] this effect is analyzed for the case of a stator winding. As said before in this work, the case of the stator winding is not the same as the case of the rotor bars because of the differences in the manufacturing. However, the explanation given can be used to describe the phenomenon that appears in the rotor bars. The reason is that the uneven current distribution in the bar causes a potential difference between the top and the bottom part. This voltage leads to circulating currents that could circulate in the opposite direction of the main current at the top of the bar and in the same direction at the bottom of it.

It is to do a more detailed study of this effect and particularize the results for the rotor bars of an IM, since the lack of literature explaining this phenomenon makes it necessary. However, this aspect is beyond the scope of this work. Also, it is still possible to analyze the skin effect since the polarity change of the currents does not affect all bars. Moreover, to determine the effects of the scaling, it is necessary to compare the reference machine and the scaled one. Therefore, if both suffer the same effect it will not affect.

4.2 Losses calculation

One of the most important aspects of the skin effect and, as a result, of the uneven current density distribution is that the losses of the rotor bars cannot be calculated as in a conductor supplied with DC current. The reason why this happens was explained

in chapter 2 and is due to the different resistance in sections in which the bar does not have the same current density.

4.2.1 Calculation of DC losses

If a conductor is supplied with DC current, the losses are calculated as

$$P_{\mathrm{Cu},2} = N_2 \cdot R_{\mathrm{bar}} \cdot I_2^2 \,, \tag{4.2}$$

where N_2 is the number of rotor bars, R_{bar} is the resistance of each bar that can be calculated with

$$R_{\mathrm{bar}} = \frac{l_{\mathrm{bar}}}{\sigma A_{\mathrm{bar}}} = \frac{l_{\mathrm{bar}}}{\sigma \sum_{i=1} A_{\mathrm{i}}} = \sum_{i=1} \frac{l_{\mathrm{bar}}}{\sigma A_{\mathrm{i}}} \tag{4.3}$$

and I_2 is the current circulating through the bar. In (4.3), l_{bar} is the length of the bar, σ the conductivity and A_{i} is the area of each element in which the bar is divided when the FEA is done. If the rotor is supplied with zero frequency, the current can be calculated with

$$I_{\mathrm{avg},2} = \bar{J}_2 \cdot A_{\mathrm{bar}} = \sum_{i=1} J_{2,\mathrm{i}} \, A_{\mathrm{i}} \,, \tag{4.4}$$

since the current density distribution is homogeneous. The parameter J_{i} of (4.4) is the current density of each element.

4.2.2 Calculation of AC losses

If the current supply has non-zero frequency, the calculation of the losses is more complex. The reason is that having a current density distribution that is not homogeneous, leads to uneven losses in the different areas of the conductor. To calculate the losses as in (4.2), the equivalent resistance of the bar and the equivalent current value must be obtained. Although the total area is the sum of the areas of the elements, the equivalent current cannot be calculated in the bar as in the DC case without losing precision. Since the area of each element is different and has an own value of current density, using (4.4) will yield errors in the value of the losses.

The approach to calculate the rotor ohmic losses properly is presented in [33], in which two different equations are introduced to calculate the losses. The first equation is

$$P_{\mathrm{Cu,2,\bar{J}}} = \sum_{i=1} (\bar{J}_2 A_\mathrm{i})^2 \cdot \frac{l_\mathrm{bar}}{\sigma A_\mathrm{i}}, \tag{4.5}$$

which is used to calculate the losses in the case of a conductor supplied with DC current. Considering the definition of the resistance (4.3) and the calculation of the bar current (4.4), and substituting these 2 equations into (4.2), (4.5) is obtained. Thus, (4.5) is the formula to calculate the DC losses in a finite element solution. This equation is also used in cases where the skin effect takes place to determine the error induced from averaging the current in the bar. This value of the losses calculated with the DC formulation when the supply is AC will be named average losses.

The equation proposed in [33] to calculate the losses considering the influence of the skin effect is

$$P_\mathrm{Cu,2} = \sum_{i=1} (J_\mathrm{2,i} A_\mathrm{i})^2 \cdot \frac{l_\mathrm{bar}}{\sigma A_\mathrm{i}}. \tag{4.6}$$

In this formula, the first term is equivalent to the current in the element, and the second the resistance of it. Hence, in this equation the losses of the bar are calculated as the sum of the ones in each element. In order to have a formulation that is equivalent to the one in (4.2), the term efficient current is defined. This magnitude is equivalent to the DC average current but for the case of AC supply. The effective current is calculated as

$$I_\mathrm{eff,2} = \sqrt{\sum_{i=1} (J_\mathrm{2,i}^2 A_\mathrm{i}) \cdot A_\mathrm{bar}}\,. \tag{4.7}$$

By making use of this definition, the effective losses can be expressed as the product of I_eff times the resistance. Operating this formulation as

$$P_\mathrm{Cu,2,bar} = I_\mathrm{eff,2}^2 \cdot R_\mathrm{bar} = \sum_{i=1} (J_\mathrm{2,i}^2 A_\mathrm{i}) \cdot A_\mathrm{bar} \cdot \frac{l_\mathrm{bar}}{\sigma A_\mathrm{bar}} = \sum_{i=1} (J_\mathrm{2,i} A_\mathrm{i})^2 \cdot \frac{l_\mathrm{bar}}{\sigma A_\mathrm{i}}, \tag{4.8}$$

the result is the same as in (4.6).

4.2.3 Comparison of the losses calculation methodologies

By making use of the formulas described, the average and the effective losses of the simulations are compared, and the repercussion of the skin effect determined. The losses of the entire J_1-f_2 map are compared for one bar case, specifically the oval shape. However, the analysis of other bar topologies yields similar results. The rotor average losses calculated with (4.5) are shown in figure 4.5, while the effective calculated with (4.6) are presented in figure 4.6. The difference between the effective losses and the average ones is observed in figure 4.7. Analyzing the comparison, there is a tendency for the losses value depending on the frequency and the stator current density. As explained in section 2.3, the higher the frequency, the bigger influence of the skin effect. Hence, the values of the current density between the elements have higher differences. Since the average losses calculation method does not account for the uneven current distribution, the losses in this case are smaller than in the case of considering the losses in each element. The same reasoning applies for the increase of the losses due to the increment of the stator current density. Despite this magnitude does not affect the influence of the skin effect, considering that the rotor current density is higher, the absolute value of the difference between the elements will be higher yielding the results observed in figure 4.7.

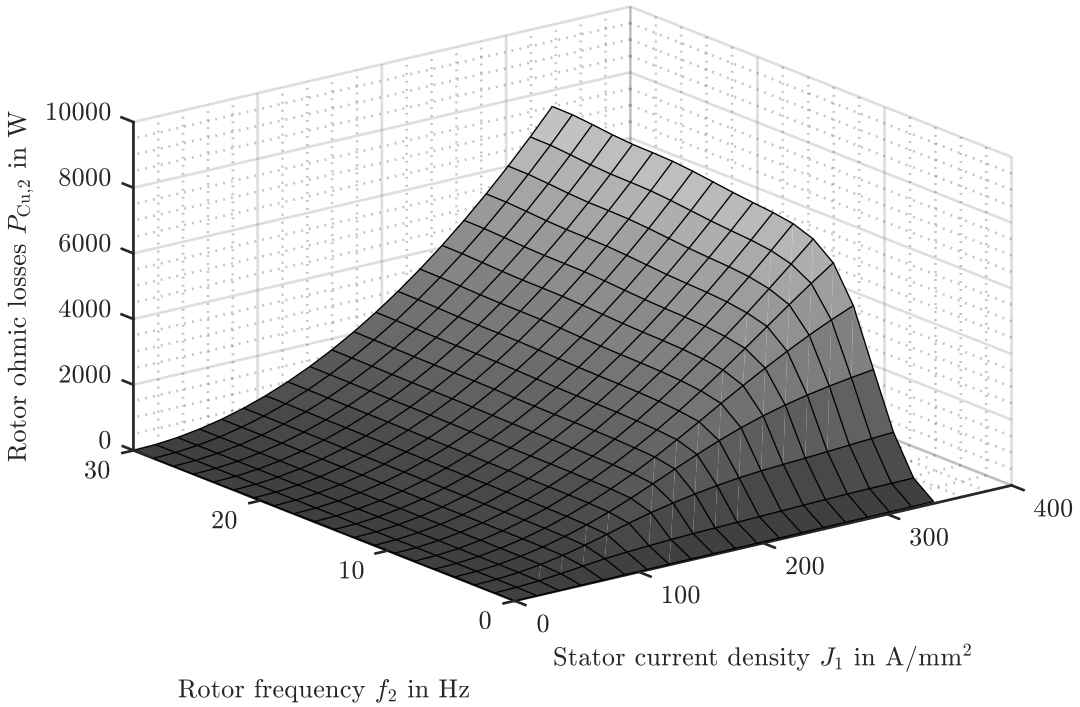

Figure 4.5: Rotor average copper losses for the oval shape.

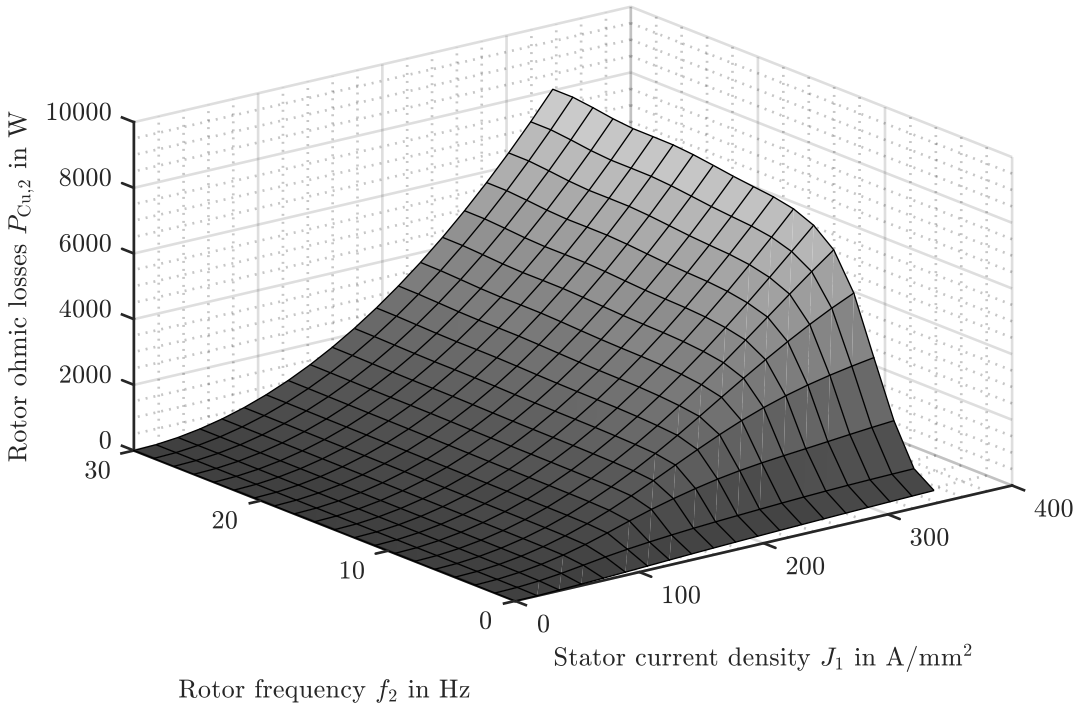

Figure 4.6: Rotor effective losses for the oval shape.

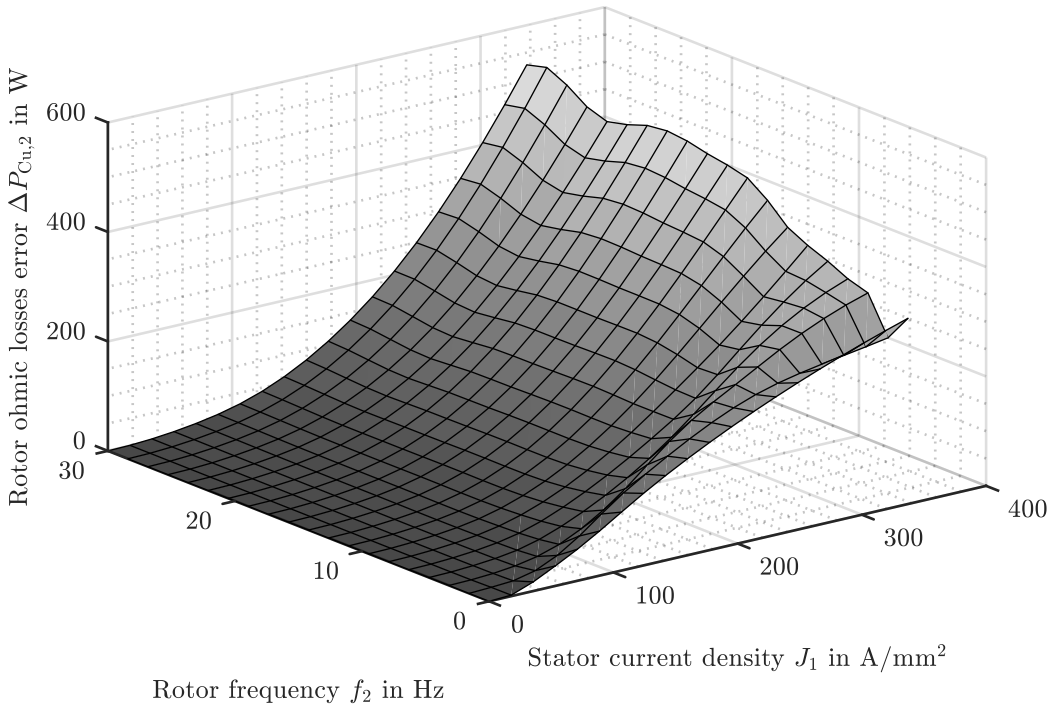

Figure 4.7: Rotor losses difference for the oval shape.

In order to determine the influence of the error of calculating the average losses instead of the effective ones, the results are transformed from the J_1-f_2 into the T-n map. This transformation is not only done changing the parameters from one reference to the other, but taking into account the limitations of the supply of the motor. More specifically, the maximum line current, the maximum voltage of the inverter considering the drop in the resistances, the maximum torque and the maximum speed. With this consideration, the number of possible operation points is reduced, since the constraints must be respected. The result of the losses difference in the T-n map can be observed in figure 4.8. In this map there are some interesting magnitudes for the control such as the maximum ampere (MA) or the maximum torque per current line (MTPCL), which establish the control limits and the most efficient curve respectively.

Regarding the map, it must be highlighted that the influence of the skin effect is not considered for the control purposes. This means that the effect of the change of the inductance of the rotor bars is not taken into account to establish the control limits. The reason is that this map is meant to give an order of magnitude of the

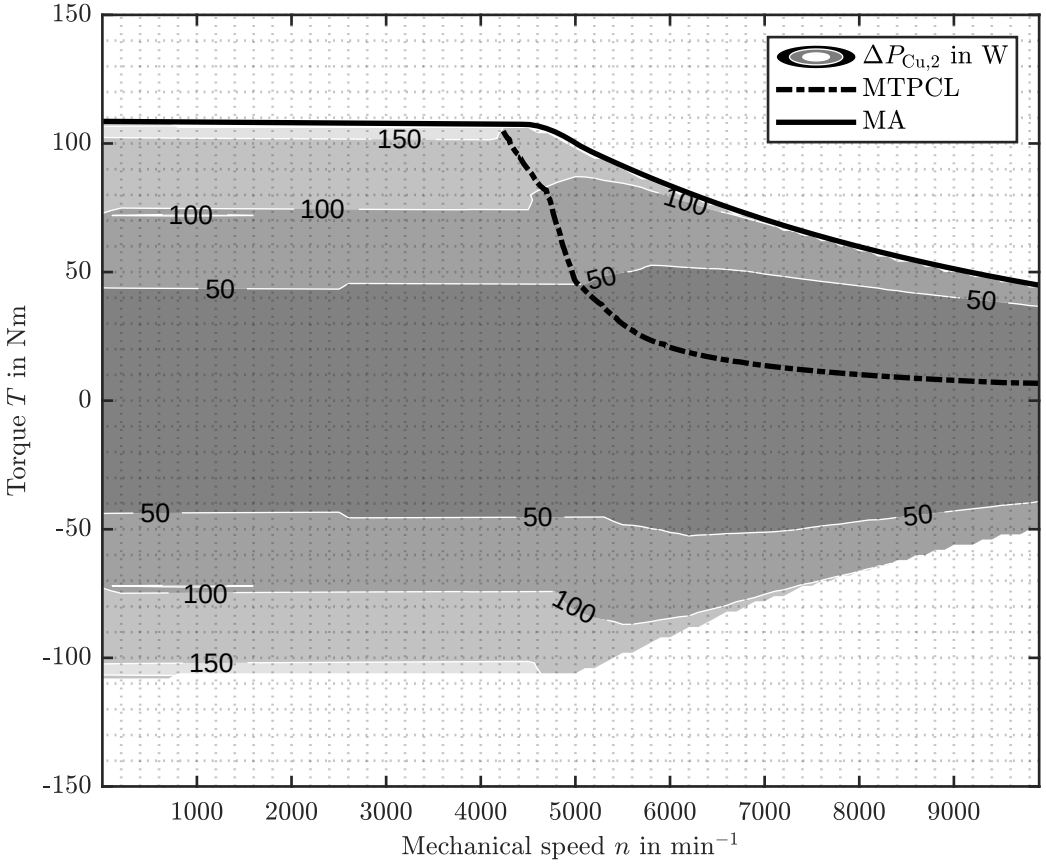

Figure 4.8: Rotor losses difference for the oval shape in the operation map.

losses difference in the real operation of the machine, not to perform a precise control of the engine. In figure 4.8, the losses difference of the operation map of the engine can be observed. At some points, the value of the losses difference is translated in a 10% of the total losses of the rotor. Hence, the control of the machine could not be applied correctly if the average losses are the ones calculated, without considering the skin effect.

4.2.4 Shape influence in the skin effect

In this section, the calculation of the losses has been carried out considering the influence of the skin effect. Therefore, by studying the losses, information about this phenomenon is obtained. As analyzed in section 2.3, the shape of the conductor is a parameter that influences the eddy current distribution, and hence, the skin effect. Comparing the losses of each geometry at the same supply conditions, information of the distributions of the current density in the different bars is obtained. Analytically, bars in which the skin effect has a higher influence, have greater values of the losses. The results shown in figure 4.9 demonstrate that the shape has a considerable influence in the eddy currents magnitude and distribution. It is remarkable that the geometries, which have similar design such as the Boucherot, the double round and the oval, have similar losses. However, the rectangular and the round shape have much higher ones. Regarding the rectangular, as explained in section 2.4, this shape is used in start-up of machines where high resistance, thus high skin effect, is desired. Analyzing the round shape, figure 4.9 shows that is the one with more losses. The explanation is that the design has a high surface/size ratio, therefore the majority of the current density is distributed along the surface, leading to a higher resistance, and hence more losses.

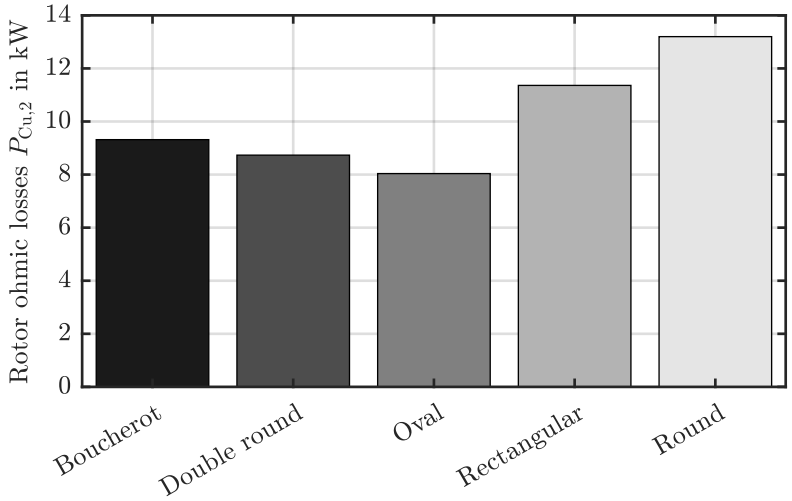

Figure 4.9: Rotor cooper losses at $J_1 = 14.5\text{A/mm}^2$ and $f_2 = 30\text{Hz}$.

However, analyzing the different geometries based of the value of the total ohmic losses is inaccurate since each rotor bar design has an area and therefore, bigger areas are expected to have greater losses than the smaller ones. In order to avoid an imprecise comparison, the specific ohmic losses are analyzed. This magnitude is calculated as the total losses divided by the mass of the cage. This magnitude includes both the rotor bars and the end rings. As the end rings are the same for each geometry, the only term that changes from one case to the other is the mass of the different designs. The result of the losses of each bar can be observed in figure 4.10. The conclusion obtained from these results is that the shape represents an important factor in the skin effect magnitude.

4.2.5 Geometry characterization

In section 2.4, the application of the different bar designs was analyzed. The selection of a certain design is based on the behavior of the IM during the start-up and the steady state. The starting of the motor has two critical parameters, which are the torque and the currents. The value of the current is important because if it is too high, the insulation of the windings needs to be improved, increasing the difficulty of the design and the costs. Regarding the torque, this magnitude needs to reach a certain value that allows the machine to run with the load attached. For the steady state, the most interesting magnitude is the efficiency, which means having a reduced amount of losses.

Based on the requirements of the machine for the starting and steady state operation, in table 2.3 the conditions in which the different bar geometries are used were established. It must be considered that there are more designs, and depending on the application

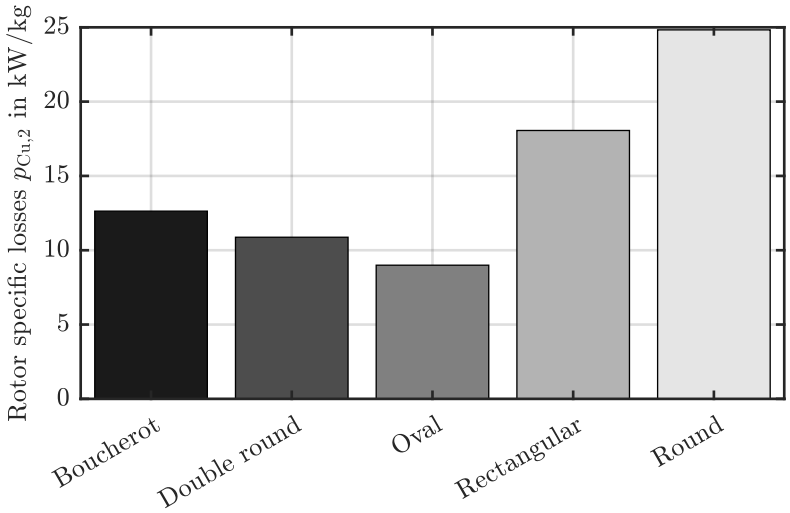

Figure 4.10: Rotor specific cooper losses at $J_1 = 14.5\text{A/mm}^2$ and $f_2 = 30\text{Hz}$.

the chosen one could differ from the table. To validate the information given in table 2.3, a simulation of the different topologies was conducted to analyze the torque and the currents during the start-up. To recreate the starting conditions, each IM design is simulated with a high value of rotor frequency, specifically: $f_2 = 30$ Hz. During start-up, the rotor is at standstill, and therefore, the frequency of the rotor and the stator are the same, according to (4.1). Although in the simulation the frequencies of the rotor and the stator are not identical, by using a high value of the rotor frequency, the conditions are similar to the ones when the machine is starting. The value of the stator current density chosen is $J_1 = 14.5\,\mathrm{A/mm^2}$.

The simulation of five different machine models is done under the described conditions. However, the results of the round topology will not be analyzed as its application is meant for high-speed conditions. By calculating the speed of the machine according to

$$n = (f_1 - f_2) \cdot 60\,, \tag{4.9}$$

the value obtained is $n = 3360$ rpm. In section 2.4, it was mentioned that high-speed application is considered with values around or greater than 10000 rpm. Thus, this is not the case and the study of the bar is not reasonable.

The results of the torque and current from the four different topologies are shown in figures 4.11 and 4.12. Analyzing the values of the torque in the different bars, it can be observed that the one with the lowest value is the oval one. As mentioned in section 2.4, this topology is designed for the steady state and not for the start-up, given its lower starting torque. On the contrary, the bars that showed higher starting torque are the ones with double shapes such as the Boucherot or double round. Regarding the rectangular bar, it was described that depending on the h/a relation, the behavior of the machine was different. Specifically, high ratios lead to high starting torque while the opposite occur with low values of h/a. In this case, the bar presents a ratio bigger than 7.5. Hence, it is expected to have a high starting torque, as shown in figure 4.11.

In figure 4.12 the rotor currents of the machines are presented. The values correspond to the rms value of the 7 rotor bars. These results are also coherent with the theory that was explained in section 2.4 and summarized in table 2.3. As expected, the topologies with high starting torque are the ones with lower currents because the torque depends on the bar resistance. Therefore, if this has a high value, the current will be lower for a constant supply voltage. As a results, the oval bar has the highest starting current. Hence, it is used in applications where the starting current is low.

The results obtained are for a particular bar dimensions. For example, if the size of the outer bar in the case of the Boucherot or the double round bar are changed, the values of the torque and current could be different. However, the importance of this analysis is to provide a simulation example of the theory explained in section 2.4 and confirm the general characteristics of each bar topology.

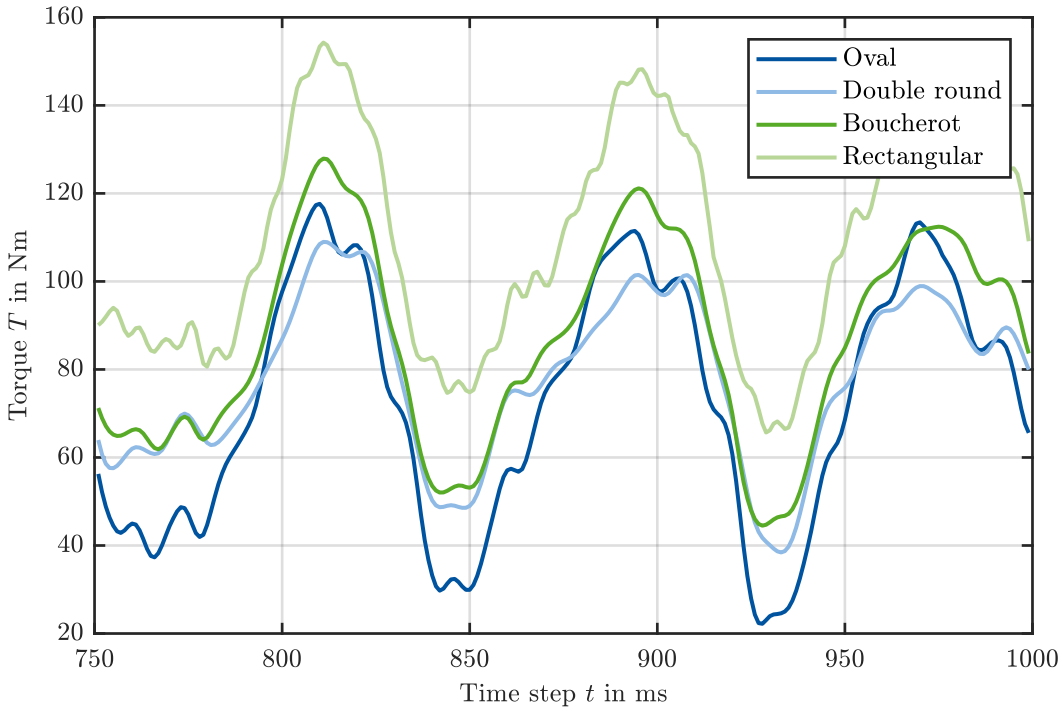

Figure 4.11: Torque comparison in the different machines at $J_1 = 14.5\ \mathrm{A/mm^2}$ and $f_2 = 30\ \mathrm{Hz}$.

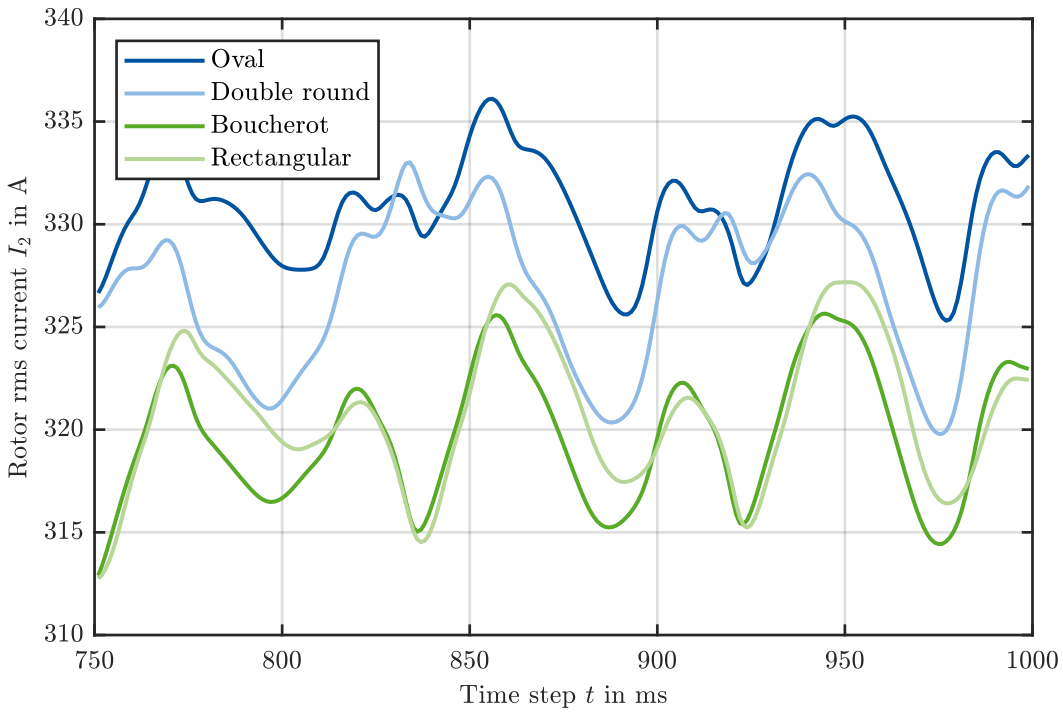

Figure 4.12: Current comparison in the different machines at $J_1 = 14.5\ \mathrm{A/mm^2}$ and $f_2 = 30\ \mathrm{Hz}$.

4.3 Skin effect and machine scaling

The influence of the skin effect in the different magnitudes of the IM has been described along this work. In the case of the rotor bars, the change caused by this phenomenon is an alteration of the value of the resistance and the inductance. As a consequence, the model of the machine is modified. As was explained in section 2.2, in order to perform the scaling of the machine a condition was required: having the same magnetic flux distribution in both models. If the rotor inductance changes, this might have an effect in the flux allocation, thus it is convenient to study the influence of the skin effect in the scaling of the machine.

The scaling procedure that was described in section 2.2 will be used in this section to analyze the changes in the current density distribution. Of the parameters that can be changed in the machine scaling, the one modified in this study is the radial dimension. The reason is that the skin effect only affects the cross section of the rotor bars, where the current density can be appreciated. Other parameters could also be scaled like the axial dimension or the conductivity of the bars. However, the first one does not affect and the influence of the last one has already been determined. Therefore, the procedure analyzed in this section is the radial scaling of the machine.

Several topologies are scaled to study the change in the current density distribution. As an example, the Boucherot and the oval geometries were scaled with a radial factor $k_r = 1.2$, while a more noticeable scaling was performed to the rectangular geometry, with a factor of $k_r = 4$. In figure 4.13, the difference in the shape of the reference rectangular bar shape (light gray) with the geometry of the scaled bar (dark gray) can be observed. The scaling procedure was performed as described in section 2.2, modifying the geometry of the model in the ANSYS © program. Once the designs are done, the next step according to figure 3.3 is to perform the FEA. There are two possibilities for the simulation: scaling the input parameters of the modified model or simulate both machines in the same conditions. The scaling of the parameters consists in modifying the rotor frequency and the stator current density to achieve the same field distribution.

When the radial dimension is modified during the process, there are several scaling factors affected. One of them is k_{R1}, which accounts for the relation between radial and axial scaling. This parameter is calculated with

$$k_{R1} = 1 + \left(\frac{k_r}{k_a} - 1\right) \kappa_2 \,, \tag{4.10}$$

where κ_2 is a geometry parameter that depends on the reference machine and is calculated as

$$\kappa_2 = \frac{1}{\frac{l_{Fe}}{\pi r_{ring}} \frac{A_{ring}}{A_{bar}} Q_2 \sin^2(\pi p/Q_2) + 1} \,. \tag{4.11}$$

In this equation l_{Fe} is the length of the stack, r_{ring} is the ring radius, A_{ring} and A_{bar} are the areas of the cage ring and bar respectively and, finally, Q_2 is the number of rotor teeth. With $\mathrm{k_{R1}}$ and $\mathrm{k_{R2}}$ is possible to calculate $\mathrm{k_R}$ as

$$\mathrm{k_R} = \mathrm{k_{R1}} \mathrm{k_{R2}} \frac{\mathrm{k_a}}{\mathrm{k_r^2}} \,. \tag{4.12}$$

Factor $\mathrm{k_{R2}}$ accounts for changes in the conductivity as a consequence of a material or temperature change, as in this case none of them is varied, this term is 1. Finally, the factor that considers time variations is calculated from $\mathrm{k_R}$ as

$$\mathrm{k_t} = \frac{\mathrm{k_a}}{\mathrm{k_R}} \,. \tag{4.13}$$

This factor is the one that scales the time of the simulation, affecting the input frequency of the scaled machine, which is calculated as

$$f_{2,\mathrm{scaled}} = \frac{f_{2,\mathrm{reference}}}{\mathrm{k_t}} \,. \tag{4.14}$$

Lastly, the input stator current density is also modified with the scaling factor, as can be seen in

$$\hat{J}_{1,\mathrm{scaled}} = \frac{\hat{J}_{1,\mathrm{reference}}}{\mathrm{k_r}} \,. \tag{4.15}$$

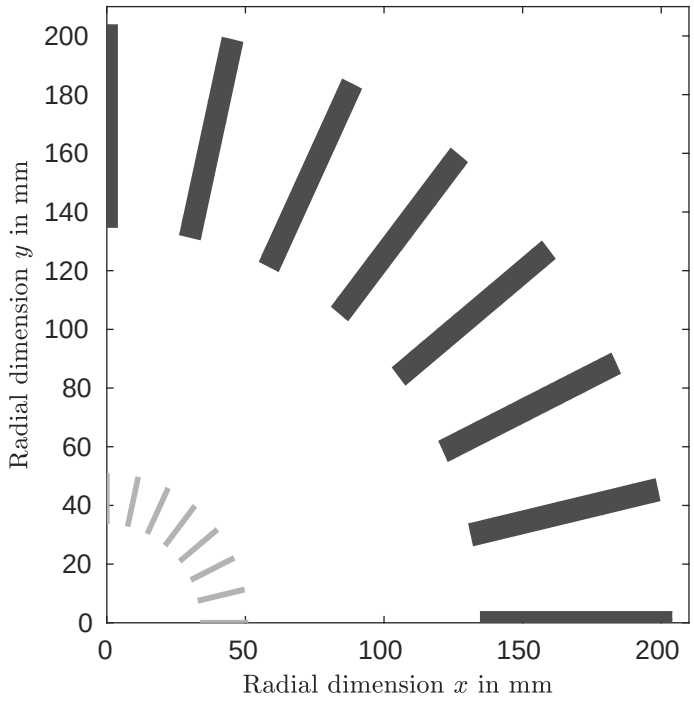

Figure 4.13: Shape comparison of the reference and scaled rectangular bar.

As explained in section 2.2, the requisite for the scaling procedure is that both compared machines have the same field distribution. Thus, by comparing the error of this parameter in both cases, it is possible to have an insight of the order of magnitude of the errors in the scaling. There are two possible comparisons, the field difference between the reference and the scaled model with modified input parameters and the reference with the scaled machine with same inputs. In figure 4.14, the flux density error between the original machine and the one with modified input is plotted. The error is very small and therefore it can be assumed that the flux in the machine is the same. This enables using the scaling procedure according to the theory.

The comparison of the scaling procedure is possible because this transformation is applied not only to the machine geometry, but also to the mesh. Hence, it is possible to compare two machines with different sizes because the size relation between them is also respected in the meshes. Dividing the parameters of the bigger machine by the scaling factor, the model is left with the same size as the reference one.

Comparing the two models with same input parameters, the results are the ones shown in figure 4.15. In these conditions, the errors are much bigger, and therefore, the scaling procedure is not as accurate. Nevertheless, this simulation allows analyzing the influence of the size in the skin effect, as it was one of the magnitudes enumerated in section 2.3 that influence the phenomenon. Since it is the only parameter changed.

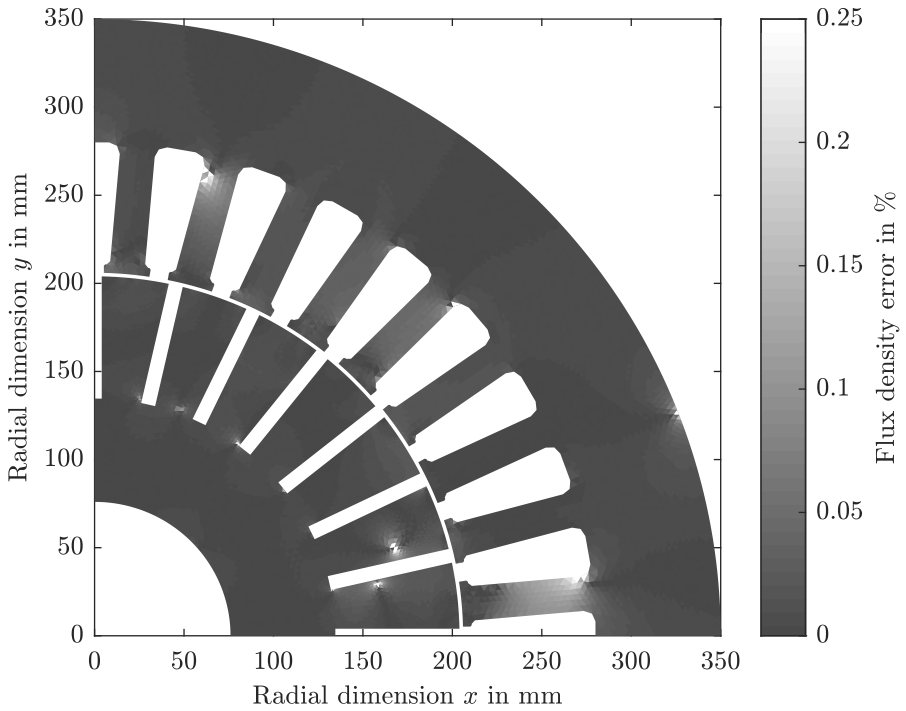

Figure 4.14: Flux density error between the reference and the scaled machine with modified input parameters.

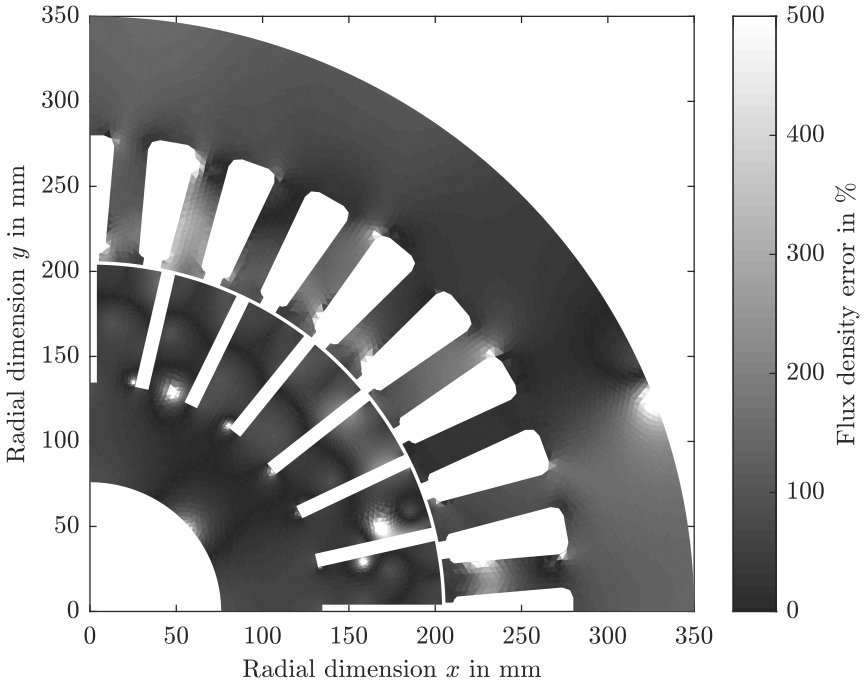

Figure 4.15: Flux density error between the reference and the scaled machine with non-modified input parameters.

After comparing the flux errors, to analyze the influence of the scaling in the skin effect, the current distributions are compared. Thus, it is possible to determine if the skin effect has the same influence in both machines. The procedure of the comparison is similar to the one used to determine the flux errors. As both meshes are scaled with the machine and the elements have the same distribution, it is possible to compare both geometries with different sizes by making use of the scaling factors. In this case, not only the bigger geometry needs to be reduced with k_r, the current density also needs to be scaled according to (4.15). The errors between the current densities in the reference and the scaled machine with modified input parameters are observed in figure 4.16. For the simulation of the scaled machine the input parameters were: $J_1 = 3.625\,\mathrm{A/mm^2}$ and $f_2 = 7.7452\,\mathrm{Hz}$. Instead, the reference machine was simulated with $J_1 = 14.5\,\mathrm{A/mm^2}$ and $f_2 = 30\,\mathrm{Hz}$. The errors between the reference machine and the scaled one with the same input parameters are represented in figure 4.17.

Analyzing figures 4.16 and 4.17, it is observed that the error between the reference and the scaled machine when the input parameters are modified is practically negligible. Therefore, the current distribution in the bars of both machines can be consider identical. However, if the input parameters are not scaled, the errors in the current density distribution are excessive, showing that skin effect is not even comparable in both machines. To prove that the results shown are independent of the bar topology, in figure 4.18 the errors between the reference and the scaled model with modified input are shown. In this case, the errors are also negligible.

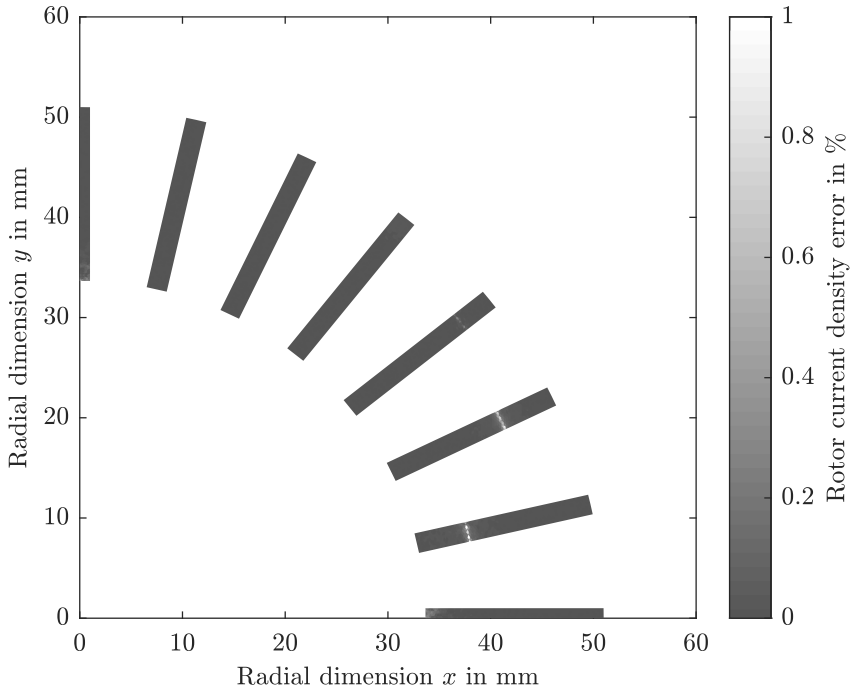

Figure 4.16: Current density error between the reference and the scaled machine with modified input parameters for the rectangular shape.

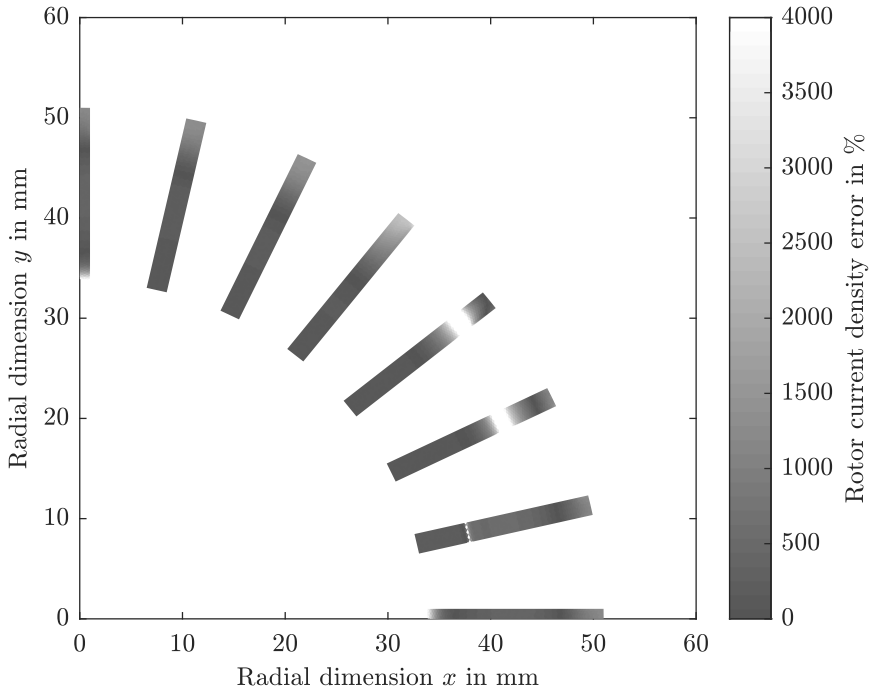

Figure 4.17: Current density error between the reference and the scaled machine with non-modified input parameters for the rectangular shape.

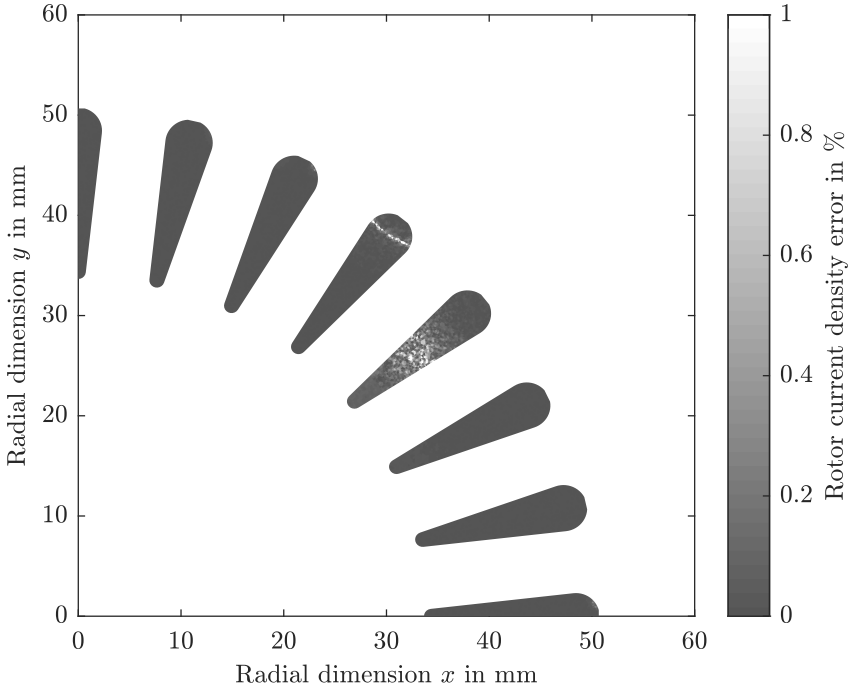

Figure 4.18: Current density error between the reference and the scaled machine with modified input parameters for the oval shape.

4.3.1 Analysis of the skin depth

The fact that different size machines have the same current density distribution arises a doubt related to the skin depth. This parameter determines the influence of the skin effect in the machine and is calculated as the distance between the surface of the bar and the point where the current is reduced by $1/e$. If both machines have the same current distribution but in different dimensions because one is scaled, therefore the skin depth will be different in both machines. However, if two machines are simulated under the same conditions, the skin depth should have exactly the same value as it mainly depends on the frequency and the conductivity. To determine the influence of the skin effect in the different cases, three simulations will be studied: reference machine, scaled one with different input parameters and the case of the scaled machine with same input parameters as the reference.

The analysis of the skin effect is conducted with a particular topology, the rectangular bar shape, since it has an analytical formulation to determine the skin depth as shown in (2.7). Hence, it allows comparing the graphical solutions obtained from the plotted results and the theoretical ones. As the problem requires a graphical solution, it is necessary to analyze the conditions of the simulation. That is said because due to the flux pulsations, the magnetic paths, etc., each bar has a different current density distribution that yields a particular value of the skin depth. Thus, to determine the

bar to analyze, the simulation is at locked-rotor conditions. This means that the frequencies of the stator and the rotor are the same, therefore the mechanical speed is zero according to (4.1). At standstill, the position of all the bars is known and it is possible to detect flux pulsations or other phenomena that would perturb the results. The simulation of the machine under locked-rotor conditions can be observed in figure 4.19. This simulation has been performed not only for the reference one but also for the scaled machine with the two approaches, scaled input parameters and original ones.

Evaluating figure 4.19, it is observed that there are no considerable flux pulsations and all the current distributions are coherent with the results in the literature. The reason for the lack of pulsations is that the magnetic path does not change since the rotor is at standstill. Thus, the inductance formed by the bars and the stator teeth is constant. While in normal operation, as the machine is moving, the magnetic paths changing every time instant. Although there are not visible pulsations in the locked rotor simulation, it can be observed that the current distribution in the bars is completely different from one to another. This depends on many factors like the time instant, the frequencies of the supply, etc. Moreover, it can be seen that some bars

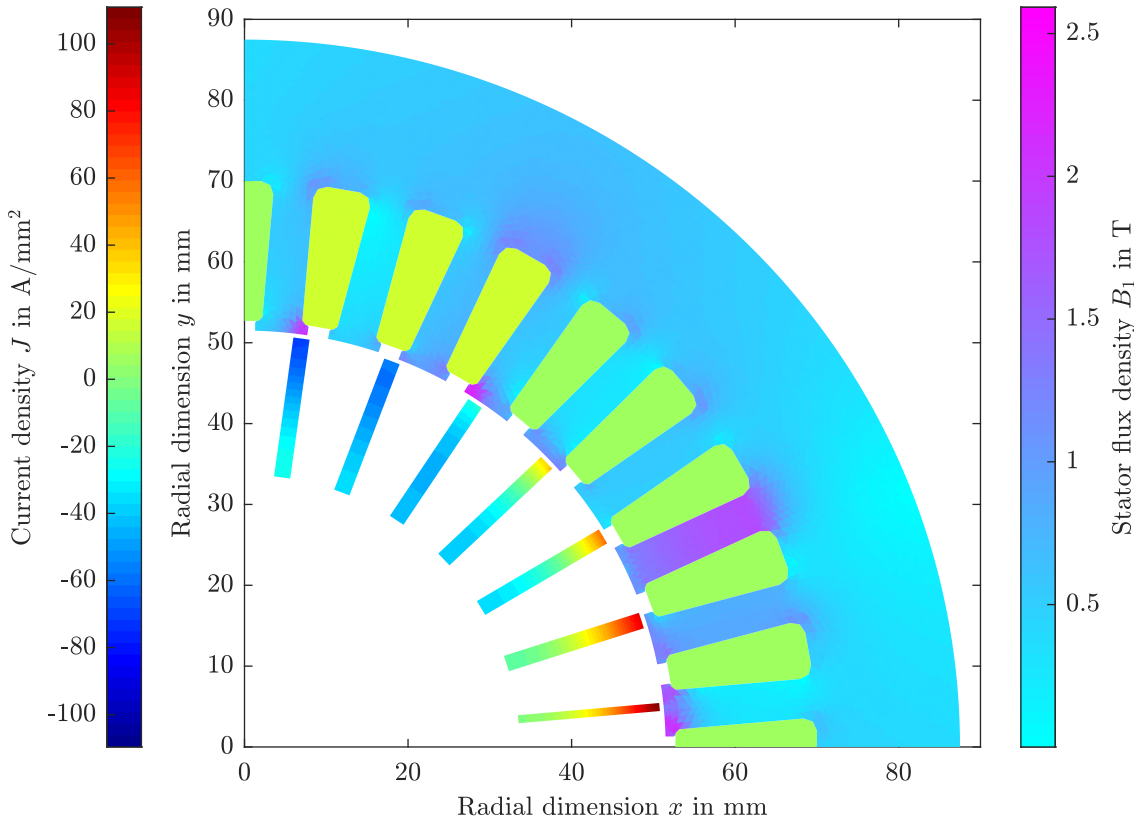

Figure 4.19: Machine simulated at locked rotor conditions.

have a change in the polarity. These bars are not analyzed as the study of the skin effect is done usually in conductors without this phenomenon. Therefore, a bar with a positive current distribution is selected. This bar will be studied to determine the skin depth for the reference machine, the scaled one with modified input parameters and the without modifying the input. The current distributions of the bar in the different cases are shown in figure 4.20.

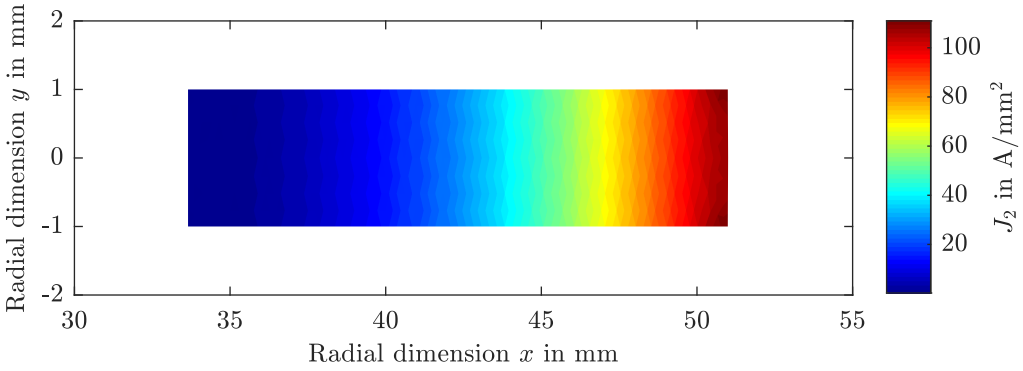

(a) Reference bar.

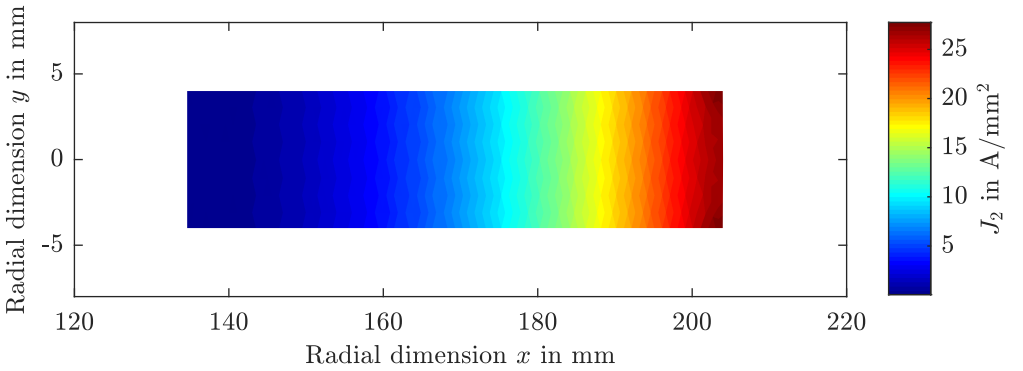

(b) Scaled bar with scaled input parameters.

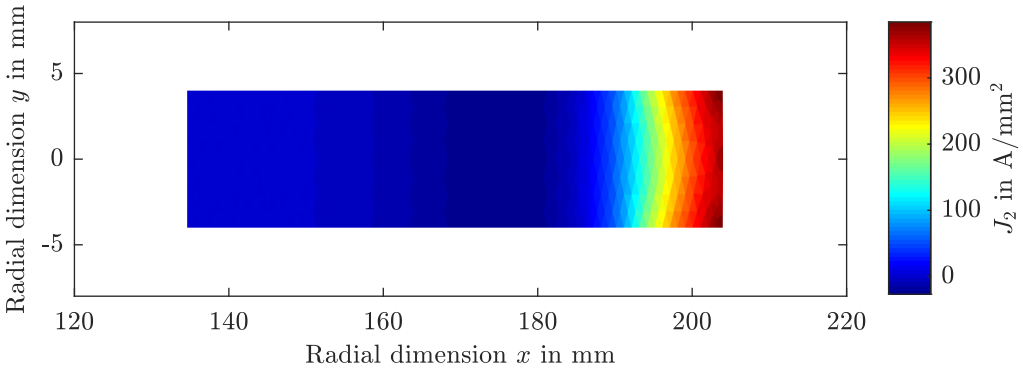

(c) Scaled bar with non-modified input parameters.

Figure 4.20: Rotor current density distribution of the rectangular shape.

From the current distribution it is possible to obtain the skin depth to compare its value in the different cases. This calculation is done using the definition of this parameter given in section 2.3.1. The procedure to obtain this parameter is based on the multilayer approach ([4], [8] and [3]) and consists in dividing the bar into thin rectangles called layers, in which the current density can be considered homogeneous. Hence, the skin depth can be calculated by just measuring the distance and the current variations. The results are shown in figure 4.21, where the plots of the bigger machines have been scaled back to the reference model. Specifically, the radial size has been reduced by the factor k_r in both cases and the current density has been multiplied times k_r in the case of the machine with modified input parameters, as it was the only that had the current density modified.

The results show that the model with modified input parameters and the original machine have the exact same current distribution, if the scaled models are transformed back to the reference. This indicates that skin effect has the same influence in both bars, since they have the same skin depth. Although it could be expected having different skin depths in both machine because of the scaling, the explanation for this result is that the frequency and conductivity in both cases is not the same, which are the parameters that influence the skin depth. To keep the flux constant in the machine, the frequency and the stator current density are scaled using (4.14) and (4.15) respectively. Thus, the scaled machine with modified input parameters is simulated in different conditions, which is what makes the skin depth to have a distinct value. Analyzing the scaled machine model with original input parameters, the skin depth has a different value than the reference model. In this case, the input parameters of

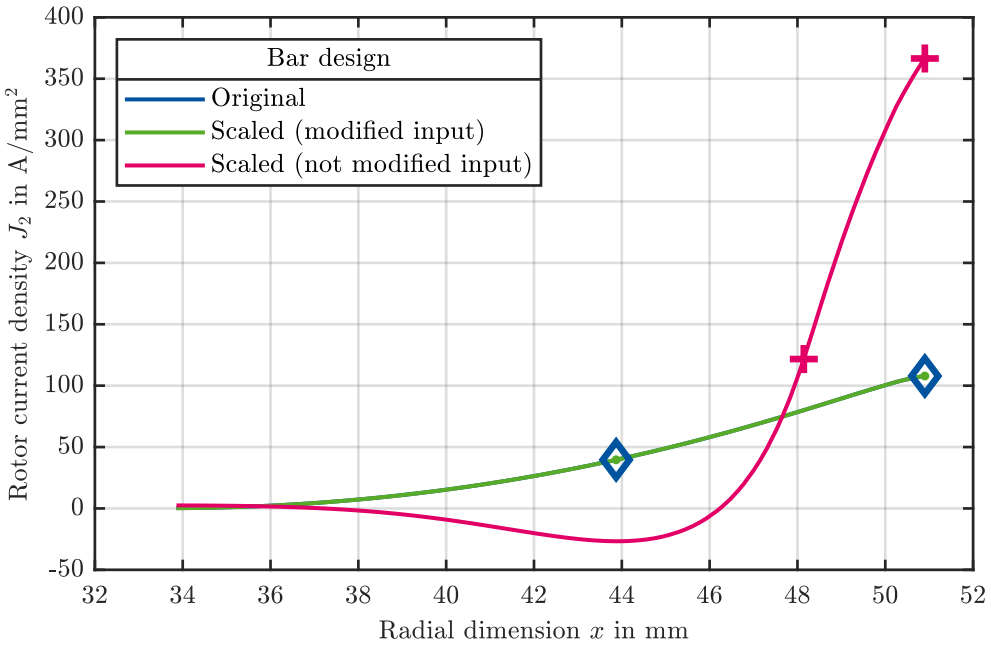

Figure 4.21: Current density distribution and skin depth.

both simulations are the same. However, as the size changes, the current distribution is not the same and therefore the skin depth has a different value, showing that the influence of the skin effect is not the same.

Nevertheless, analyzing only one bar among all the simulated ones and at a certain time instant could induce errors if the skin depth is calculated graphically. Thus, based on the equation that allows to calculate the skin depth in a rectangular conductor, the same conclusion is obtained mathematically: the scaling procedure is not affected by the skin effect when the input parameters are modified. This demonstration is based on the scaling of the input parameters shown in (4.14) and (4.15). If the parameter k_{R1} calculated in (4.10) is substituted into the formulation of k_R in (4.12) and particularized for this case ($k_a = 1$), the result obtained is

$$k_R = \left(1 + (k_r - 1)\,\kappa_2\right) \frac{1}{k_r^2}\,. \tag{4.16}$$

Substituting this equation into the calculation of k_t in (4.13) and the result into (4.14) yields

$$f_{2,\text{scaled}} = f_{2,\text{ref}} \cdot \frac{(1 + k_r - 1)\,\kappa_2}{k_r^2}\,. \tag{4.17}$$

The other parameter, which appears in the skin depth calculation that is affected by the scaling, is the conductivity. Its change with the scaling is defined by

$$\sigma_{2,\text{scaled}} = \frac{\sigma_{2,\text{ref}}}{k_{R1}\,k_{R2}} = \frac{\sigma_{2,\text{ref}}}{\left(1 + (k_r - 1)\,\kappa_2\right)}\,. \tag{4.18}$$

By substituting the frequency and the conductivity formulations into the skin depth equation, the result obtained is

$$\delta_{\text{scaled}} = \sqrt{\frac{1}{\pi f_{\text{scaled}}\,\mu\,\sigma_{\text{scaled}}}} = \sqrt{\frac{1}{\pi f_{\text{ref}} \cdot \frac{(1+k_r-1)\kappa_2}{k_r^2}\,\mu\,\frac{\sigma_{2,\text{ref}}}{\left(1+(k_r-1)\kappa_2\right)}}}\,. \tag{4.19}$$

Simplifying this equation, the result is

$$\delta_{\text{scaled}} = \sqrt{\frac{k_r^2}{\pi f_{\text{ref}}\,\mu\,\sigma_{2,\text{ref}}}} = \delta_{\text{ref}} \cdot k_r\,. \tag{4.20}$$

These results show that when scaling a machine, the influence of the skin effect in the reference and the scaled model is the same, as the parameter that characterizes this phenomenon in the rectangular bar is the skin depth. As shown in (4.20), the skin depth changes according to the scaling. Thus, when the scaled machine is converted back to the reference with the scaling factors, both cases are identical, as shown in figure 4.21.

As a summary of the chapter, the influence of the skin effect in the scaling procedure has been determined. After explaining the simulation process and the influence of this phenomenon in the IM, the importance of this effect was determined by analyzing the losses in the rotor bars. Two calculation methods have been explained to determine the ohmic losses, one assuming that the bar has an even current density distribution and the other considering that the skin effect leads to a heterogeneous one. The results show that not taking the skin effect into account can lead to errors around 10%, which could also compromise the control of the machine. Moreover, the influence of the shape on the magnitude of the losses, and hence on the skin effect, was determined. Furthermore, the characteristics of the bars described in section 2.4 have been proved in simulations. Finally, the scaling of the machine was performed and the differences in the current density distribution were studied. The results showed that when the scaling is done variating in the input parameters, the flux and the current errors are very small. Furthermore, it was proven both graphically and mathematically that the influence in a reference bar and a scaled one is the same. Thus, it can be concluded that the scaling procedure is not affected by the skin effect.

5 Scaling of the geometry

Along this work, the different techniques to optimize the simulations of the FEM have been studied. The goal is to develop a quick process that allows simulating the machine in a reduced amount of time. Moreover, once the simulation is done, the scaling techniques enable optimizing the design of the drive with no extra simulations. This optimization can be done in several ways. For instance the materials can be optimized, the size, the stator windings and also the design of the rotor bars. Already in chapter 2, the most used rotor shapes and its application were explained. As the choice of the rotor bar shape depends on the expertise of the manufacturer and the purpose of the drive, there is not an established topology. Therefore, it is interesting having a scaling procedure, which allows changing the design of the rotor without performing the FEA again, only making use of analytical calculations.

5.1 Principles of the geometry scaling

The development of a scaling procedure to allow the change of the rotor design is a difficult process. The scaling analyzed so far in this works involves the change of parameters of the machine that are quantified. For example, if the rotor material is substituted with a different one, the conductivities of both materials are known. If the temperature changes, the resistances variations are calculated with analytical equations. Even if the radial or the axial dimensions are modified, the changes of the parameters can be determined. However, the rotor topology is a magnitude that is not quantified, it is not only defined by a parameter. Hence, the change of the rotor bar design is a difficult process to introduce in the scaling procedure.

Although the shape of the rotor bars is not determine by any parameter in particular, some properties depend on it. The magnitude that depends on this shape is the rotor bar resistance. Nevertheless, this magnitude is related with the area instead of the shape. Hence, two bars with different shapes but made of the same material and in the same conditions can have the same resistance if the total area of the conductor is the same. The length of the bars also affects the value of the resistance. However, to optimize the calculations and reduce the computational effort, a 2-D model of the machine is studied. Thus, the value of the length is predefined and it is independent of the rotor bar design.

Considering the variations in the machine due to the modification of the shape of the rotor bar, the basic parameter in which the scaling procedure is based is the rotor resistance. Since the geometry of the rotor is closely related with the shape of the rotor core, the resistance change is not the only one produced in the machine. The rotor core is the ferromagnetic material that carries most of the magnetic field in the rotor. As explained in section 2.2, the scaling procedure is based on the magnetic field distribution. This magnitude must be kept constant during the process in order to use the analytical equations with high accuracy. To analyze the flux variations due to the scaling, simulations of the reference machine and the modified one will be carried out. However, this is meant for validation purposes because the objective is the use of analytical equations to perform such operation.

In order to fulfill the requirements of the scaling procedure, the magnetic field distribution has to be kept constant in both machines. This condition forces the scaling method to be used with geometries that share a similar shape. If the bar designs resemble each other, the rotor core of the reference and the scaled machine will be similar and therefore the flux field distribution would not present big differences. As a result, the minor the change in the rotor bars is, the smaller errors yielded by using the analytical equations. However, not all the topologies of rotor bars are similar. As analyzed in section 2.4, there are 5 main designs meant for different applications and whose shapes differ. Nevertheless, there are cases where small modifications are needed and not the change from one topology to a different one.

To analyze the modification of the rotor bar design, it is convenient to consider the variation of the resistance. This is a magnitude that influences the current allocation, and therefore, has an effect in the field distribution in the machine. To keep the flux constant when the resistance of the rotor changes, the inductances of the equivalent circuit should be modified as shown in figure 2.3. Therefore, the influence of the resistance must appear in the scaling factors that are used to modify the values of the different parameters. Analyzing the factors presented in chapter 4, the value that determines the influence of the scaling in the resistance is k_R. This is calculated in (4.12) and depends on other terms. One is k_{R1}, which accounts for changes in the resistance due to the ratio between the radial and axial scaling. Another is k_{R2}, which considers the changes of the temperature or the material. Both of these terms affect the conductivity of the bars. Since the modification of the rotor bar shape does not have any influence on the conductivity, these terms must be kept constant.

Since the parameters k_{R1} and k_{R2} are not modified and the other term on which depends k_R is the relation of axial to radial scaling ($k_a \backslash k_r^2$), a new parameter needs to be introduced. This will be named k_{R3} and will account for the resistance change caused by the variation of the area. The calculation of this parameter is done with

$$k_{R3} = \frac{R_{2,\text{scaled}}}{R_{2,\text{reference}}} , \tag{5.1}$$

where $R_{2,\text{scaled}}$ is the resistance of the new bar and $R_{2,\text{reference}}$ the one of the original design. This factor has a direct influence in k_R, which now is calculated as

$$k_R = k_{R1}\, k_{R2}\, \frac{k_a}{k_r^2}\, k_{R3}\,. \tag{5.2}$$

Therefore, variations of the shape that lead to a bigger area (smaller resistance), will yield values of k_R greater than one.

As mentioned, the changes of the resistance affect the current allocation in the machine. This requires modifying the values of the inductances in order to keep constant the flux distribution. Hence, the change of the parameter k_R will also show in k_t, which is the time scaling factor that also affects the inductances, the frequency, etc. As a consequence, the calculation of k_t is modified to

$$k_t = \frac{k_a}{k_R} = \frac{k_a}{k_{R1}\, k_{R2}\, \frac{k_a}{k_r^2}\, k_{R3}}\,. \tag{5.3}$$

Ideally, the modification of the inductances as well as the resistances would keep constant the flux distribution in the machine and the scaling procedure would have negligible errors. However, it is difficult to compensate analytically the flux changes due to the shape variation and some inaccuracies will appear.

A consideration must be made regarding the calculation of k_{R3}. As explained, its value depends directly on the change of the resistance from one bar design to the other. Nevertheless, the value of the resistance is not calculated easily as it depends on the skin effect. Since the scaling must be performed in the entire $J_1 - f_2$ map, different frequencies and stator current densities will be simulated. Then, considering that the rotor bars are affected by the skin effect, the resistance value is not constant in the map. Furthermore, because of having two different shapes, the resistance variation along the map is not the same in both cases. This implies having a different resistances for each frequency and a particular k_{R3} value in each operating point. Thus, the influence of the skin effect in the different shapes needs to be considered.

Finally, to analyze the theory, real simulations will be carried out to determine the errors and the feasibility of the procedure. Thus, two different approaches will be analyzed to study the process. First, a modification of the rotor bar shape will be implemented, more specifically, the introduction of a cooling channel. This modification keeps the shape of the rotor core and only modifies the bar design, ensuring that the change in the flux distribution is smaller. Then, the change of the bar shape will be done to determine the errors when the shapes differ more and the ferromagnetic material is altered.

5.2 Modification of the geometry

Since both rotor bar designs in the scaling procedure need to be similar to keep the flux distribution constant, a slight modification is introduced in the geometry. This modification is a change in the design to improve a certain aspect of the operation. It differs from the change of one shape to another because it is not a big variation and the application of the design is still the same. For example, if the bar was designed for a high speed application, the operation in these conditions will still be possible but the new shape will allow to have a better performance.

The modification done in this case is the implementation of a cooling channel in the rotor bar in order to achieve a better thermal performance. The rotor bar shape in which this conduct is used is the oval shape. The result of the modification is shown in figure 5.1, where the conduct is the element represented in light gray. The rotor slot and the conduct are represented in the same color because both parts have the same properties since they are made of air.

The thermal modeling of an electric machine is key in the design process as the temperature is one of the most critical parameters that determines the motor operation. As stated in [4], any electric machine is thermally constrained. In the case of regular conductors, the thermal conditions determine the size of the conductor and the insulation. This insulation needs to make sure that the temperatures are not higher than the insulation limit, even in the worst machine conditions. This condition occurs with high supply currents. In the particular case of the IM, the design of the conductors is different. Regarding the stator windings, it is possible to take certain measures like modifying the insulation, changing the distribution of the wires or the winding rates. However, the rotor bars are casted in the shaft, inside the rotor core, and this makes the cooling much more difficult.

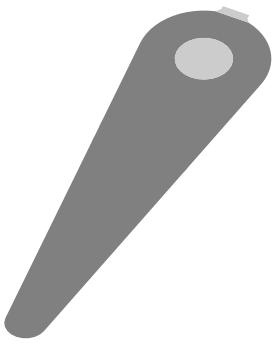

Figure 5.1: Shape of the oval bar with the cooling channel.

To understand the rotor cooling, it is convenient to mention the principle of the heat transfer in the machine. The sources of the heat are the losses that are generated in the windings of the machine, both the rotor and the stator, due to the Joule effect. The higher the losses, the more heat that is generated and therefore the greater the increase of the temperature. It needs to be considered that the losses depend on the operation point and can be affected by the skin effect. As explained in chapter 4, the higher the rotor frequency and the stator current density, the greater the losses in the bar, as shown in figure 4.6. For this reason, it could happen that if the machine is not cooled properly, the temperature rise due to the losses could prevent the machine to work at some points of the $J_1 - f_2$ map.

Regarding the cooling mechanisms, there are two main that take part in the rotor bars of the machine. The first is the conduction of the heat, which is the flow of the heat from one source to a sink, being both of them in contact. The source is the spot with higher temperature, the bars, in the case of the rotor. The heat flows by conduction from this source to the element surrounding these windings, the rotor core. Then, the second mechanism to transfer the heat takes place: the convection. In this case, the heat is transferred from the surface of a solid body to a moving fluid, for example the air. Particularized for the rotor of the IM, the heat is extracted from the surface of the rotor core to the air flowing in the air-gap. There are several types of convection cooling, but the three most important are: natural air cooling, forced air cooling and liquid cooling. The air natural one consists in extracting the heat making use of the normal air flow, which is the case of a totally enclosed design of the IM. The forced cooling involves a fan or a mechanism to move the air and accelerate the heat extraction. If instead of air a fluid such as water or oil is used, the cooling is more efficient but the price of the design is higher. Usually in IMs a fan is attached to the shaft to achieve forced cooling, which removes more heat and drops the temperature.

If the heat created in the rotor of the machine is too big, the forced cooling could not be enough. Therefore, in machines with high power, the cooling with water or oil is used. However this approach is very expensive as it requires pumps, seals, having all materials resistant to corrosion, etc. For these reasons, other options are preferred over the liquid cooling. The one mentioned in [4], is the designing a rotor with additional slots. These could be axial, along the shaft of the machine, or radial if they go from the shaft to the surface of the rotor. These slots enhance the cooling as they facilitate the convection and reduce the path of the conduction, which is the slowest mechanism. In the case studied in this section, the slot in the middle of the bar allows to cool the bar with forced air from the inside, which is where the biggest production of heat takes place. Considering this, the creation of a conduct for cooling is useful in cases where the machines have high rated power and, therefore, high losses. The use of analytical equations allows to simulate the original machine and then study the effect of the air cooling on the electrical and mechanical magnitudes. The change of the thermal model should also be done, but this is beyond the scope of this work.

The main advantage for the scaling of this modification is that the shapes of both rotor bars are very similar and also the flux distribution. Since the modification of the geometry is done in the rotor bars, the magnetic path is not greatly affected because these bars are not made of ferromagnetic materials. Most of the flux in the rotor flows in the core, and if shape is kept, the flux does not vary much. Moreover, the permeability of the rotor bar material is similar to the one of the air, which is the material introduced in the rods. As a result, the magnetic path is barely affected. However, in order to have the same flux is required to scale the machine with the correct factors, not being enough simulating a similar shape.

As explained in section 5.1, the change of the shape of the rotor must be corrected with the factor k_{R3}, which accounts for changes in the resistance. In this case, the quotient to calculate this factor is the resistance of the cooled bar divided by the one of the original oval bar. However, as mentioned before in this chapter, the influence of the skin effect in the bar resistance must be considered in the factor. Therefore, it is convenient to study the resistance variation with the frequency for both topologies. To do so, use is made of the parameter K_R, defined in equation (2.8) and calculated as the quotient of R_{ac} divided by R_{dc}. The first term is the resistance of the bar supplied with a non-zero frequency, while the second is the DC value of the resistance. The calculation of the parameter K_R is not trivial, but use can be made of the formulation proposed in [4] or [8]. The equation to calculate the factor is

$$K_R = \frac{P_{Cu,2,ac}}{P_{Cu,2,dc}}\,, \tag{5.4}$$

where $P_{Cu,2,ac}$ are the rotor ohmic losses when $f_2 \neq 0$ and $P_{Cu,2,dc}$ the losses but for the case of DC current.

As the simulation provides the results for the entire $J_1 - f_2$ map, K_R is calculated for each stator current density by dividing the value of the losses in the operating point by the value at zero frequency. Knowing the factor, the resistance of the bar is obtained just by multiplying it times the value of the DC resistance. Nevertheless, the values of K_R are compared instead of the resistances. The reason is that the value of k_{R3} accounts for the changes of the DC value. Therefore, if the evolution of both bar resistances with the frequency is the same, k_{R3} is fixed for the entire simulation. The results for the case of the oval bar are shown in figure 5.2 while the resistance variation of the bar with the cooling conduct is seen in figure 5.3.

Comparing both figures, the evolution of the resistance is very similar in both cases. Hence, the same k_{R3} is used for each operating point, calculating it as

$$k_{R3} = \frac{R_{2,dc,cooled}}{R_{2,dc,oval}}\,. \tag{5.5}$$

With this value, the rest of scaling parameters such as k_R and k_t are calculated. These factors allow to scale the input parameters before FEA in order to achieve the same flux field distribution.

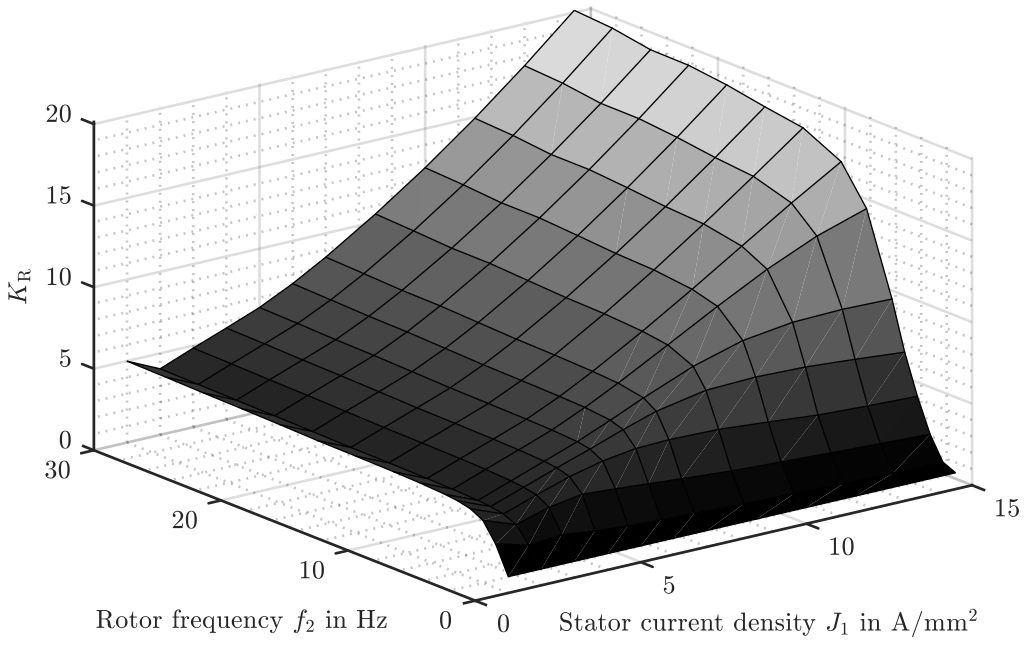

Figure 5.2: K_R parameter of the oval bar shape.

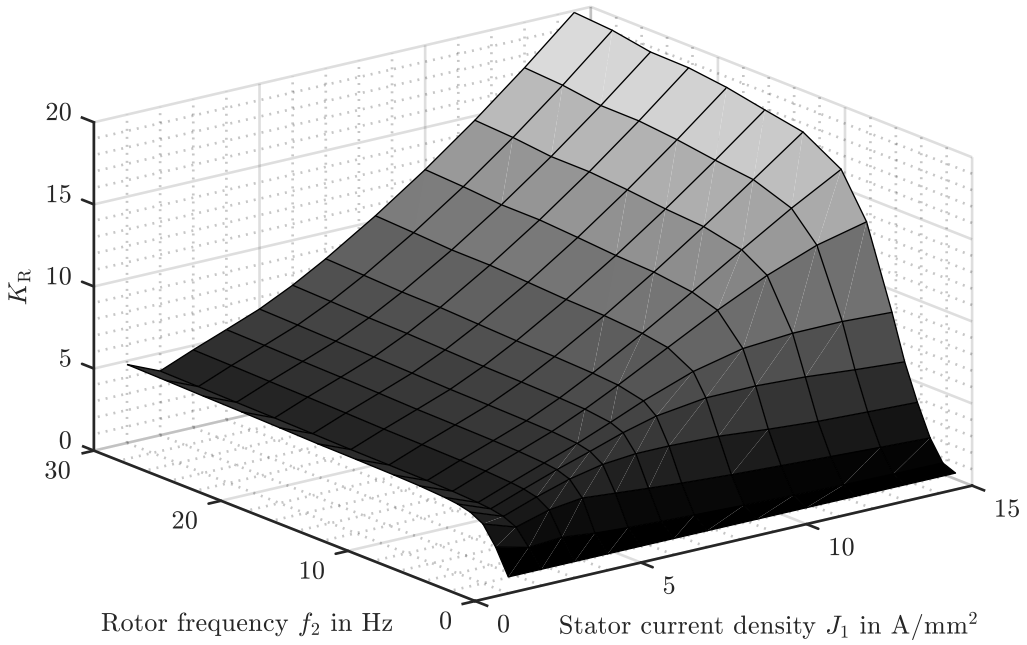

Figure 5.3: K_R parameter of the oval bar shape with the cooling conduct.

After the calculation of the scaling parameters, the FEA is done. In this case, 3 machine models are simulated: the one with oval bars (reference machine), the model with the cooling channel and same input parameters as the reference and the scaled model with modified input. As mentioned in section 2.2, the modification of the input parameters is required to achieve the same field distribution in both machines and reduce the errors of the solution when analytical equations are used.

The process of the scaling is similar to the cases studied in previous chapters but including a few modifications. First of all, as the scaling process implies a change of the geometry, the ANSYS © program is used to create both models. For the geometrical scaling, one model was designed and then scaled. In this case, the entire bar geometry is modified. After the machine with the oval bar and the one with the cooling channel are created, they are simulated using the FEM. For the model with modified input parameters, the scaling of the input is done modifying J_1 and f_2. However, the stator current density is only affected by the radial scaling, which is constant in this case. Thus, the only input parameter affected is the rotor frequency. This is modified with the factor k_t, which depends on the factor k_{R3} determined by the resistance change.

Analyzing the results of the FEA, the flux density distribution between the reference machine and the scaled ones are compared. In figure 5.4, the error of the flux density between the drive with oval bars and the one with cooling channels but with same input parameters is shown for a particular operating point. In this case, it is convenient to study separately the rotor and the stator flux. The reason is that both shapes are not affected in the same way by the scaling procedure. As the geometry of the rotor bar is changed, the magnetic path is not the same even though the materials that are modified have much lower permeability compared with the rotor core. However, this is enough to yield high errors when comparing the flux density between the reference and the scale model, as shown in the figure. Studying the case of the stator, the effect of the geometry change in its magnetic path is not that noticeable. Hence, the errors observed in the stator are much smaller that the ones in the rotor, since the geometry of this part is the same. Nevertheless, the errors have an average value of 5.5%, which is much higher than the errors of the geometrical scaling.

In order to reduce the errors in the flux distribution, the input parameters are modified. When the rotor frequency is modified with the scaling factors, the errors between the reference model and the scaled one for a particular case are the ones shown in figure 5.5. Comparing these results with the ones in figure 5.4, the errors in the rotor can be considered of a similar magnitude. This is due to the change of the rotor geometry, which alters the magnetic path. However, if the errors in the stator are analyzed, it can be appreciated that the average error is much lower. By changing the input parameters, the average error in the stator flux has now a value smaller than 0.7%. It must be considered that these flux errors have been analyze for a particular operating point. However, although the results might change depending on the conditions, the conclusion of having more precision when scaling the input parameters is still applicable, as well as the order of magnitude of the errors.

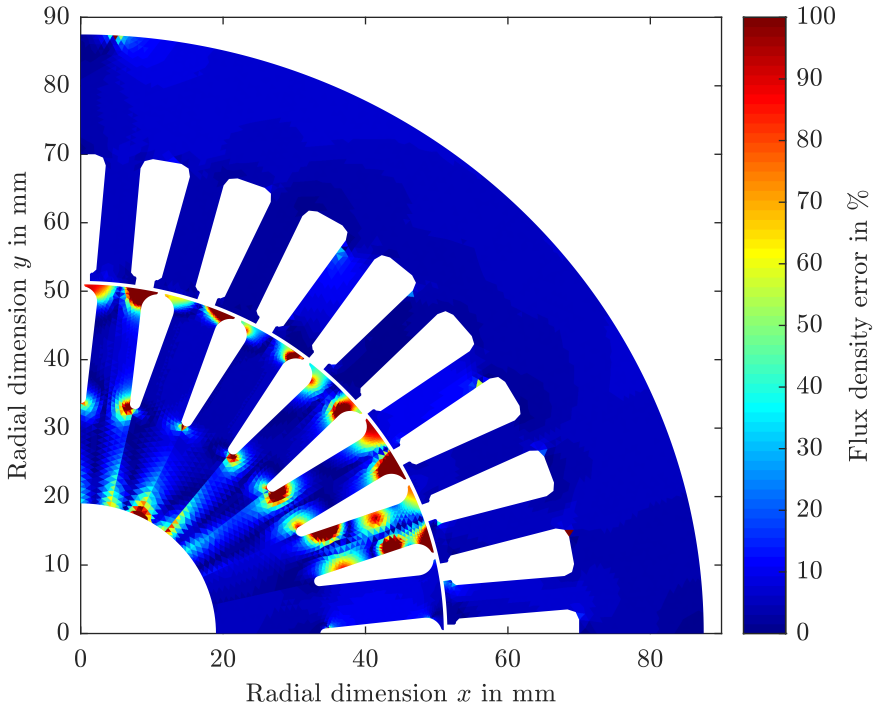

Figure 5.4: Flux density error between the machine with oval bars and the one with cooling channel without modifying input parameters at $\hat{J}_1 = 6\,\mathrm{A/mm^2}$ and $f_2 = 5\,\mathrm{Hz}$.

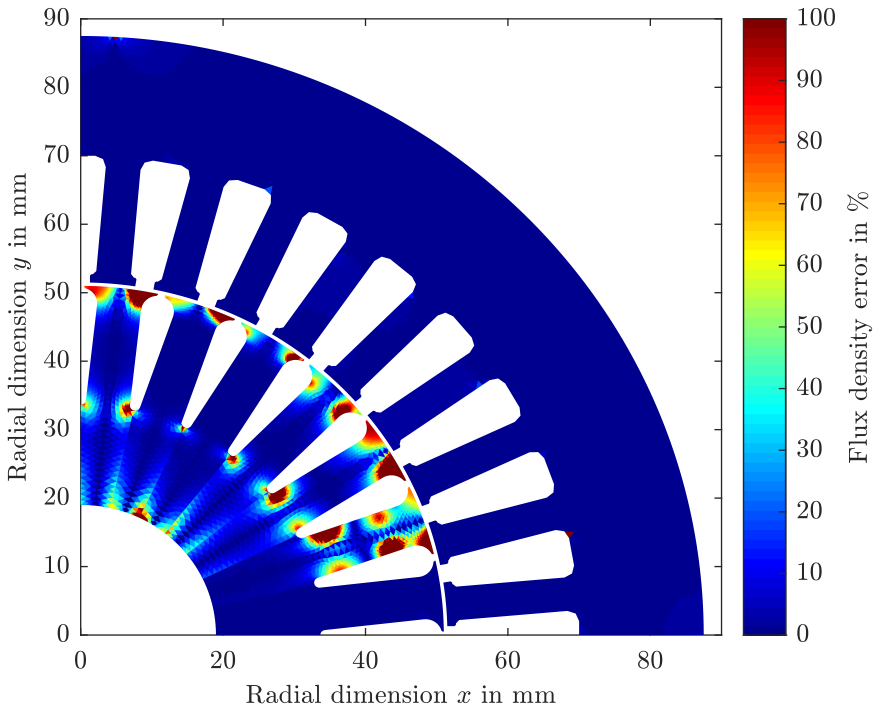

Figure 5.5: Flux density error between the machine with oval bars and the one with cooling channel and modified input parameters at $\hat{J}_{1,\mathrm{ref}} = 6\,\mathrm{A/mm^2}$ and $f_{2,\mathrm{ref}} = 5\,\mathrm{Hz}$.

The results of the simulations show that scaling the input parameters reduces the flux errors but mostly in the stator. The rotor case is different because the modification of the geometry alters the reluctance of the rotor and changes the magnetic paths. For this reason, the errors that appear in the rotor are much higher than the ones in the stator, which keeps the geometry constant. Considering that to use analytical equations to scale the machine, the flux distribution in both machines must be similar. The feasibility of this approach is questionable. In the case of the geometrical scaling, it was shown that when the flux distribution in both machines was the same, the errors were negligible. However, when the input parameters are not scaled, the flux errors are considerable and the use of the analytical equations shows inaccuracies.

To determine the errors of using analytical equations to do the scaling, the errors in the magnitudes of the machine such as losses, torque, etc. are studied. To analyze these magnitudes, the scaled machine is converted back to the reference by making use of the analytical equations, which are the ones to change the parameters shown in table 2.1. If the errors in the magnitudes are small, despite the differences in the flux, the use of analytical equations could be accepted.

The results of the scaling using analytical equations are studied. In this case, there are two principal values interesting for the comparison: the torque and the losses. The first one is important because it determines the power generation in the machine, which in most cases is the critical magnitude for the motor operation. The losses are important because they allow, along with the value of the torque, to calculate the machine efficiency. This parameter is key as the current standards establish minimum values for this magnitude in most cases.

In order to compare the magnitudes mentioned, use of the analytical equations is made. The scaled machine with modified input parameters and the one with the same input as the reference are converted to the original machine model. Since the transformation from the reference to the scaled model was making use of the factor k_{R3}, the inverse of this value is utilized for the opposite conversion. When the models are representations of the original machine, their values can be compared. The first magnitude to compare is the torque generated in each operating point of the $J_1 - f_2$ map. In figure 5.6, the error between the torque value of the machine with oval bars and the one with the cooling bars and same input is shown. The figure shows that the inaccuracies in the flux distribution are translated into the magnitudes mentioned, yielding an error that is not negligible. If instead, the error is calculated between the bar which had modified input parameters and the original one, the results are the ones shown in figure 5.7. By scaling the input parameters, the torque error is reduced greatly, having very accurate results. In both cases, there are a set of values which present errors above the 10%. However, these values belong to the lowest stator current density. At these points, the torque generated by the machine has values near to 0 Nm. Since the errors are calculated in percentage, even though the deviations in the values are small, the errors are big because they are divided by a number close to zero.

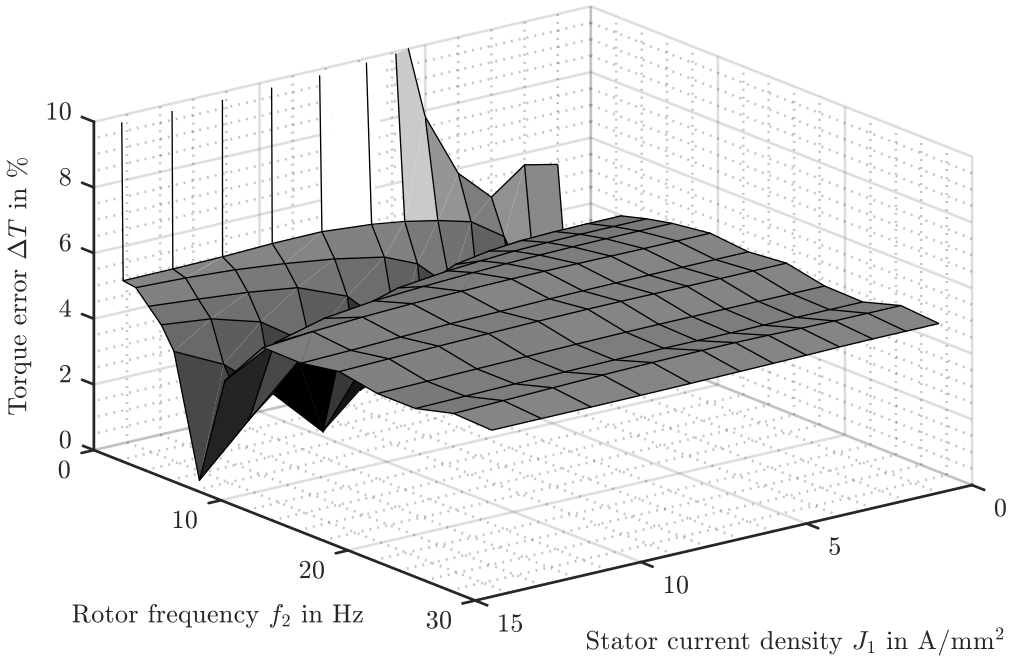

Figure 5.6: Torque error between the machine with oval bars and the one with cooling channel without modifying input parameters.

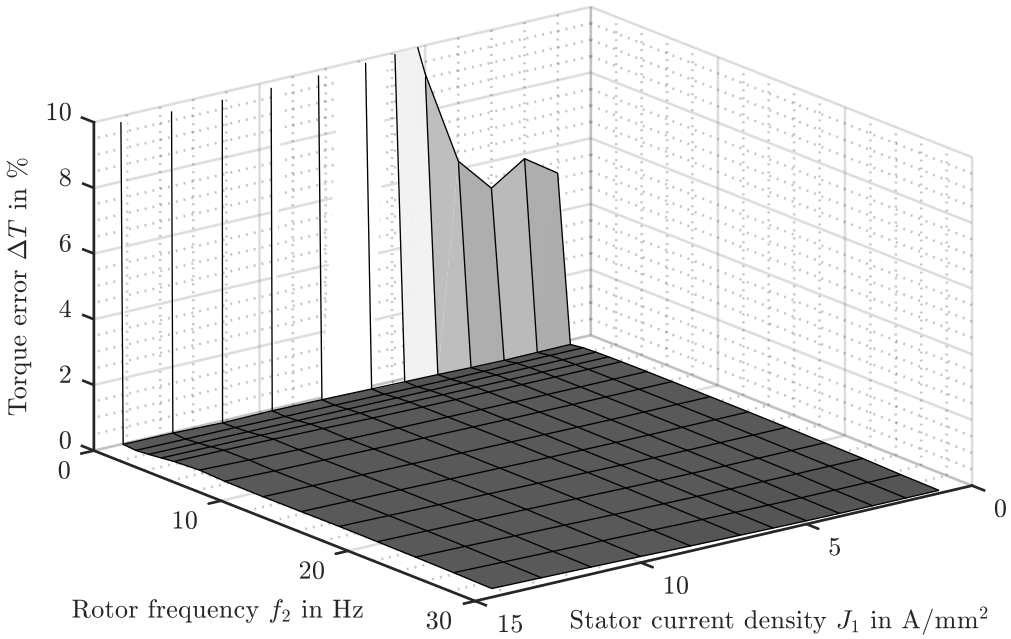

Figure 5.7: Torque error between the machine with oval bars and the one with cooling channel and modified input parameters.

If the losses that occur in the machine are studied, the results are the ones shown in figure 5.8 for the case of non-scaled input parameters and in figure 5.9 when the inputs are scaled with the corresponding factors. Even though the errors in the case of non-scaling the input are small in most of the points, under some conditions they reach values of 5%, which could not be acceptable in all cases. However, if the input parameters are scaled, the errors are always under 1.5%. The losses of the figures are the combination of the stator and rotor ohmic losses as well as the iron losses. As the stator of the machine is kept constant, the losses in this element present almost no errors. Thus, when adding all the losses, the errors of the rotor losses have less influence.

Analyzing the errors derived of the scaling procedure, it can be concluded that although the flux distribution is not the same in the reference and the scaled model of the machine, the errors yielded in the losses and torque comparison could be acceptable. However, this is only in the case of scaled input parameters, which demonstrates that is the use of the resistance correction factor in the scaling what allows this procedure. As a result, it can be stated that the use of analytical equations to perform the scaling of the machine to study modifications of the rotor bar design is possible and yields results with errors below 2% in most of the magnitudes.

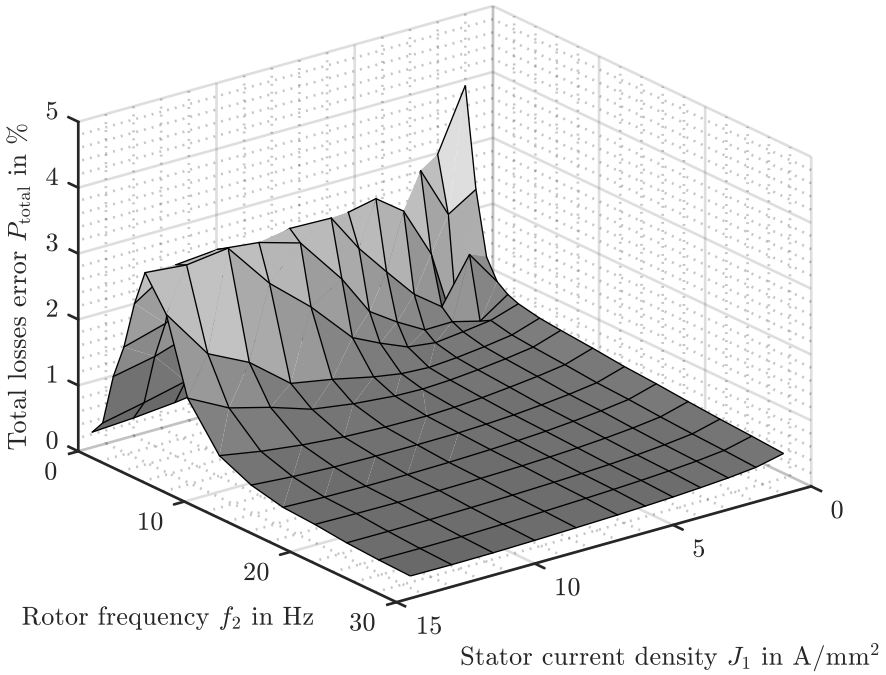

Figure 5.8: Total losses error between the machine with oval bars and the one with cooling channel without modifying input parameters.

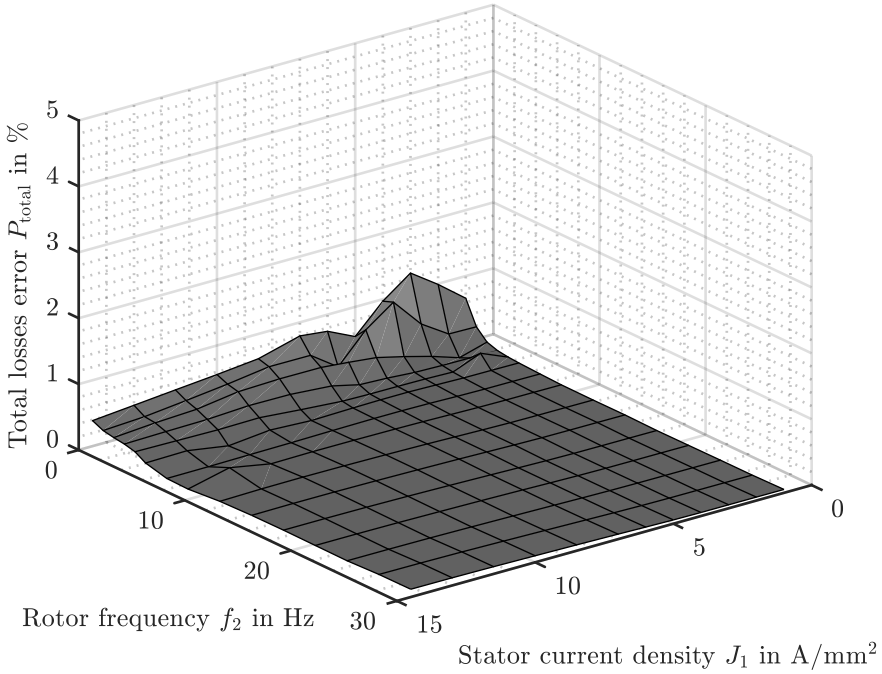

Figure 5.9: Total losses error between the machine with oval bars and the one with cooling channel and modified input parameters.

5.3 Change of the design

In the last section, it was proved that a slight modification of the geometry of the rotor bar yields small errors. In this section, the effect of changing the rotor bar shape is analyzed. The condition that enabled a small variation in the geometry, like the introduction of a cooling channel in the rotor bar, without having considerable errors, was the fact that the shape of the bar remained similar. However, it is interesting to determine the effect of a more demanding scaling, like the change of the rotor bar topology. In this case the modifications have a bigger dimension, and therefore, it must be determine if the errors in the results could be acceptable.

As mentioned in previous chapters, the use of analytical equations to scale the machine is accurate when the flux density distribution in both models is similar. With the changes of the geometry in the machine, the magnetics paths are modified. This was observed in section 5.2, where the original machine and the altered design did not have the same flux distribution. With the introduction of the cooling channel, the modifications only affected the rotor bars and not the ferromagnetic materials. Still, the differences in the rotor flux distributions of the machines were remarkable. Nevertheless, despite these errors, the final results presented accurate values in terms of losses and torque generation.

A more complex scaling process is the change of the entire rotor bar design, altering not only the rod itself but the materials that surround it. More specifically, this change would be substituting a geometry of the ones shown in figures 2.9 and 2.10 for a different one. In this case, the bigger the differences between the two topologies are, the higher the errors of using analytical equations. Thus, the modification of the rotor design must be made with two similar topologies. As a result, the scaling will be applied to alter the oval topology to the Boucherot bar shape. There are two main reasons for this selection: the similarities in the shape and the interest from the operation point of view.

The similar design of both bars can be observed in figure 5.10. These are the geometries that share most similarities in the shape among the ones mentioned in section 2.4. This characteristic ensures that the flux distribution in both IMs will be more similar than in the rest of the cases. Despite the similarities, errors are expected as the variation of the bar design implies changes in the ferromagnetic materials, specially in the rotor core. The consequence of this modification is having different magnetic paths that will induce errors when the analytical equations are used. However, using the scaling factors as in section 5.2, these errors are expected to be reduced in the output values of the simulation, i.e. the losses and the torque generation. It must be mentioned that there are innumerable shapes for the rotor bar and not only the five mentioned in section 2.4, as each rod design can be optimize with a particular machine application. Hence, the scaling could be done between more similar designs than the selected ones. However, the feasibility of using analytical equations must be proven in a complex case.

Not only the similarities in the designs make this analysis interesting, but also the real application. In section 2.4, the use of different bar designs was described. It was concluded that the oval design was meant for low to medium power IM and applications where the starting current did not have a high peak value. On the contrary, the main application for the Boucherot shape is in high power machines

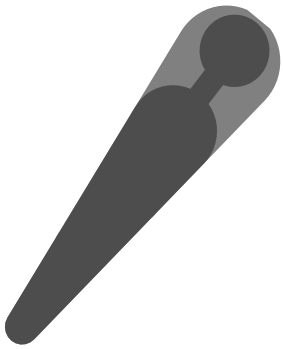

Figure 5.10: Comparison of the oval and the Boucherot bar designs.

where the starting current has a high value, as the design enhances the skin effect and increases the resistance during start-up. Therefore, this scaling procedure to change the bar topology can be useful in a design stage. If a FEA of the simple bar is done, and the results obtained show that the starting current exceeds the limits, analytical equations can be used to determine if the double shape is a better solution.

To study the feasibility of the scaling procedure, both geometries are simulated. No geometrical scaling must be applied to any design, instead the two IMs must be designed in ANSYS ©. Both machines are simulated with the FEM. The reference selected is the motor with the oval bars, and therefore, the one with the double shape will be considered the scaled. As in section 5.2, one simulation of the scaled model will be done with same input parameters as the reference, and in the other case, modifying them with the scaling factors. In order to scale the input, the factor k_{R3} is calculated as in (5.1) and used to obtain the rest of scaling parameters. Again, the factor only accounts for the difference in the resistance between both bar designs, not considering changes in the magnetic path. However, to calculate the value of k_{R3}, it is convenient to determine the variation of the resistance due to the skin effect.

As the machine is simulated in different operating points, each with a stator current density and a rotor frequency, the influence of the skin effect is different in every case. Due to the uneven current density distribution in the rotor bars, the real resistance of the conductors is different to the DC value. Based on the rotor ohmic losses, the resistance variation can be calculated making use of the factor defined in (5.4). Determining the variation of the real resistance in both cases is needed because the scaling factor k_{R3} would have different values depending on the operating point. The result of the resistance variation in the oval bar design is shown in figure 5.2. The difference between the value of the DC resistance and the real one is shown in figure 5.11 for the case of the Boucherot bar.

In the case of the geometry modification to introduce the cooling channel, the variation of the resistances of both bars was very similar. This characteristic lead to a scaling factor constant for the entire operation map. By comparing the variation in the case of the Boucherot and the oval bar, it is obvious that the variations cannot be neglected. In figure 5.12, the difference between the change of the resistance in both bars is shown. Based on this figure, different k_{R3} must be calculated and this is only possible when a FEA of both machines is conducted. However, the purpose of the scaling is providing the simulation results of both machines by only simulating one. Therefore, it is not possible to calculate particular values of k_{R3} for each operating point based on the simulation of one machine. There are possible approaches to overcome this problem. For example studying a wide variety of machines and obtaining look-up tables to calculate k_{R3}, obtaining analytical calculations to predict the resistance variation of the different shapes, etc. Nevertheless, the solution of this problem is beyond the scope of this work. The easiest approach is scaling the machine with a constant value of k_{R3}, which corresponds to the DC resistance quotient. Although errors are expected by using this simplifications, analyzing their values is interesting.

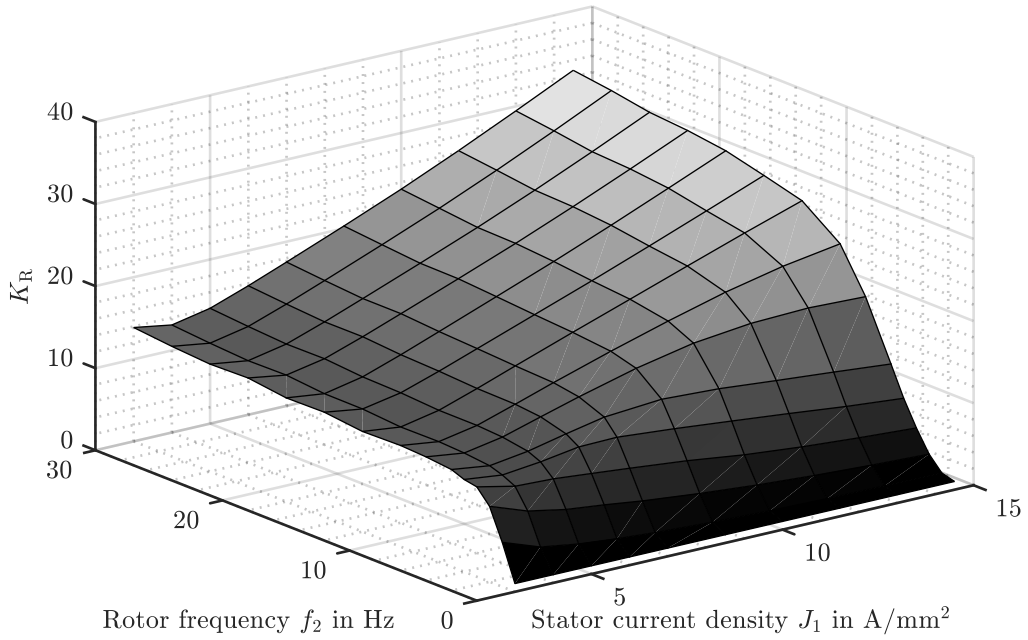

Figure 5.11: K_R parameter of the Boucherot bar shape.

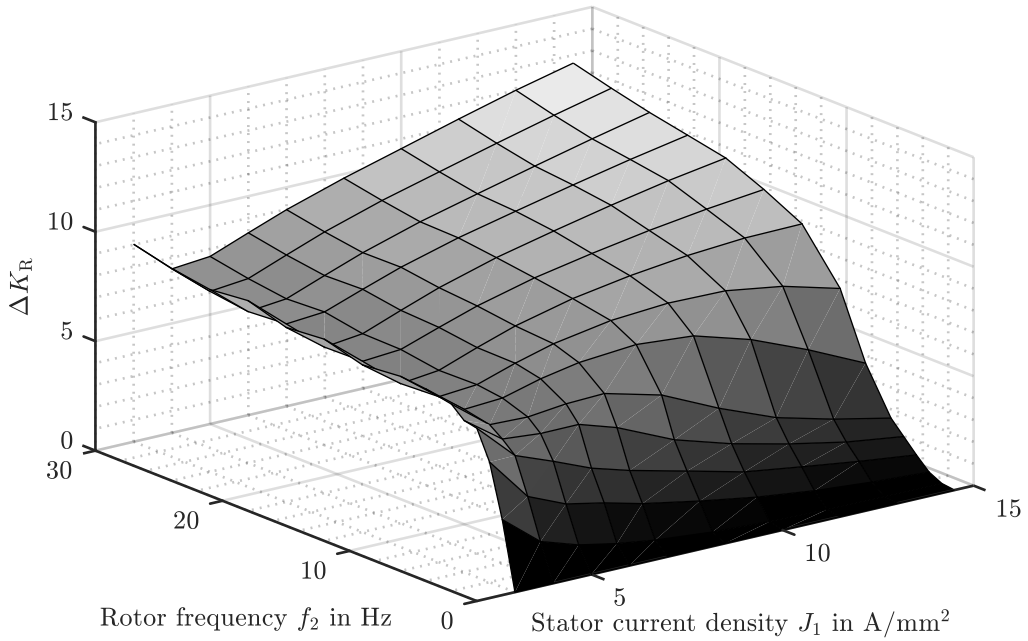

Figure 5.12: K_R difference between the Boucherot and the oval bar shape.

The simulation of the three machine models is done: oval, Boucherot with modified input and Boucherot with same input. These machines are simulated in the entire $J_1 - f_2$ map. In the model with scaled input parameters, the modification of the rotor frequency and the stator current density is done by using the scaling factor k_{R3}. With this parameter, the value of k_t is obtained according to (5.3). As there is no geometrical scaling, the only input parameter modified is the rotor frequency, which is calculated as shown in (4.14).

The flux density distribution of the simulated machines is compared to analyze the differences. The error between the IM with oval rods and the one with Boucherot bars is shown in figure 5.13, both simulated with same inputs. Analyzing the machine with Boucherot bars and scaled input parameters, the results of the flux differences are the ones shown in figure 5.14. The operating point is the same as in the previous figure for the reference machine. The input parameters of the scaled model, since they are modified, are the equivalent to the same point. Instead of analyzing the errors in the entire map, one representative point is chosen. However, the magnitude differences in the machines are calculated in all operating points. In this case, only the flux in the stator of the machines is analyzed. The reason is that the rotors have different geometries that lead to distinct meshes. Hence, it is not possible to compare element by element. However, in section 5.2, the results showed that the main effect of the scaling is reflected in the stator flux and the rotors present almost the same errors.

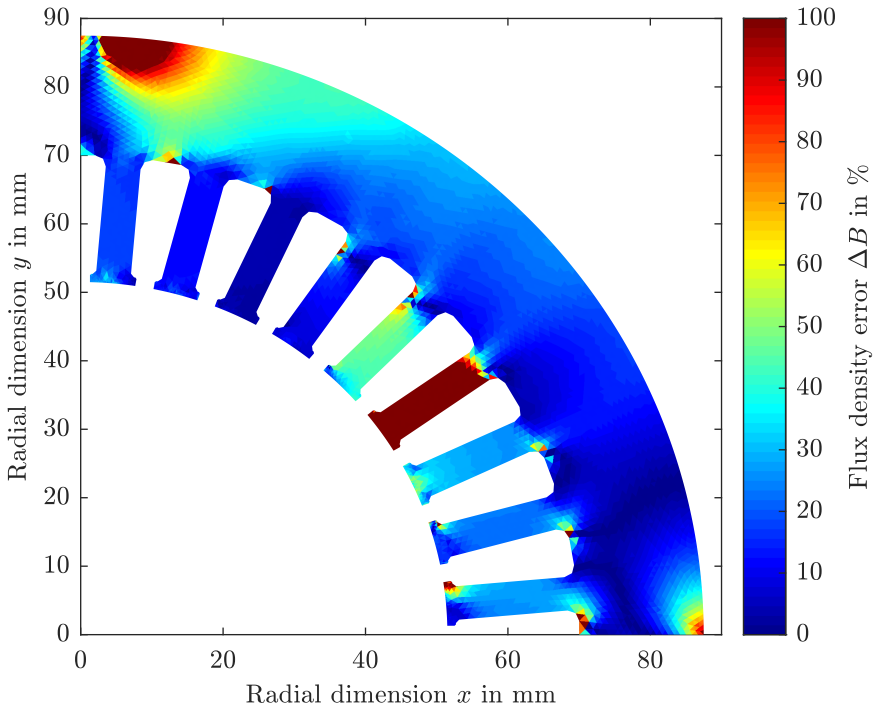

Figure 5.13: Flux density error between the machine with oval bars and the one with Boucherot rods at $\hat{J}_1 = 6\text{A/mm}^2$ and $f_2 = 5\text{Hz}$.

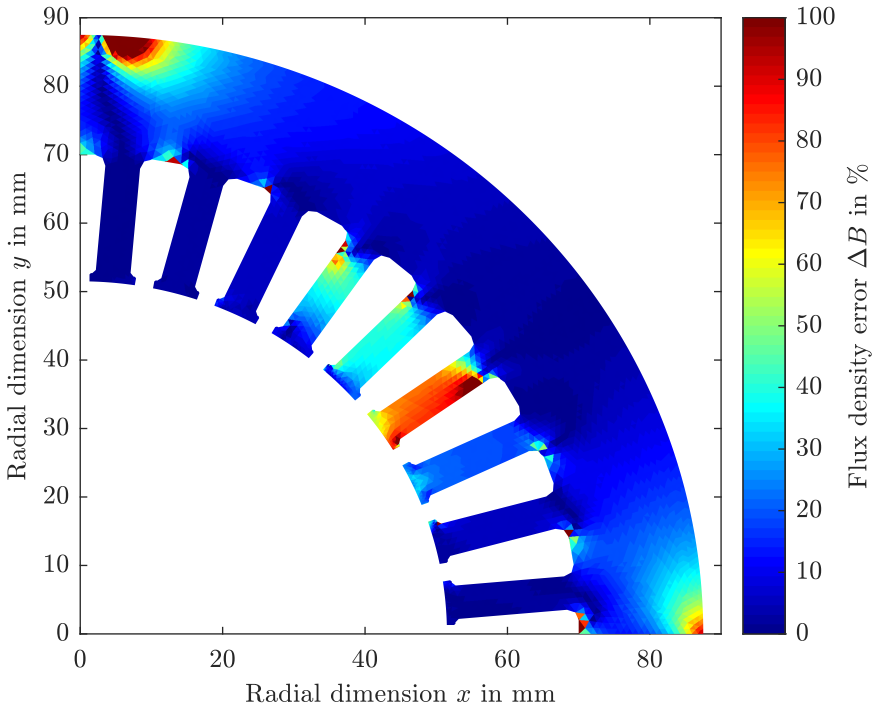

Figure 5.14: Flux density error between the machine with oval bars and the one with Boucherot rods and modified input parameters at $\hat{J}_{1,\mathrm{ref}} = 6\,\mathrm{A/mm^2}$ and $f_{2,\mathrm{ref}} = 5\,\mathrm{Hz}$.

Analyzing the results of the flux density errors, it can be observed that the modification of the input parameters reduces them. The average error in figure 5.13 is around 35% while in figure 5.14 is 19%. The reduction of the error is considerable, but still the magnitude of it is too big compared with the case of the cooling channel. However, the results are coherent because the rotor core is modified, which has a greater influence in the magnetic path and leads to bigger flux errors. Even though the errors in the rotor could not be calculated, they are also expected to be bigger than in the cooling bar case.

To determine the real impact of the flux errors, the differences of the torque and the total losses between the reference machine and the scaled one are analyzed. The torque comparison between the reference machine and the scaled with same input parameters is shown in figure 5.15. The results present errors with values around 20% in the majority of the map. If the input parameters are scaled, the errors are reduced to the ones in the figure 5.16. In this case, the improvement is not as general as in the case of the cooling channel, where almost all the points had an error close to zero. When scaling the input parameters, the points with stator current densities close to zero show higher errors than when the both machines have the same inputs. However, this is not that critical, as for low current values the torque has a small magnitude and therefore the errors are consequence of dividing by a number close to zero. The points that have more relevance are those where $\hat{J}_1$ has higher values because the torque

generation is greater, which is the usual operation point for most IM. For example, analyzing the range with stator current densities grater than $4\,\mathrm{A/mm^2}$, the errors are reduced from a mean value of 15% to a 5% by scaling the input.

The analysis of the electric losses in the machine is performed calculating the errors of the sum of iron and ohmic losses between the reference and the scaled IM. In figure 5.17, the difference between the machine with oval bars and the one with Boucherot rods is shown. Both machines are simulated with the same input parameters. The results present errors that rise up to almost 30%. However, the average value of the error is lower, but still has a value near 5%. When modifying the input parameters with the scaling factors, the errors are reduced to a value close to 1.5%, as shown in figure 5.18.

The results of both the losses and the torque errors demonstrate that the scaling of the machine loses accuracy if the modification of the bar shape is considerable. In the case of the cooling channel, the change affected mainly the magnetic flux in the rotor and the stator kept the same values. As a result, the errors were under 2% in the analyzed magnitudes. However, the change of the rotor topology involves a modification of the rotor core, which affects the magnetic path of both the stator and rotor. This results in bigger differences between the flux of both machines. As the scaling requires same flux distribution in both machines, the errors are translated in the output magnitudes. Still, these have values around 5% in most of the operating map. Thus, the use of analytical equations is possible if the application affords that uncertainty.

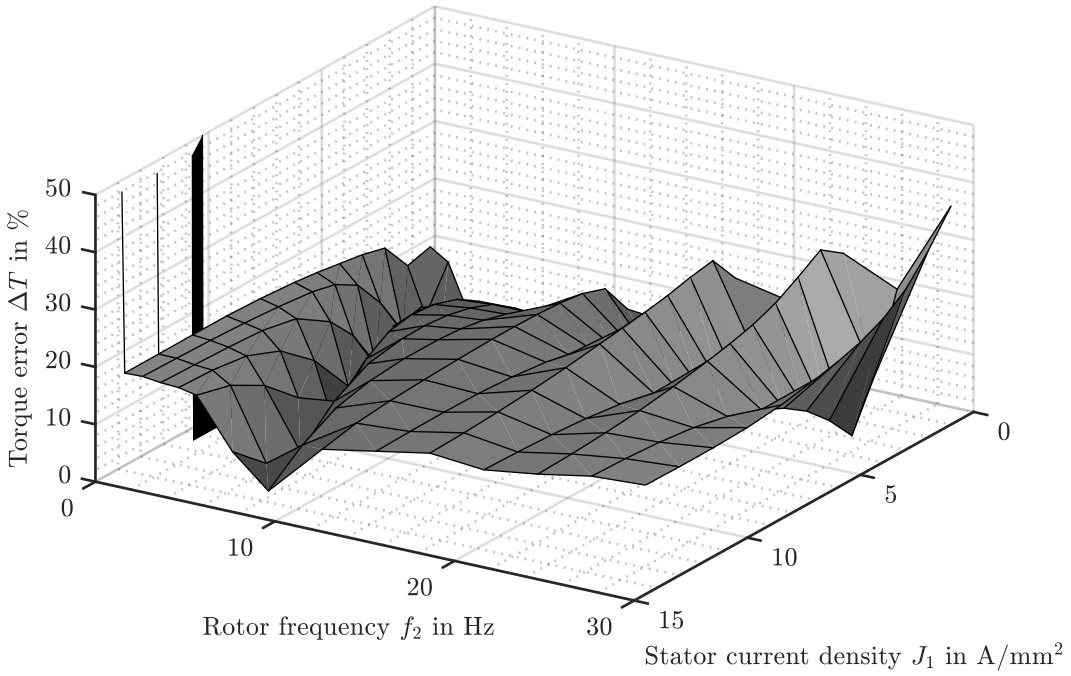

Figure 5.15: Torque error between the machine with oval bars and the one with Boucherot rods without modifying input parameters.

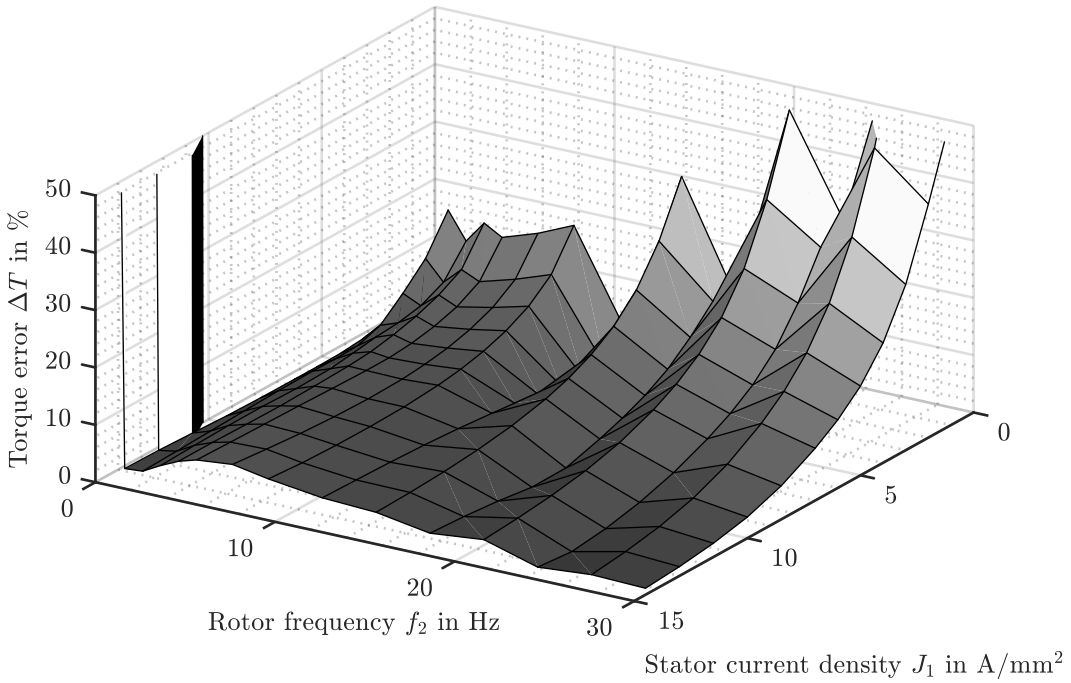

Figure 5.16: Torque error between the machine with oval bars and the one with Boucherot rods and modified input parameters.

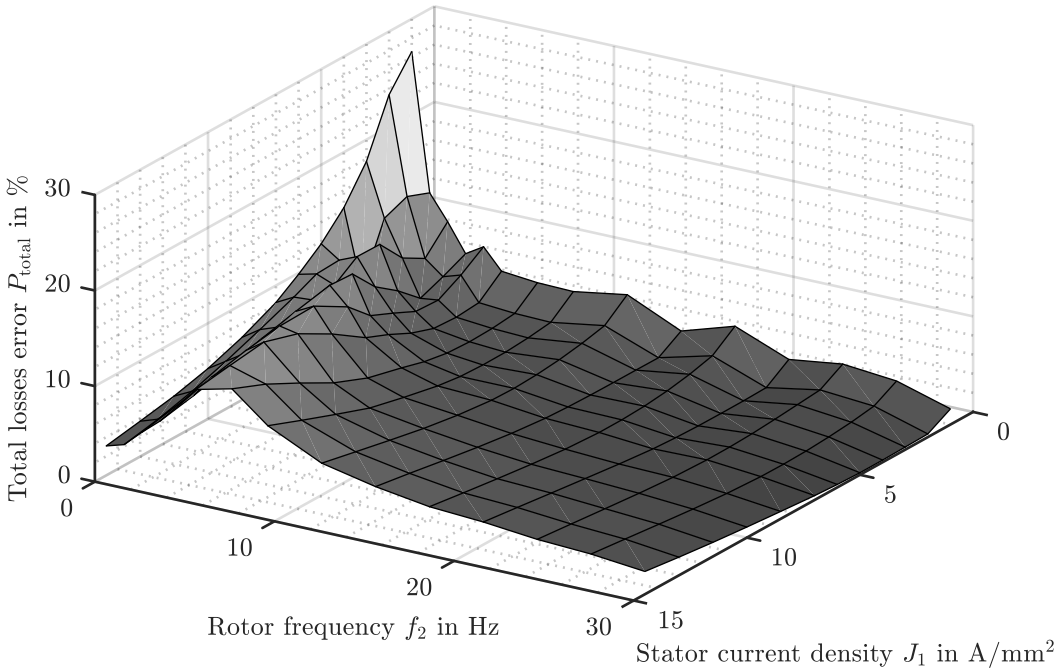

Figure 5.17: Total losses error between the machine with oval bars and the one with Boucherot rods without modifying input parameters.

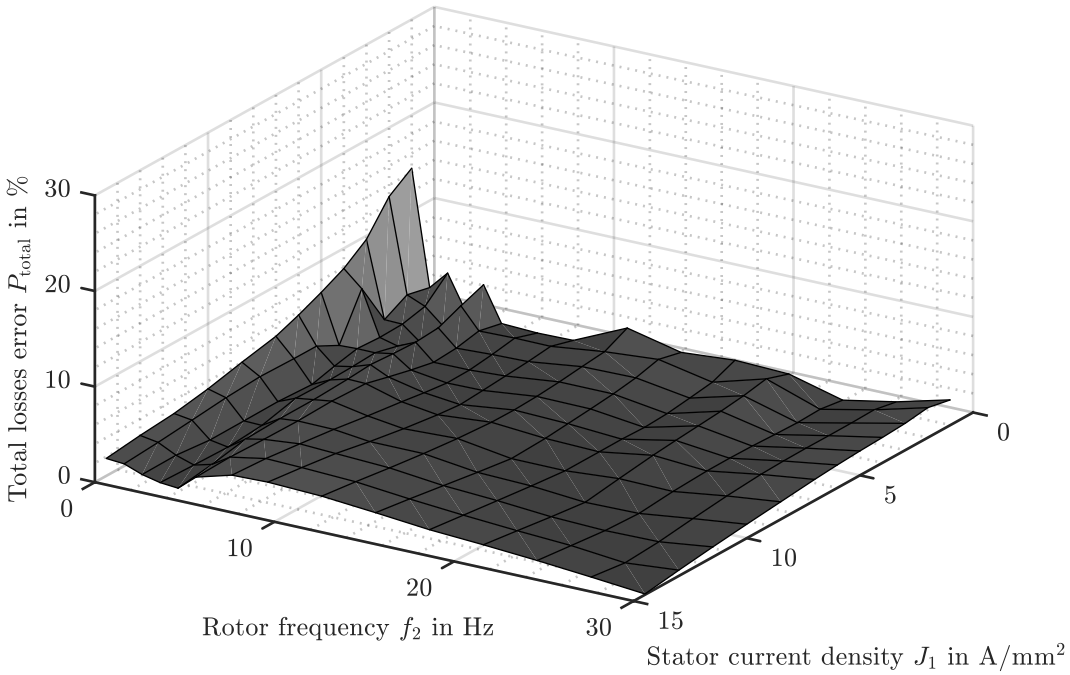

Figure 5.18: Total losses error between the machine with oval bars and the one with Boucherot rods and modified input parameters.

6 Summary and future work

In order to analyze the influence of the skin effect in the scaling procedure when the machine geometry is modified radially or when the design of the rotor bars is changed, a literature review was made to understand the fundamentals of these topics. Based on the information of the FEM, the use of the analytical equations and the theory of the skin effect, a methodology to study the influence of this phenomenon in the scaling process was developed. This procedure established the steps to measure the accuracy of the scaling when the skin effect is taken into account, when the geometry is modified or only the rotor bar design.

To analyze the influence of the rotor bars' skin effect in the geometrical scaling, the parameters that cause this phenomenon were determined based on analytical formulations and results from simulations. This information was used to simulate the machine at conditions were the skin effect is more noticeable. These results were used to calculate the ohmic losses in the rotor bars, accounting for the skin effect in one case and neglecting it in the other. It was concluded that assuming that the current distribution in the rotor is homogeneous, can lead to errors up to 10%. Thus, the skin effect must be considered in the simulations. Furthermore, simulation of different bar topologies was conducted to determine the influence of the shape in the current distribution in the bars.

After characterizing the skin effect, its influence in the accuracy of the scaling procedure was studied. First, a machine model was scaled radially to determine if the skin effect affected the accuracy of the process. It was concluded that when the simulation of the scaled model was carried out with modified input parameters, the errors in the final magnitudes were below 1%. These results ensure that the use of analytical equations to scale the machine is a correct procedure even if the skin effect is present in the rotor bars. A more complex approach is the use of analytical equations to calculate the new machine results when the topology of the rotor bar is changed. As the flux in the reference and the scaled machine need to be similar to use the scaling equations, the changes in the bar shapes must be small. Hence, the first modification is the introduction of a cooling channel in the bar. The results obtained show that the use of analytical equations is possible, yielding errors below 2%. If the modification is more drastic and the entire topology of the bar is changed, the scaling process has errors around 5% in the majority of the points of machine operation.

In order to reduce the errors obtained, there are several improvements to make in future work. One possibility is introducing more scaling factors that account for the variations in the magnetic paths and reduce the differences between the flux of the reference and scaled model. As observed during the scaling, most of flux errors were located in the rotor, since the modifications in the bars affect the magnetic path. Therefore, including a term that accounted for these changes could reduce the errors. Moreover, if not only the rotor bars are modified but also the core, the change of the inductance in the ferromagnetic material induces errors. A scaling factor that considered this variation could increase the accuracy.

Furthermore, when the scaling factor that accounted for the resistance change from one topology to another was calculated, its magnitude was fixed for the entire operating map and was the quotient of the DC resistances of the bars. However, it was shown that the value of the resistance changes for each rotor frequency. Hence, considering this variation and particularize the scaling factor for each point could reduce the losses. Nevertheless, a method to determine this value should be developed as the simulation of the reference machine does not provide enough information.

Finally, the last step would be implementing and testing all this process in a real machine. Although it is costly in terms of time and resources, the results could be the final validation to implement the scaling procedure in the industry.

List of symbols

Latin characters

A	m^2	area
B	T	magnetic flux density
D	$\mathrm{As/m}^2$	electric flux density
E	V/m	electric field strength
F	N	force
H	A/m	magnetic field strength
I	A	current
J	$\mathrm{A/m}^2$	electric current density
J_1	$\mathrm{A/m}^2$	stator current density
J_2	$\mathrm{A/m}^2$	rotor current density
K_R		resistance relation between ac and dc
K_X		reactance relation between ac and dc
L	H	inductance
P_{mech}	W	mechanical power
R_2	Ω	rotor resistance
R_ac	Ω	alternate current resistance
R_dc	Ω	direct current resistance
T	N m	torque
U	V	voltage
V	m^3	volume
X	Ω	reactance
X_ac	Ω	alternate current reactance
X_dc	Ω	direct current reactance
$\mathbb{C}$		set of complex numbers
$\mathbb{N}$		set of natural numbers
$\mathbb{R}$		set of real numbers
a	$\mathrm{m/s}^2$	acceleration
e		Euler's number ($\mathrm{e} = 2{,}718\,281\ldots$)
f	Hz	frequency
f_1	Hz	stator frequency
f_2	Hz	rotor frequency
h	m	height
j		imaginary unit $\left(\sqrt{-1}\right)$

k_a		axial scaling
k_r		radial scaling
k_R		resistance scaling
k_t		time scaling
l	m	length
m	kg	mass
n	1/s	speed
p_{mech}	W/kg	mechanical power density
r	m	radial component in cylindric coordinate system
t	s	time
v	m/s	speed
x	m	x-component in cartesian coordinate system
y	m	y-component in cartesian coordinate system
z	m	z-component in cartesian/cylindric coordinate system

Greek characters

Ψ	Wb	magnetic flux linkage
δ_{ij}		Kronecker-Delta (sometimes also: Kronecker-Symbol)
δ	m	Skin depth of a conductor
ε	As/(Vm)	permitivity (also: dielectric conductivity)
μ	Vs/(Am)	magnetiv permeability (also: magnetic conductivity)
π		Pi ($\pi = 3{,}141\,592\ldots$)
ρ	As/m^3	electric space density
σ	$\Omega^{-1}\,m^{-1}$	electric conductivity
φ	rad	tangential component in cylindric coordinate system
ω	s^{-1}	angular frequency

Subscripts index

0	in void
max	maximum
r	relative
t	tangential
x	in x-Direction
y	in y-Direction
z	in z-Direction
φ	in tangential direction

Nomenclature

$\widehat{x}$	amplitude (also: maximum value)
$\overline{x}$	mean value
$\vec{x}$	vector

Bibliography

[1] *NEMA Standards Publication MG.* Rosslyn, VA, USA : National Electrical Manufacturers Association, 2009

[2] Barta, J. ; Uzhegov, N. ; Losak, P. ; Ondrusek, C. ; Mach, M. ; Pyrhönen, J.: Squirrel-Cage Rotor Design and Manufacturing for High-Speed Applications. In: *IEEE Transactions on Industrial Electronics* 66 (2019), Sep., Nr. 9, S. 6768–6778. http://dx.doi.org/10.1109/TIE.2018.2879285. – DOI 10.1109/TIE.2018.2879285. – ISSN 0278–0046

[3] Boglietti, A. ; Cavagnino, A. ; Lazzari, M.: Computational Algorithms for Induction Motor Equivalent Circuit Parameter Determination—Part II: Skin Effect and Magnetizing Characteristics. In: *IEEE Transactions on Industrial Electronics* 58 (2011), Sep., Nr. 9, S. 3734–3740. http://dx.doi.org/10.1109/TIE.2010.2084975. – DOI 10.1109/TIE.2010.2084975. – ISSN 0278–0046

[4] Boldea, Ion ; Nasar, Syed A.: *The Induction Machine Handbook.* 1st Edition. Boca Raton : CRC Press, 2002. – ISBN 9780429127328

[5] Bone, J. C. H.: Influence of rotor diameter and length on the rating of induction motors. In: *IEE Journal on Electric Power Applications* 1 (1978), February, Nr. 1, S. 2–6. http://dx.doi.org/10.1049/ij-epa.1978.0002. – DOI 10.1049/ij–epa.1978.0002. – ISSN 0140–1327

[6] Chen, J. Q. ; Wang, D. ; Cheng, S. W. ; Yu, Z. J. ; Guo, Y. J. ; Yi, X. Q. ; Yu, Z. S.: 2D FEM transient analysis of permanent magnet motor considering skin effect of stator winding. (2015), Nov, S. 522–523. http://dx.doi.org/10.1109/ASEMD.2015.7453686. – DOI 10.1109/ASEMD.2015.7453686

[7] Cipin, R. ; Patocka, M.: Skin effect in rotor bars of induction motor in form of transfer function. (2013), Nov, S. 3149–3153. http://dx.doi.org/10.1109/IECON.2013.6699631. – DOI 10.1109/IECON.2013.6699631. – ISSN 1553–572X

[8] Deliang Shan ; Xinzhen Wu: Rotor resistance and inductance calculation of single-phase induction motors with skin effect consideration. (2008), Oct, S. 79–82

[9] Fireteanu, V. ; Tudorache, T. ; Turcanu, O. A.: Optimal Design of Rotor Slot Geometry of Squirrel-Cage Type Induction Motors. 1 (2007), May, S. 537–542. http://dx.doi.org/10.1109/IEMDC.2007.382724. – DOI 10.1109/IEMDC.2007.382724

[10] Gerada, D. ; Mebarki, A. ; Brown, N. L. ; Gerada, C. ; Cavagnino, A. ; Boglietti, A.: High-Speed Electrical Machines: Technologies, Trends, and Developments. In: *IEEE Transactions on Industrial Electronics* 61 (2014), June, Nr. 6, S. 2946–2959. http://dx.doi.org/10.1109/TIE.2013.2286777. – DOI 10.1109/TIE.2013.2286777. – ISSN 0278–0046

[11] Gyftakis, K. N. ; Athanasopoulos, D. ; Kappatou, J.: Study of double cage induction motors with different rotor bar materials. (2012), Sep., S. 1450–1456. http://dx.doi.org/10.1109/ICElMach.2012.6350069. – DOI 10.1109/ICElMach.2012.6350069

[12] Hamalainen, H. M. ; Pyrhonen, J. J. ; Puranen, J.: Minimizing skin effect in random wound high speed machine stator. (2009), May, S. 752–757. http://dx.doi.org/10.1109/EURCON.2009.5167718. – DOI 10.1109/EURCON.2009.5167718

[13] Kabbaj, H. ; Roboam, X. ; Lefevre, Y. ; Faucher, J.: Skin effect characterization in a squirrel cage induction machine. 2 (1997), July, S. 532–536 vol.2. http://dx.doi.org/10.1109/ISIE.1997.649011. – DOI 10.1109/ISIE.1997.649011

[14] Kanelis, K. W.: Analytical equations of the induction machine. (2016), Sep., S. 2854–2860. http://dx.doi.org/10.1109/ICELMACH.2016.7732928. – DOI 10.1109/ICELMACH.2016.7732928

[15] L Kirtley, James: Designing Squirrel Cage Rotor Slots with High Conductivity. (2004), 01

[16] Lange, E. ; Henrotte, F. ; Hameyer, K.: An Efficient Field-Circuit Coupling Based on a Temporary Linearization of FE Electrical Machine Models. In: *IEEE Transactions on Magnetics* 45 (2009), March, Nr. 3, S. 1258–1261. http://dx.doi.org/10.1109/TMAG.2009.2012585. – DOI 10.1109/TMAG.2009.2012585. – ISSN 0018–9464

[17] Lee, G. ; Min, S. ; Hong, J.: Optimal Shape Design of Rotor Slot in Squirrel-Cage Induction Motor Considering Torque Characteristics. In: *IEEE Transactions on Magnetics* 49 (2013), May, Nr. 5, S. 2197–2200. http://dx.doi.org/10.1109/TMAG.2013.2239626. – DOI 10.1109/TMAG.2013.2239626. – ISSN 0018–9464

[18] Lin, D. ; Zhou, P.: An improved dynamic model for the simulation of three-phase induction motors with deep rotor bars. (2008), Oct, S. 3810–3814

[19] Maddi, Zakari ; Kadour, Abdoune ; Aouzellag, Djamal: Skin Effect Modelling in Induction Motors Rotor Deep Bars. (2018), 11

[20] Mauffrey, T. ; Pradurat, J. ; Durantay, L. ; Fontini, J.: Comparison of 5 different squirrel cage rotor designs for large high speed induction motors. (2013), May, S. 1–9. – ISSN 2151–7665

[21] McGuiness, D. T. ; Gulbahce, M. O. ; Kocabas, D. A.: A performance comparison of different rotor types for high-speed induction motors. (2015), Nov, S. 584–589. http://dx.doi.org/10.1109/ELECO.2015.7394606. – DOI 10.1109/ELECO.2015.7394606

[22] Nell, M. ; Lenz, J. ; Hameyer, K.: Efficient Numerical Optimization of Induction Machines by Scaled FE Simulations. (2018), Sep., S. 198–204. http://dx.doi.org/10.1109/ICELMACH.2018.8507088. – DOI 10.1109/ICELMACH.2018.8507088. – ISSN 2381–4802

[23] Nell, M. ; von Pfingsten, G. ; Hameyer, K.: Approach for the rapid characterization and control of an induction machine. (2017), Sep., S. 1–2. http://dx.doi.org/10.1109/ISEF.2017.8090672. – DOI 10.1109/ISEF.2017.8090672

[24] Nell, Martin ; Leuning, Nora ; Mönninghoff, Sebastian ; Groschup, Benedikt ; Müller, Fabian ; Karthaus, Jan ; Jaeger, Markus ; Schröder, Michael ; Hameyer, Kay: A Complete and Accurate Modular Numerical Computation Scheme for Multi-Coupled Electric Drive Systems. (2019)

[25] Okoro, Ogbonnaya I.: *Dynamic and thermal modelling of induction machine with non-linear effects*. 2002.

[26] Rahimi, Saeed: *Modeling of Rotor Bars in Induction Motors with Special Focus on Starting Performance*. 2006.

[27] Shamimul, Md ; Choudhury, md ; Uddin, Muhammad ; Hasan, Md. N. ; Alam, Shafiul ; Farhan, Meer ; Bashar, Ibn: Impact of skin effect for the design of a squirrel cage induction motor on its starting performances. In: *International Journal of Engineering Science and Technology* 4 (2012), 01

[28] Silvas, E. ; Hofman, T. ; Murgovski, N. ; Etman, L. F. P. ; Steinbuch, M.: Review of Optimization Strategies for System-Level Design in Hybrid Electric Vehicles. In: *IEEE Transactions on Vehicular Technology* 66 (2017), Jan, Nr. 1, S. 57–70. http://dx.doi.org/10.1109/TVT.2016.2547897. – DOI 10.1109/TVT.2016.2547897. – ISSN 0018–9545

[29] Stipetic, S. ; Zarko, D. ; Popescu, M.: Scaling laws for synchronous permanent magnet machines. In: *2015 Tenth International Conference on Ecological*

Vehicles and Renewable Energies (EVER) (2015), March, S. 1–7. http://dx.doi.org/10.1109/EVER.2015.7113006. – DOI 10.1109/EVER.2015.7113006

[30] Turcanu, O. A. ; Tudorache, T. ; Fireteanu, V.: Influence of squirrel-cage bar cross-section geometry on induction motor performances. (2006), May, S. 1438–1443. http://dx.doi.org/10.1109/SPEEDAM.2006.1649994. – DOI 10.1109/SPEEDAM.2006.1649994

[31] van der Giet, M. ; Schlensok, C. ; Schmulling, B. ; Hameyer, K.: Comparison of 2-D and 3-D Coupled Electromagnetic and Structure-Dynamic Simulation of Electrical Machines. In: *IEEE Transactions on Magnetics* 44 (2008), June, Nr. 6, S. 1594–1597. http://dx.doi.org/10.1109/TMAG.2007.916121. – DOI 10.1109/TMAG.2007.916121. – ISSN 0018–9464

[32] Vande Sande, Hans: *Modelling and Finite Element Simulation of Non-Linear and Anisotropic Quasi-Static Electromagnetic Systems*. 1st Edition. Leuven : Katholieke Universiteit Leuven, 2003. – ISBN 90–5682–426–0

[33] von Pfingsten, G. ; Hameyer, K.: Highly efficient approach to the simulation of variable-speed induction motor drives. In: *IET Science, Measurement Technology* 11 (2017), Nr. 6, S. 793–801. http://dx.doi.org/10.1049/iet-smt.2017.0152. – DOI 10.1049/iet–smt.2017.0152. – ISSN 1751–8822

[34] von Pfingsten, G. ; Nell, M. ; Hameyer, K.: Hybrid simulation methods for induction machine calculation reduction of simulation effort by coupling static FEA with transient FEA and analytic formulations. (2017), Sep., S. 1–2. http://dx.doi.org/10.1109/ISEF.2017.8090681. – DOI 10.1109/ISEF.2017.8090681

[35] von Pfingsten, G. ; Steentjes, S. ; Hameyer, K.: Transient approach to model operating point dependent losses in saturated induction machines. (2016), Sep., S. 626–632. http://dx.doi.org/10.1109/ICELMACH.2016.7732591. – DOI 10.1109/ICELMACH.2016.7732591

[36] Von Pfingsten, G. ; Steentjes, S. ; Hameyer, K.: Operating Point Resolved Loss Calculation Approach in Saturated Induction Machines. In: *IEEE Transactions on Industrial Electronics* 64 (2017), March, Nr. 3, S. 2538–2546. http://dx.doi.org/10.1109/TIE.2016.2597761. – DOI 10.1109/TIE.2016.2597761. – ISSN 0278–0046

[37] Williamson, S. ; McClay, C. I.: Optimization of the geometry of closed rotor slots for cage induction motors. In: *IEEE Transactions on Industry Applications* 32 (1996), May, Nr. 3, S. 560–568. http://dx.doi.org/10.1109/28.502167. – DOI 10.1109/28.502167. – ISSN 0093–9994

Sperrvermerk und Selbstständigkeitserklärung

Diese Master Thesis ist geschütztes Eigentum des betreuenden Institutes dem Institut für Elektrische Maschinen (IEM) der Rheinisch-Westfälischen Technischen Hochschule (RWTH) in Aachen.

Die Weitergabe von Ergebnissen, von Soft- und Hardware und von Unterlagen der Master Thesis an Dritte ist untersagt. Eine Ausnahmeregelung ist nur mit der schriftlichen Genehmigung des Institutsleiters Univ.-Prof. Dr.-Ing. habil. Dr. h. c. Kay Hameyer möglich.

Ich bin auf die möglichen rechtlichen Folgen bei Zuwiderhandlung hingewiesen worden und ich versichere, dass ich die Arbeit selbständig und ohne Zuhilfenahme unzulässiger Mittel erstellt habe.

Aachen, im September 2019

David Maldonado Lopez